NOTICE

The quality of this microform is heavily dependent upon the quality of the original thesis submitted for microfilming. Every effort has been made to ensure the highest quality of reproduction possible.

If pages are missing, contact the university which granted the degree.

Some pages may have indistinct print especially if the original pages were typed with a poor typewriter ribbon or if the university sent us an inferior photocopy.

Reproduction in full or in part of this microform is governed by the Canadian Copyright Act, R.S.C. 1970, c. C-30, and subsequent amendments.

AVIS

La qualité de cette microforme dépend grandement de la qualité de la thèse soumise au microfilmage. Nous avons tout fait pour assurer une qualité supérieure de reproduction.

S'il manque des pages, veuillez communiquer avec l'université qui a conféré le grade.

La qualité d'impression de certaines pages peut laisser à désirer, surtout si les pages originales ont été dactylographiées à l'aide d'un ruban usé ou si l'université nous a fait parvenir une photocopie de qualité inférieure.

La reproduction, même partielle, de cette microforme est soumise à la Loi canadienne sur le droit d'auteur, SRC 1970, c. C-30, et ses amendements subséquents.

THE UNIVERSITY OF ALBERTA

QUANTIFICATION OF CALCIUM IN SOLITARY PULMONARY NODULES: A COMPARISON OF THREE MODALITIES

BY

WARREN G. ANDERSON

A THESIS

SUBMITTED TO THE FACULTY OF GRADUATE STUDIES AND RESEARCH IN PARTIAL FULFILMENT OF THE REQUIREMENTS FOR THE DEGREE OF MASTER OF SCIENCE

IN

RADIOLOGICAL PHYSICS

DEPARTMENT OF RADIOLOGY AND DIAGNOSTIC IMAGING

EDMONTON, ALBERTA

SPRING 1989

ISBN 0-315-52997-0

THE UNIVERSITY OF ALBERTA

RELEASE FORM

NAME OF AUTHOR : Warren G. Anderson

TITLE OF THESIS : Quantification of Calcium in Solitary Pulmonary Nodules: A Comparison of Three Modalities

DEGREE : Master of Science

YEAR THIS DEGREE GRANTED : 1989

#4 10731 85 Ave,

Edmonton Alberta,

T6E-2K9

Date: April 18, 1989

Measured objectively, what a man can wrest from Truth by passionate striving is utterly infinitesimal. But the striving frees us from the bonds of the self and makes us comrades of those who are the best and the greatest.

- Albert Einstein -

THE UNIVERSITY OF ALBERTA

FACULTY OF GRADUATE STUDIES AND RESEARCH

The undersigned certify that they have read, and recommend to the Faculty of Graduate Studies and Research for acceptance, a thesis entitled Quantification of Calcium in Solitary Pulmonary Nodules: A Comparison of Three Modalities submitted by Warren G. Anderson in partial fulfilment of the requirements for the degree of Master of Science in Radiological Physics.

.....
Supervisor

.....

.....

.....

.....

Date: April 18, 1989

To my Mom, Angele, Nicole, and Renee, for the unique outlook on life they shared with me, and to LJF, for being my mentor and my friend.

Abstract

Solitary pulmonary nodules are often found in chest radiographs of otherwise asymptomatic patients. In the past, distinguishing benign nodules has required invasive procedures. Over the last decade, investigation into using radiological imaging methods to identify calcium in benign nodules has increased rapidly. Computed tomography, analog radiography, and digital radiography have been used to quantify calcium in SPNs. Computed tomography has become commonly used. CT research suggests 40 mg/ml is a minimum level of calcification for which a nodule can be considered benign. This thesis will attempt to compare the quantitative capabilities of these three imaging modalities to one another and to the 40 mg/ml threshold. As a result of this comparison, the suitability of each modality for routine screening will be discussed.

Acknowledgements

I'd like to thank all the people who helped me in various ways with my thesis:

my family for their faith.

the people in CT at both the U of A and the Grey Nuns for their expertise and patience, especially Wendy Olsen and Doug Bridgeman who always made time for me.

the secretaries of the department of radiology for their inumerable services, especially Janet.

Dr. Russell for his support, both financial and moral, and his belief in the importance of medical physics.

my committee for their guidance and instruction.

Larry Filipow, D.Phil., for his help in every aspect of my thesis and my life.

Jim, Mark, and Suzanne for their companionship and interest.

Wally, Sanjay, Chuck, Jack, Andrew and sometimes Gene, for their comradery and insights, and the great lunchtime discussions we had.

Brenda, for being there for me through most of it.

TABLE OF CONTENTS

TABLE OF CONTENTS (cont.)

TABLE OF CONTENTS (cont.)

LIST OF TABLES

List of Figures

List of Figures (cont.)

List of Figures (cont.)

List of Figures (cont.)

List of Figures (cont.)

Chapter 1 : Introduction

1.1 Rationale

Solitary pulmonary nodules (SPNs) are occasionally identified on chest radiographs of otherwise asymptomatic individuals. These nodules might be either benign or malignant. It is important to identify malignant lesions so that they might be resected. At the same time, for benign nodules, unnecessary surgery should always be avoided if possible, and thoracotamy may lead to complications.

This is the dilemma faced by a physician upon the detection of a pulmonary nodule on a patient's radiograph. There are two current reliable radiological indicators of benignancy in SPNs[1]. The first is a lack of detectable growth over a two year observation period. The second is the presence of a 'sufficient' level of calcification.

When these conditions are not clearly satisfied, a biopsy is usually necessary to determine if the lesion is malignant. This bears its own risks, not the least of which is the possibility of metastases. Non-invasive methods are clearly preferable. Of the two radiological methods, if no prior chest radiographs are available, then only the detection of calcification can be used to determine benignancy.

Nodules which are highly calcified, or those with local pockets of calcification, are readily identified by qualitative observation of a radiograph. However, a sufficient level of diffuse calcification often exists to ensure that the nodule is benign. Diffuse calcification is much more difficult to detect, especially when the

concentrations are low. It is of value, then, to develop a non-invasive method to detect low concentrations of diffuse calcification in SPNs.

The most likely methodology for doing this would involve a diagnostic imaging procedure. Attempts have already been made with at least three modalities[1,2,3]. These attempts have met with varying degrees of success. They will be discussed in more detail below. There have also been some attempts to cross compare the three methodologies[2,3,4], but they have been limited, and there has been disagreement between them.

It is the intention of this work to compare, from a physical science perspective, the performances of these three modalities and to try to develop simpler, quicker, more accurate, and less expensive methods of quantifying calcium (Ca) in SPNs using projective radiological procedures.

1.2 Basic Theoretical Background

The three radiological modalities used to quantify calcium in SPNs have been analog radiography, CT, and digital radiography. These are all projective radiological procedures, ie, those that require projection of x-rays through the imaged object (patient). Such procedures are the most widely used in diagnostic imaging and provide the best prospective for low level Ca quantification.

It is easy to understand the physical basis upon which the detection of calcification is based. To demonstrate: an x-ray of energy E passes through an object composed of n different types of material

(see Fig 1). The path length of the x-ray through each material (i) is l_i. For this x-ray of energy E, the linear attenuation coefficient for each material is $\mu_i(E)$. The probability of the x-ray traversing the object without being interacting is:

$$(1.2.1) \qquad P(\text{no atten}) = \exp \sum_{i=1}^{n} -(\mu_i[E] \cdot l_i)$$

Thus, for a polychromatic spectrum of photons $N_0(E)$, the number of photons that traverse the object without interacting is:

$$(1.2.2) \qquad N_t = \int_0^{Emax} dE\ N_0[E] \cdot \exp \sum_{i=1}^{n} -(\mu_i[E] \cdot l_i)$$

It is a valid approximation to suppose that the polychromatic spectrum acts like a monochromatic beam with effective energy E_{eff}. Eq (1.2.2) then becomes:

$$(1.2.3) \qquad N_t = N_0 \cdot \exp \sum_{i=1}^{n} -(\mu_i[E_{eff}] \cdot l_i)$$

By measuring N_t for an object, we have in essence measured the sum of $\mu_i l_i$ for the object. Measuring N_t for n different effective energies will provide n equations, and thus a unique solution, for the n quantities $\mu_i l_i$.This is the basis of multi-energy subtraction.

Alternately, the object may be considered to be composed of a large number of individual volumes, each of small but finite extent. Each volume will have an average attenuation coefficient μ_j. By obtaining transmission values along a large but finite number of rays through each volume, one may calculate these coefficients. This is the principle used in computed tomography (CT).

X-RAY ATTENUATION

$$N = N_0 \sum_{i=1}^{3} -\mu_i(E) l_i$$

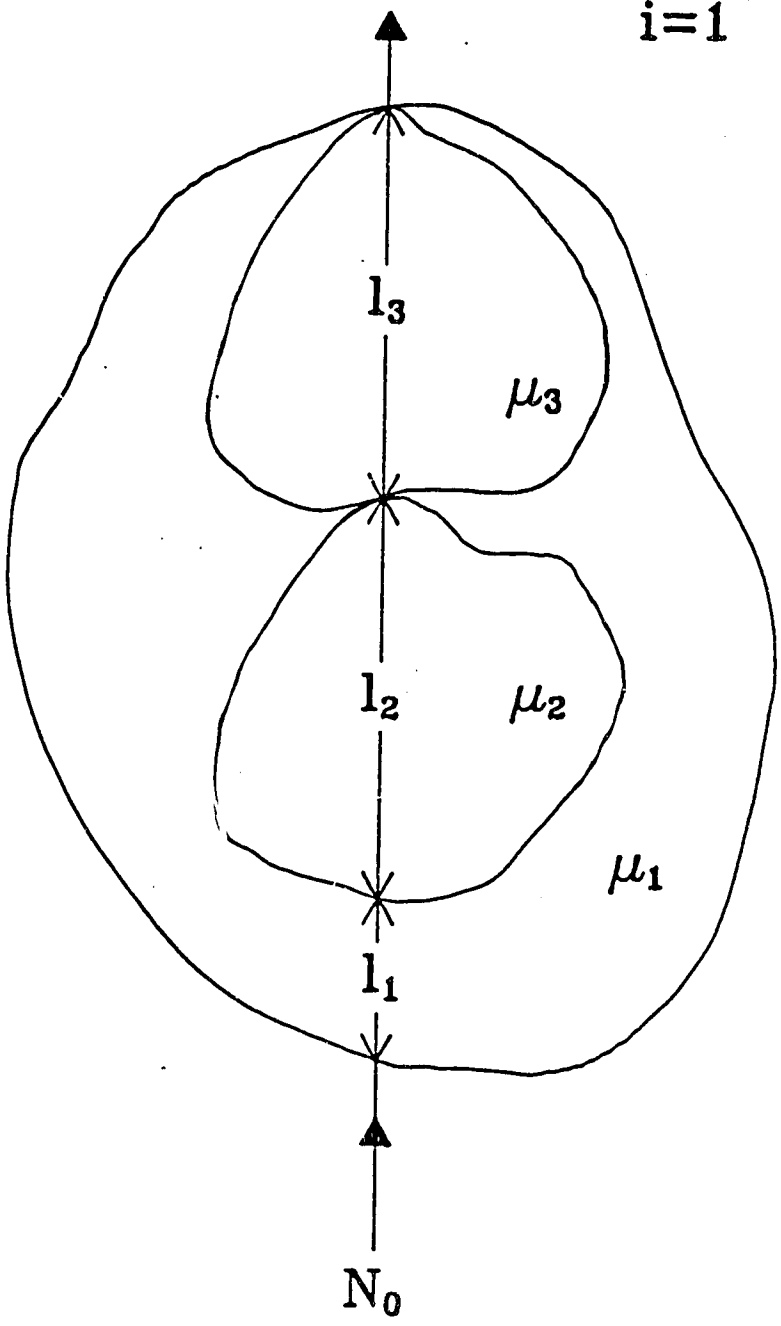

Fig. 1 Attenuation of monoenergetic x-ray photons.

In either case, a large number of x-rays are required. X-rays used in diagnostic imaging are produced by a process known as bremsstrahlung: energetic charged particles, when decelerated, will lose a portion of their kinetic energy by creating x-rays. Bremsstrahlung is accomplished most efficiently by shooting light charged particles at atoms with heavy, highly charged nuclei.

In an x-ray tube, high energy electrons are shot at a target made of tungsten (Z=74). The charges on the nuclei in the tungsten atoms will violently accelerate each electron as it passes near the nucleus, causing it to produce x-rays.

Because of the statistical nature of the bremsstrahlung interaction, the radiation is produced with a spectrum of energies, ranging from the kinetic energy of the incoming particle to essentially 0. A typical, filtered, bremsstrahlung spectrum is shown in Fig 2. The number of photons emitted is almost linear with the inverse of the energy, but those with low energies are typically attenuated within the x-ray tube before they can be seen or measured.

After passing through the patient, the unattenuated portion of the beam is transmitted to the detector. For analog radiography, the detector is a film screen combination. For CT, the detectors are electronic radiation detectors, such as ionization chambers or scintillation crystals. For digital radiography the detectors are either image intensifiers (II's) or electronic detectors much like those for CT.

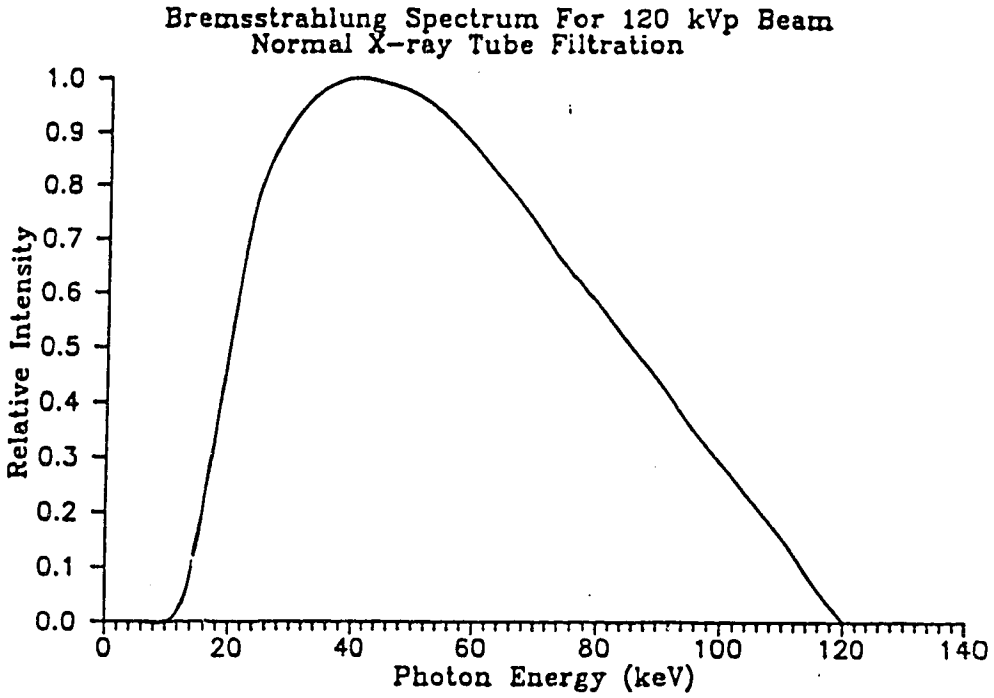

Fig. 2 A typical energy spectrum for x-rays from an xray tube.

In diagnostic imaging, only those x-rays that are transmitted through the object are measured. The rest are attenuated; absorbed or scattered in the object. When an x-ray is attenuated it deposits its energy into the object. The energy from attenuated x-rays may damage the living body tissues. The degree of tissue damage is proportional to the energy deposited per unit mass of attenuator. This quantity is called the absorbed dose and is measured in Grays or joules per kilogram.

Thus, although transmissive radiology is a useful tool, it is not without isk. The risks of not having a diagnosis, however, or of obtaining it by invasive techniques are considered much higher than those from radiation. Clearly, though, radiological procedures should be used prudently.

Electronic detectors use various means to convert radiation to electrical energy. The electrical impulses are measured and converted into numeric values which are stored in a computer system. CT scanners convert the electrical impulses into CT numbers (CT#) or Hounsfield Units (HU). These units compare the attenuation of a volume of the imaged object to that of water. The formula for a CT# is:

(1.2.4) $CT\# = k \times (\mu - \mu_W)/\mu_W$

where : k is an arbitrary constant (usually 1000).

μ is the attenuation coefficient of the object volume.

μ_W is the attenuation coefficient of water.

When k is 1000 a CT# is in units of HU.

1.3 Experimental Background

1.3.1 Analog Radiography

Film-screen combinations are the most common x-ray detectors used. Although x-rays will expose a film directly, in modern radiography screens are used. These are usually sheets of plastic containing crystals of rare earth compounds. These crystals fluoresce when exposed to x-rays, providing a source of visible photons, which expose the film much more efficiently than x-ray photons.

When the film is developed, it will be dark where there has been greater exposure, light where there has been less exposure. A quantitative measure of film darkness is the optical density (OD). The manner in which the optical density varies with the logarithm of the x-

ray exposure is called the characteristic curve. A typical characteristic curve is shown in Fig 3.

The characteristic curve for a film-screen combination is linear over some range of exposures, and this is what should produce the image. This range is related to the gamma of the characteristic curve. The gamma is the maximum slope of the characteristic curve. High contrast comes from film screen combinations with high gammas, while a greater latitude (useful exposure range) is provided by lower gamma systems.

Since the mid 1950's, analog radiography had not been considered a likely candidate for Ca quantification in SPNs. The reason was that although radiographs provide excellent resolution, they were considered to lack contrast sensitivity. In 1980 Kruger et al. from the University of Utah investigated the use of dual energy film subtraction for Ca quantification[3].

They showed theoretically, and to some extent experimentally, that subtracting films taken at different energies can remove tissue contributions. However, imperfect matching of the tissue optical densities between films left some residual tissue contributions. These unwanted contributions corresponded to Ca levels of up to 100 mg/cm^2. 125 mg/ml in a 1 cm diameter lesion was therefore determined as the minimum Ca detectable.

These results were obtained with idealized phantoms and not expected to improve in clinical use. It was also not made clear how this method was to be implemented in a clinical environment. Presumably, measured optical densities would be compared to a calibration curve obtained through experiment or theoretical

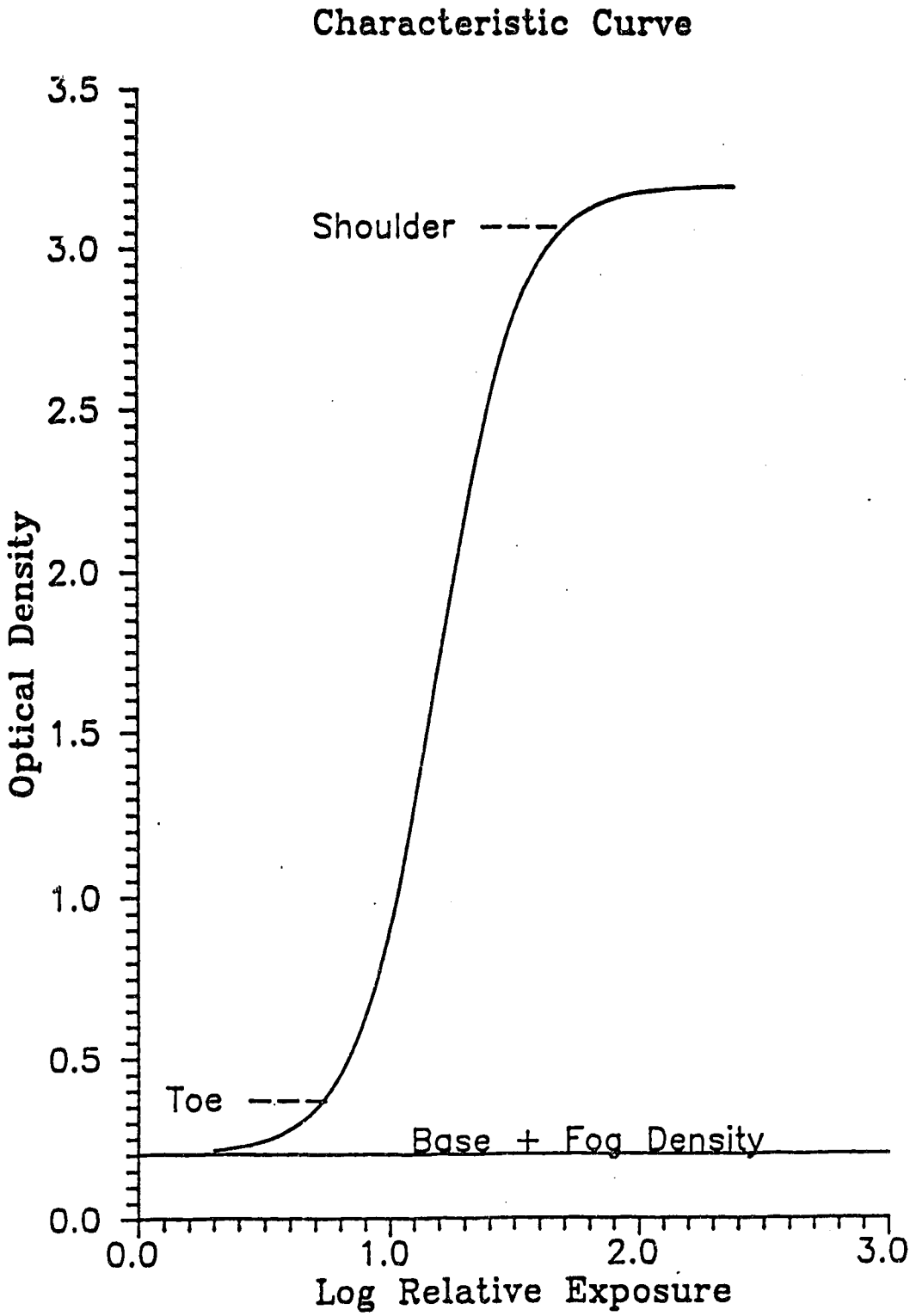

Fig. 3 A typical film-screen characteristic curve.

considerations. This, however, would lead to further error, since the variability in exposures between calibration and measurement could be considerable.

One method of minimizing error would be to simultaneously image a phantom with the patient. This would provide a calibration curve from data with identical image characteristics to the SPN. If further reduction in the dual energy subtraction error could be obtained, this might provide a moderately successful method of quantitation. Furthermore, this method would be less costly, less time consuming, and less complicated. Patient exposure would be much less than for CT, and the only equipment required would be a common radiographic procedure room.

1.3.2 Digital Radiography

Barring significant improvements in analog radiography, another alternative is digital radiography. Work has been done on quantification of SPNs using digital radiography by Barnes et al. from the University of Alabama in Birmingham[2]. This group had at their disposal a prototype dual energy digital scanning slit chest unit[8,9,10] provided by the Advanced Development Group of Picker International.

The Birmingham group did work on both detection[11,12] and quantification[2] of Ca in SPNs. During these experiments, dual energy radiographs were obtained. These were subtracted to show either only calcium (bone) or only tissue contributions.

On the digital bone images, a parallelogram region of interest was defined over a nodule. The parallelogram edges were chosen by the

operator to be parallel to the edges of the ribs, so as to provide a uniform background behind the nodule (ie, no rib, single rib or double rib background). A frequency distribution of pixel values was obtained showing the background as a base level density with the nodule density 'sitting' on top of this base. The base level was subtracted leaving only the nodule pixel values. The average pixel value was calculated and compared to a calibration curve to obtain an estimate of the Ca concentration. Standard deviations were also determined.

Measurements of simulated nodules whose Ca level were determined by this technique and plotted against the actual values showed that the system could detect no less than 35 mg/cm^2 accurately. A Ca sensitivity of only 35 mg/cm^2 is poorer than expected for this technique. However, no provisions were made for the fact that the projection of the spherical nodule onto a two dimensional radiograph will lead to a nonuniform distribution of Ca.

Also, the possible effects of system variation between calibration and measurement had again not been dealt with. Use of an in-scan calibration phantom might have allowed more accurate quantification. Nor has a discussion of system parameter optimization been given.

Nonetheless, digital radiography seems to hold substantial promise for Ca quantification. While detectability may not be as good as for CT, it may be more than adequate. The major obstacle to the use of digital radiography is currently a lack of equipment availability, with only a few large hospitals having digital angiographic equipment, and virtually no scanning projection chest units available. This, however, is expected to change significantly in the near future, which

would mean that digital radiography might provide a viable alternative to CT for Ca quantitation.

1.3.3 CT

Of the three types of transmissive radiological methods used in attempting to quantify calcium in SPNs, only CT appears to be gaining significant clinical use. Commercially available phantoms designed for use in SPN calcium quantitation are currently available.

Siegalman and Zerhouni and their group at Johns Hopkins were amongst the first to carefully study the use of CT in this application[1]. They used a Pfizer/A.S.&E. scanner to study 88 patients with 91 nodules. Of these, 58 nodules were malignant and 33 benign. The average size of malignant lesions was 2.4 cm; benign, 1.3 cm.

The mean C.T. number (CT#) for each nodule was calculated by averaging over the CT#s for the highest 32 contiguous voxels within the nodule. The 45 primary malignancies had a mean CT# of 92 and a standard deviation of 18. It was decided that the mean plus 4 standard deviations would provide an adequate degree of certainty for calcification, and therefore 164 was suggested as the threshold CT# for benignancy.

Obvious calcification was detected at the 600-800 CT# range. Thus, this quantitative evaluation provided information that qualitative observation had not. The 146 to 164 CT# region was considered borderline. Below 146, lesions were classified as malignant, even though 8 were in fact benign. This is acceptable; one would expect

a high rate of false positives since there must be a high confidence that there will be no false negatives.

Subsequent work, however, led to some doubt about these results. A Duke University group found that CT was only a slightly more reliable indicator of benignancy than analog radiography[5]. Others found CT#s to be unreliable as quantitative values[6].

In response the Johns Hopkins group showed that CT#s are machine and parameter dependent for a given scanner[4]. 164 Hounsfield units (HU) for their machine with the parameters used previously was shown to correspond to 40 mg/ml of calcium. A calibration phantom with a tissue-like thoracic wall and interchangeable SPN phantoms of various sizes which could be positioned anywhere within the lung was designed for scanning immediately after the patient in order to allow a machine and attenuation independent method of quantitation[7]. This was the basis for the design of subsequent commercial packages for quantification of Ca in SPNs.

1.4 Proposed Research

Analog radiology may provide a viable alternative to CT for calcium quantification. Although early investigations proved discouraging[3], expectations may have been too exacting. For instance, plexiglass subtraction for thicknesses between 7 and 18.6 cm yielded errors equivalent to 125 mg/cm^2 of Ca. However, this represents a range of tissue depths that is greater than would likely be seen over the regions of interest in a chest radiograph.

Also, use of analog radiology for Ca quantitation requires investigation beyond that provided by Kruger. After his dual energy subtraction is used, reference to a calibration curve is still necessary. This may be accomplished in many ways, but the least error might be provided by scanning a calibration phantom simultaneously with the patient.

Also, a different method of performing dual energy scans may be necessary. Kruger used two different exposures with different kVps and filtration. In a clinical setting, this may lead to significant error from motion artifacts. A dual energy cassette system, exposing two films at once, may be more accurate in this regard[13].

Issues to be addressed for analog radiographic Ca quantification will therefore be:

1) Design and construction of a Ca calibration phantom suitable for use with the patient.

2) Investigation of system parameters and their effects on quantitation errors.

If these investigations yield promising results, two more issues will be addressed:

3) Design of a dual-energy cassette tissue subtraction method.

4) Determination of the effect of residual tissue contributions on calcium quantification.

Digital radiography has already shown promise for calcium quantification[2]. The drawback here is that there is an overwhelming lack of systems like that used for these experiments. Two solutions seem viable.

Although digital radiographs acquired through image intensifier (II) systems are produced in a fundamentally different manner than those acquired by scan projected digital radiography (as were those by the Birmingham group), they are more common because they are currently used for digital angiography. Work has already been done on errors in dual energy II systems from a theoretical standpoint[14]. Recently, Kruger looked at a hybrid of the two types of systems as a means of bone mineral quantification[15].

Scan projected digital radiography (SPDR) is already used in clinical radiography. Such radiographs are produced on CT units in order to provide anatomical reference for slice selection. Although not presently used diagnostically, a 1979 study of these radiographs showed them to have good low contrast sensitivity and to provide lower doses than analog radiography[16]. Scanner design has improved since 1979 so results may meet or exceed the high expectations that are encouraged by that work.

As regards the use of digital radiography for calcium quantification in SPNs, examination of the following will be conducted:

1) Determination of the suitability of an II based digital subtraction angiography (DSA) unit using methods similar to those proposed for analog radiography.
2) Determination of the minimum error that can be achieved.
3) Determination of the suitability of CT scanners as SPDR devices for Ca quantification.
4) Examination of the effects of system parameters on contrast sensitivity and determination of the minimum quantification error.

5) Development of a clinically useful quantification method.

At present, CT provides the best alternative for quantification of calcium in solitary pulmonary nodules using transmissive radiological methods. Unfortunately, although the quantitative abilities of CT scanners seem to be adequate, the method employed is lengthy, costly, and complicated. It is moderately available. Although some system parameters have been shown to affect quantification[4], optimization of these parameters has not been discussed. Also, little work has been done to investigate quantification errors in detail.

In regard to the use of CT then, the following issues will be addressed in this thesis:

1) Determination of the sources and magnitudes of error in quantification.
2) Determination of the optimal system parameters for quantification, ie, those that give the minimal error. Since these may be system dependent, three systems will be studied.
3) Determination of possible simplifications to the present method.

Through a comparison of these different modalities, it is hoped that an optimal method of Ca quantification in SPNs may by found.

As a by-product of the phantom design that will be necessary, it is also believed that some insight into optimal phantom design will be achieved. In the papers cited above, no fewer than 4 calcium or potassium salts, suspended in three different media, were used as phantoms. None of the salts used was hydroxyapatite ($Ca_3(PO_4)\cdot Ca(OH)_2$), the primary constituent of bone and most likely candidate for calcification.

Chapter 2: Analog Radiography

2.1 Materials

A Philips fluoroscopy unit used for these experiments (model numbers - tube: SRO 33 100 HEW, housing: RTO 350, generator: MCM-100). This system has a maximum rated peak tube voltage of 150 kV. It has stated nominal focal spot sizes of 0.6 mm (small focal spot) and 1.2 mm (large focal spot). The anode has a rhenium alloyed tungsten-molybdenum compound construction. It is angled at 13°. The high voltage generator is a three-phase rectified twelve pulse generator with falling load capability.

Various phantoms were used during these experiments. Two 30 cm x 30 cm x 6 cm water filled blocks with 0.5 cm plexiglass walls were used as a scattering medium to simulate the patient's thorax. To measure the source to image distance of the fluoroscopy (fluoro) unit an alignment phantom was used (see Fig 4). This phantom consists of a plexiglass cylinder closed at both ends. Radio-opaque objects are imbedded in each end. This allows the relative magnifications of these objects to be measured on a radiograph of the phantom, and simple triangulation is used to determine the source to image distance.

Two aluminum step wedges were also used. A step wedge is simply a block of aluminum which has 'steps' cut into it in one dimension. This provides attenuation of the x-ray beam by various thicknesses of aluminum in a single exposure. One step wedge consisted of eleven 3 mm

GEOMETRY PHANTOM

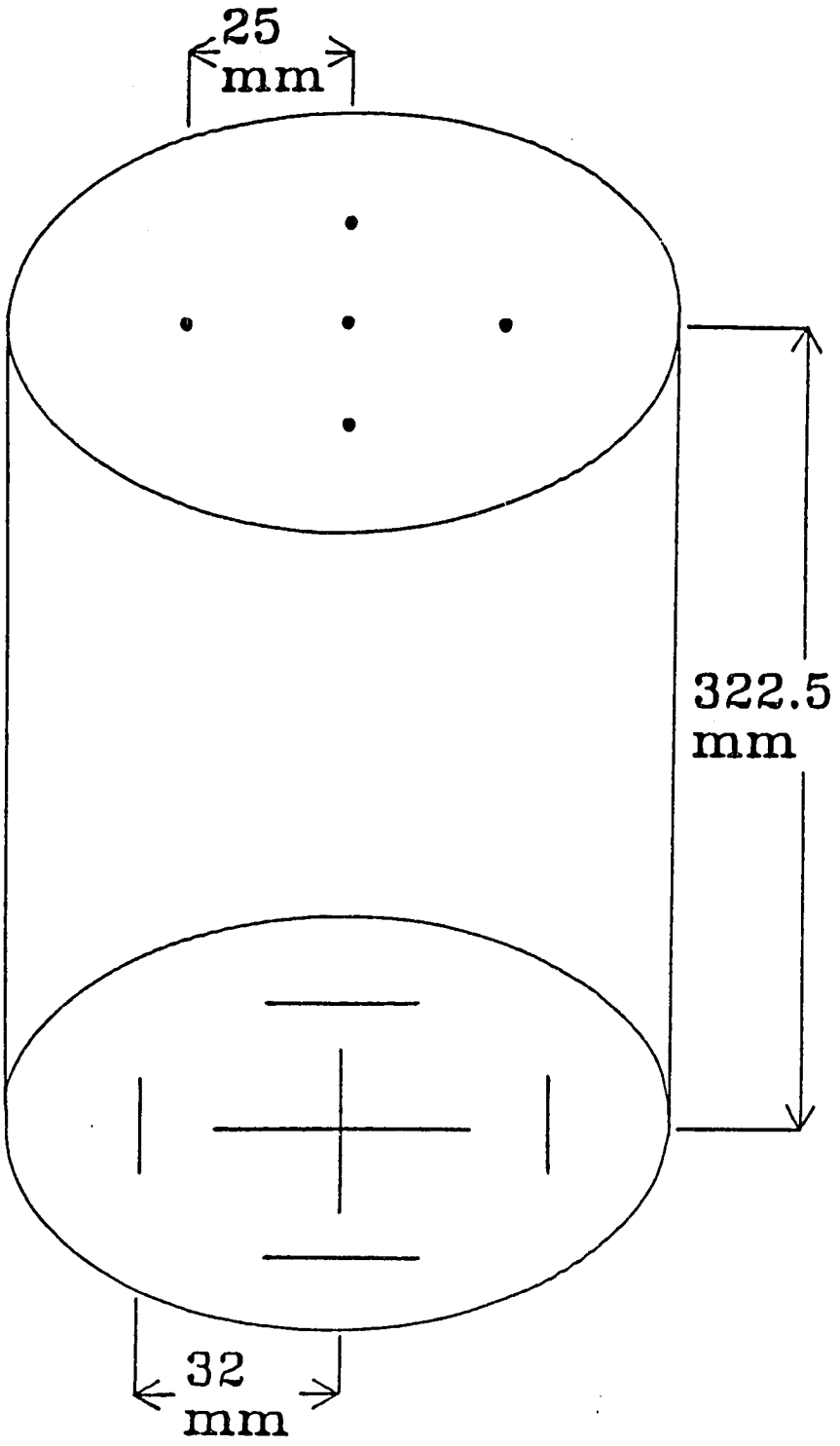

Fig. 4 The alignment or geometry phantom.

thick steps from 5 mm to 35 mm. The other had five steps of 0.5, 1, 2, 3, 4 and 5 mm thicknesses.

To simulate SPNs five pill bottles of 21.5 mm (± 0.5mm) inside diameter were used. They contained the calcium salt Tri-basic Calcium Phosphate $Ca_3(PO_4)_2$ in concentrations as specified in Table 1. $Ca_3(PO_4)_2$ was used primarily because of its availability and similarity in composition to hydroxyapatite. Its theoretically calculated attenuation cross section is compared with that of other calcium salts in Fig 5.

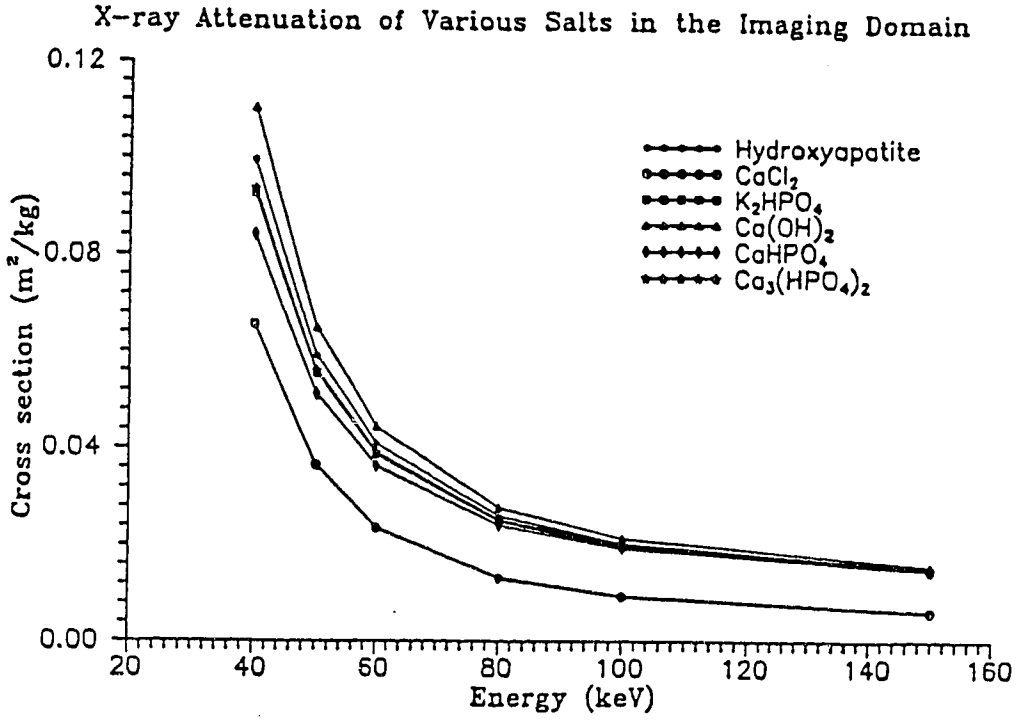

Fig. 5 Crossections of various salts, theoretically calculated using data from Hubbel (see bibliography).

Table 1 Calcium Salt Concentrations in Pill bottle Phantom

Bottle #	$Ca_3(PO_4)_2$ mass (± .05 grams)	$Ca_3(PO_4)_2$ conc (mg/cm^2)
0	0.0	0+-0
1	0.20	54+-16
2	0.35	96+-18
3	0.72	198+-23
4	1.45	399+-32

To each pill bottle 11 grams of water was added to ensure that the salt maintained a constant depth over the entire cross sectional area of the phantom.

A phantom designed specifically for calcium quantitation for plain films was also used. The schematics for this phantom are shown in Fig 6. It consisted of 7 concentric circular compartments. The compartments were circles 4 mm wide and 2 cm deep carved into a piece of lucite. Each compartment contained a different calcium concentration. The calcium concentrations consisted of $Ca_3(PO_4)_2$ suspended in petroleum jelly. Initial concentrations were 25, 50, 100, 150, 200, 300, and 400 mg/cm^2 of calcium salt. Petroleum jelly was used because it has a roughly tissue-like (soft tissue and water can be considered to have the same attenuation properties for most cases) attenuation cross section (see Fig 7) and because of its viscosity which readily suspended the calcium salt.

The above concentrations were selected because they provided a wide range of attenuations with which to determine the sensitivity of spot-filming. The circular geometry was chosen so that, in clinical use, at least one portion of each compartment might appear on the film without being obstructed by bone. It is worth noting at this point that

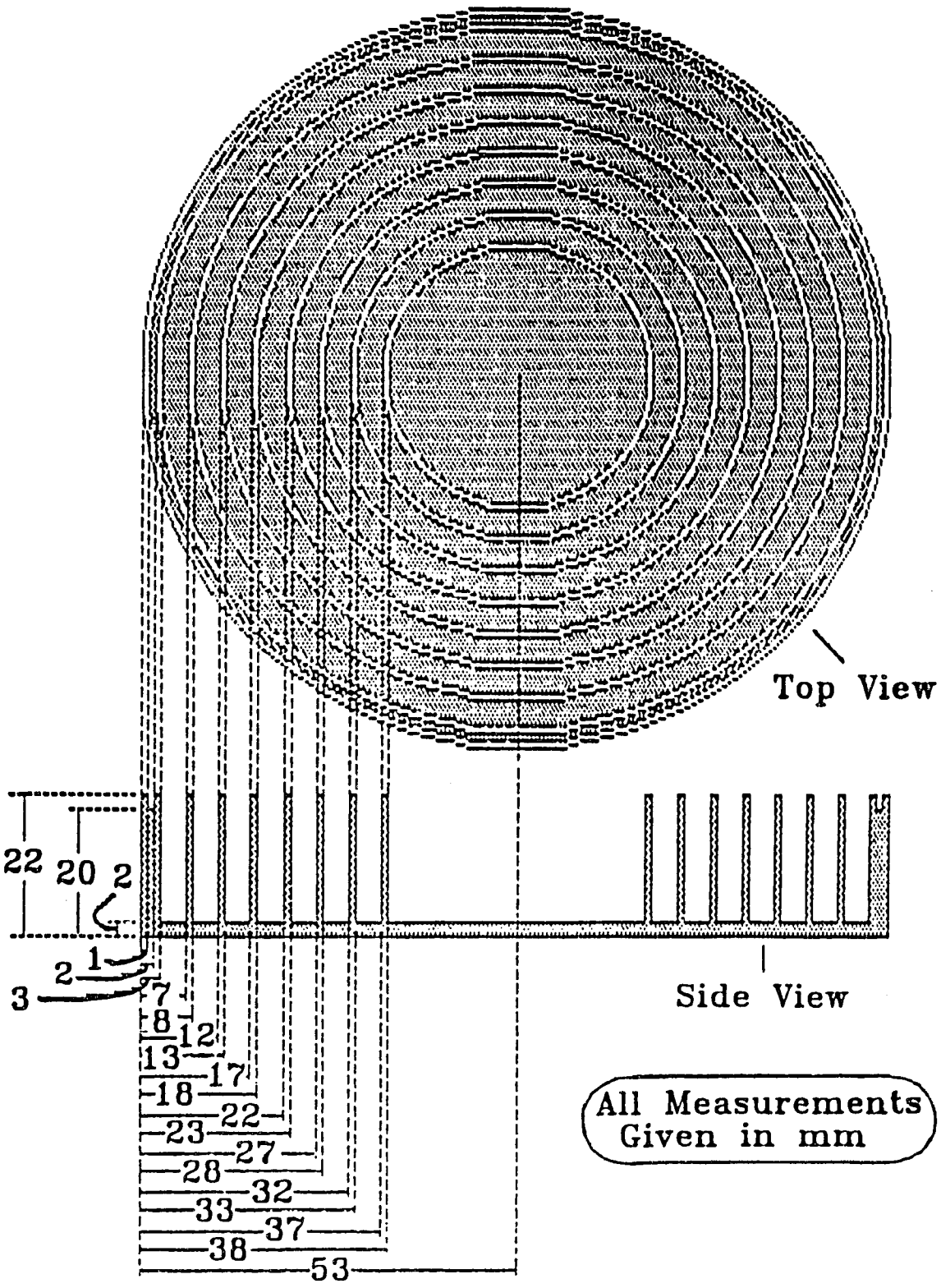

Fig. 6 The ring phantom designed for radiographic quantification.

the phantom proved extremely difficult to assemble because air pockets were created in the compartments during filling, thus leading to inhomogeneities in the phantom. There were, however, usable portions of each compartment of the phantom.

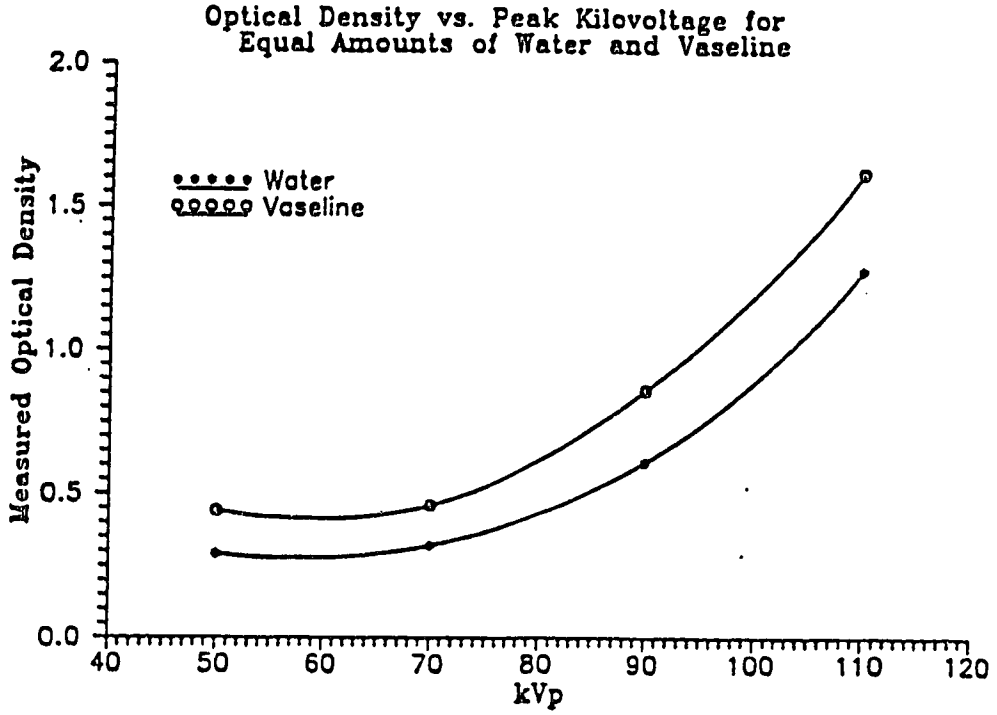

Fig. 7 Optical density measurements show that water and petroleum jelly have similar attenuation characteristics.

Throughout these studies the film-screen combination used was that normally used in the fluoroscopy section of the Department of Radiology and Diagnostic Imaging at the University of Alberta Hospitals. This consisted of Kodak TMG-1 films and Lanex Regular screens. The film processor was a Kodak M6AW processor operated at a nominal 95°F with a 20s immersion time. The chemistry employed was Dupont HSD.

Film densities for the early experiments were read with an X-Rite 331 B/W transmission densitometer. This densitometer was used with a 1 mm diameter exit aperture. It is battery operated. The manufacturer's

operation manual states that the accuracy of this densitometer is better than ± 0.02 Optical Density (OD) Units and the precision is better than ± 0.01 OD Units. This manual also states that there is a maximum zero level drift of 0.02 OD Units over an 8 hour period.

Optical densities in later experiments were measured with a Therados RFA-3 water tank dosimeter/scanning densitometer. The scanning motion of this densitometer is driven by the RFA-3 control unit. This unit both drives, and also reads the voltages from, the densitometer diode. The densitometer voltages were passed along with x,y coordinate voltages to a Hewlett Packard HP7090A plotter/data collection unit which in turn transferred the information to an IBM XT clone. A Pascal program stored the information in a file of data records.

This densitometer is configured such that the film to be scanned is laid on a piece of optically flat glass. An arm carries the density measuring apparatus such that the light source is held to one side of the glass and the photo sensitive diode is held to the other. Thus the light passes through the glass and the film before being received by the diode. Films were aligned via markers stuck to the glass.

It is important to note that over the 24 cm width of the film, a 1000 point scan along the x axis corresponded to a spacing of ~0.25 mm/point. This was less than the 1mm diameter diode aperture used, so the field was in fact over sampled. This contrasts sharply to the y direction sample spacing. In the y direction, the controller only allowed one to choose between a 1 mm spacing over a 56 mm total scanning distance or a 1 cm spacing over 56 cm. To incorporate the entire 30 cm length of the film a 1 cm spacing was used in the y direction. A schematic of the scanning protocol is shown in Fig 8. A

FILM SCANNING PATTERN

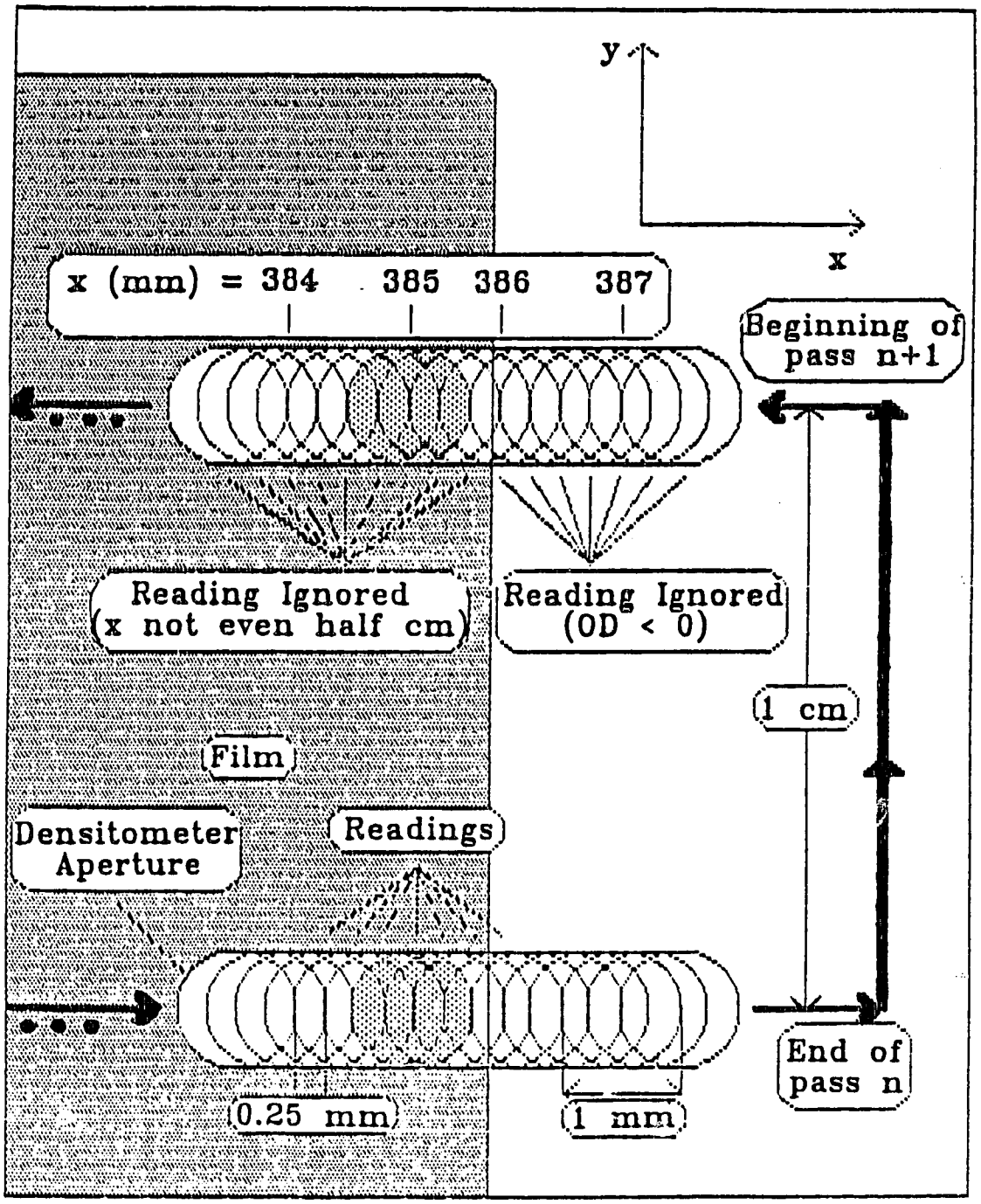

Fig. 8 The raster scanning motion and oversampling of the scanning densitometer.

description of the scanning system can be obtained from the Cross Cancer Institute.

2.2 Preliminary Experiments

2.2.1 Introduction

In order to better understand the specific equipment being used and the processes involved, a series of preliminary investigations where undertaken:

- to investigate the relationship between x-ray tube potential (kVp) and contrast sensitivity
- to investigate the relationship between x-ray tube current (mAs) and contrast sensitivity and
- to establish the physical dimensions of the fluoroscopy equipment; ie the source to object distance and the object to detector distance.

It was also discovered that the non-uniformity of the x-ray exposure to the film significantly influenced the measured optical density of the film. This was perceived to be a potential obstacle to the goal of optimizing the contrast sensitivity of the imaging process. Thus the affects of two factors known to be related to field non-uniformity were studied: the source to object distance and the placing of a collimating grid between the object and the detector. These five investigations are the subject of this section.

2.2.2 Fluoroscopic Geometry

This experiment measured the distance between the x-ray tube focal spot and the table(source to object distance or SOD) and also the distance between the face of the image intensifier assembly and the spotfilm (object to detector distance or ODD). An image of the alignment phantom (Fig 4) was obtained with the image intensifier assembly face next to one end of the phantom and the other resting on the table. By measuring the relative magnifications of the radio-opaque objects embedded at each end, and using simple properties of similar triangles, two equations involving the two unknowns, SOD and ODD, were solved. The calculated values for SOD and ODD are 391.5 ± 28.1 mm and 63.1 ± 17.2 mm respectively.

2.2.3 kVp vs. Contrast Sensitivity

Although the characteristic curve is a property only of the film-screen combination used, similar and related curves can be obtained by plotting OD vs. step wedge thickness for a given material. The maximum slope of such a curve is called the effective gamma for that material at the kVp used. To measure small amounts of calcium salts in SPNs, one needs to maximize the contrast sensitivity of the detection system. This corresponds in real terms to increasing the effective gamma of the system. It has long been known that effective gamma increases for all object materials as kVp decreases. Although the changes in gamma that were observed were expected, the effect of the nonuniformity of the x-ray field emitted from the x-ray tube was not.

The first experiment was performed using the pill bottle phantoms (see fig. 9). These were set atop the 2 water block phantoms and films were taken at 50, 60, 70, 80, 90, 100, and 110 kVp. The height of the image intensifier assembly above the table was held constant. The automatic exposure control devices (AECs) were used to regulate mAs. These are simply ion chamber radiation detectors that measure the exposure to the film and turn off the x-ray beam when a proper exposure has been reached. They are set for the film-screen combination in use. A grid was also employed to reduce scatter. The small focal spot was used to reduce penumbra and film-screens and processing were as described previously. Optical densities were measured at three randomly selected locations within the image of each of the four pill bottles. Results are displayed in Fig 10.

The immediately obvious feature of this graph is that optical densities for the pill bottle phantoms do not vary linearly with Ca salt concentration as expected. This may be partially due to the leveling off of the characteristic curve at the shoulder or heel. However, the slope changes from the expected negative slope to a positive slope over some portions of the curves. This cannot be accounted for purely in terms of the leveling off of the characteristic curve. Neither is it likely caused by fitting the data with a cubic spline, since the curves vary in a uniform way, as a family of curves. However, since the variation between optical densities in these curves is so small, a linear fit would fit to within the 0.02 OD error in measurement. Therefore this data does not eliminate the possibility that the change in the sign of the slope is due to random fluctuation.

ANALOG RADIOGRAPHY GEOMETRY

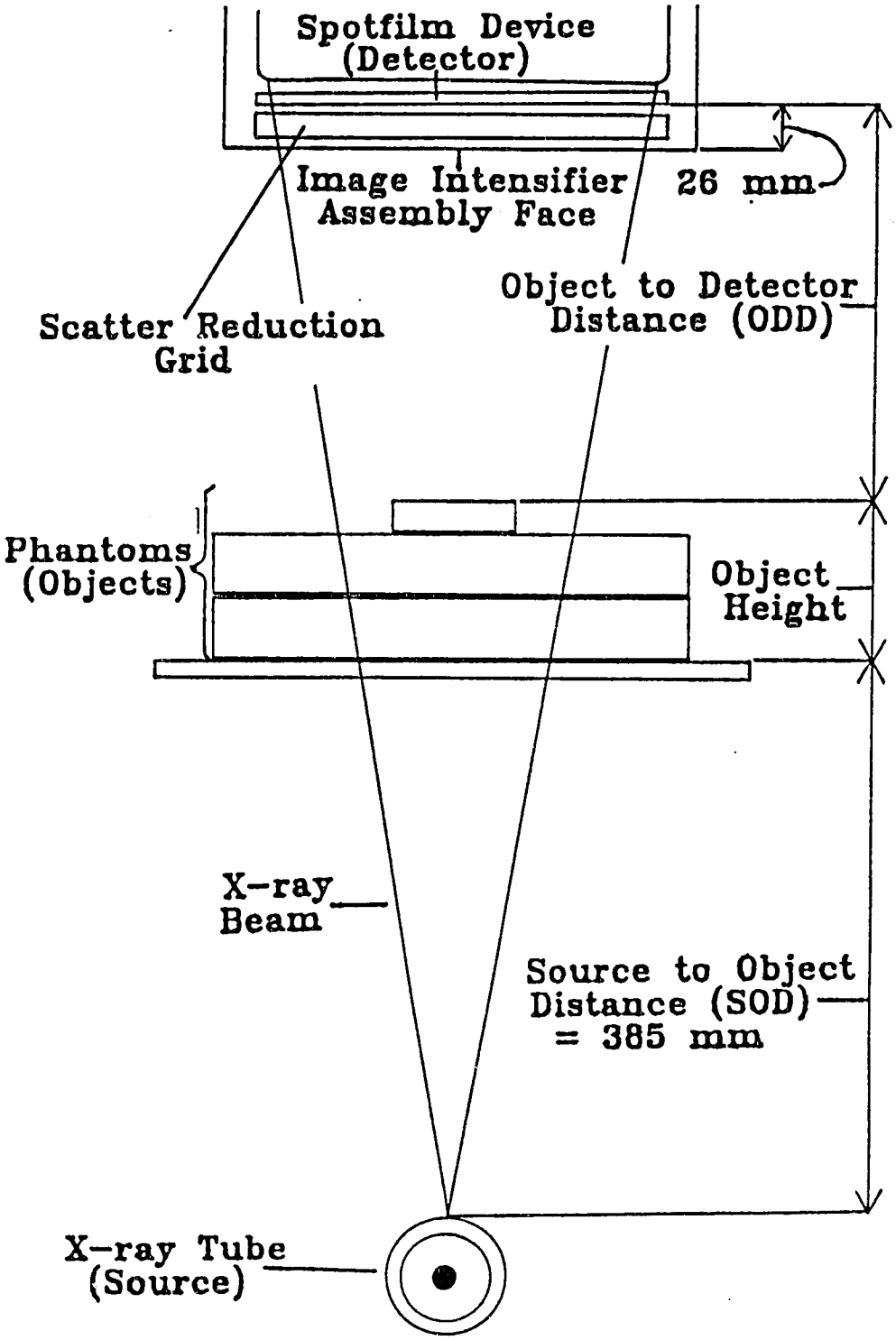

Fig. 9 The geometry employed for analog radiography experiments.

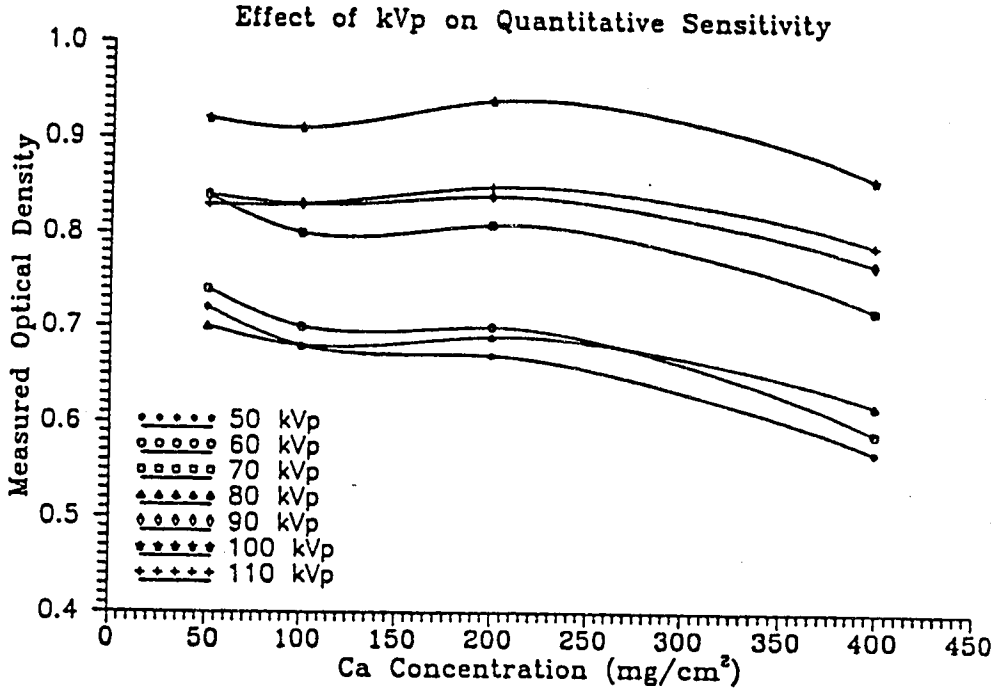

Fig 10 Detection curves at various kVp show anomolous changes in the slope.

To test for this possibility the 11 step aluminum step wedge was imaged. With thicknesses ranging from 5 to 35 mm of aluminum, this wedge would provide a much greater range of optical densities. The experiment consisted of imaging the step wedge, placed on the water block phantoms, at 50,60,70,80,90,100 and 110 kVp. Identical imaging conditions to those for the pill bottles were used. The results are shown in Fig 11.

All the curves in Fig 11 have been renormalized to start at the same point, 2.5 OD at 5 mm Al. The relationship between kVp and contrast is readily apparent from this graph, as the kVp is lowered the slope of the linear portion of the curve decreases (increases in the negative sense) providing better contrast sensitivity, as was expected.

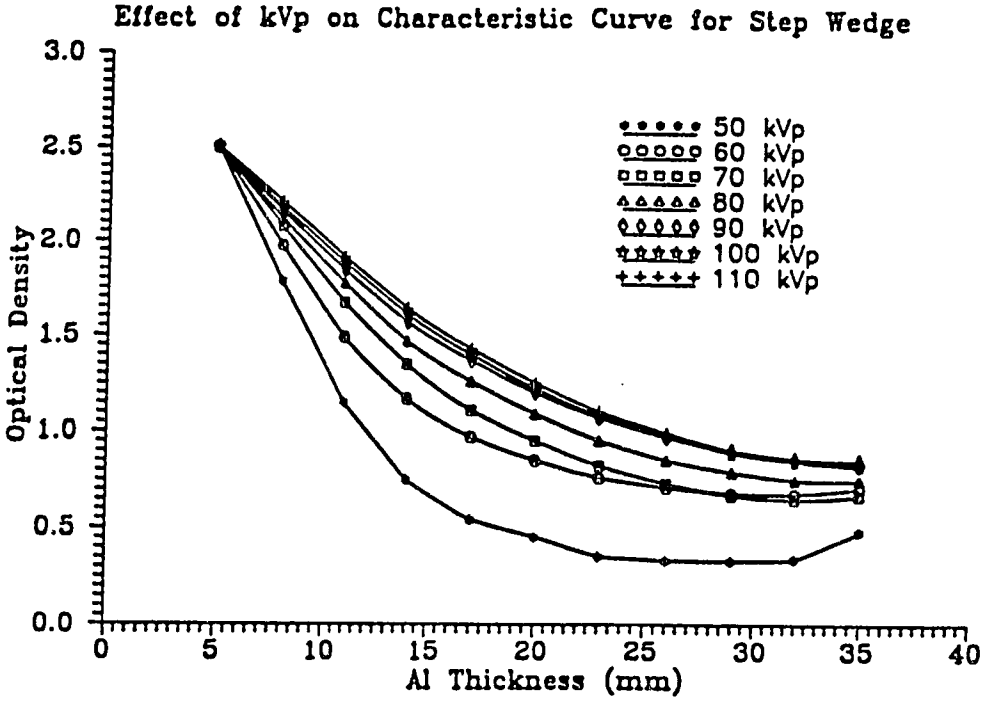

Fig 11 The slope of the linear portion of the curves increases as kVp decreases.

However, once again we observe an unexpected phenomenon in a few of the curves where slope becomes positive at the greatest thicknesses. This effect is most pronounced for the thickest parts of the step wedge at 50 kVp. This jump of 0.10 OD is too great to be attributed to measurement error (approx. 0.02 OD).

Further proof of irregularity is provided by the raw data for the graph in Fig 11. Samples of this data are provided in Table 2.

Table 2 Data for kVp vs. OD for 20 mm Al

Energy (kVp)	Measurement (OD) 1	2	3	mean
50	0.56	0.47	0.47	0.50
60	0.56	0.49	0.49	0.51
70	0.76	0.71	0.72	0.73
80	0.81	0.77	0.78	0.79
90	0.81	0.79	0.80	0.80
100	0.89	0.88	0.87	0.88
110	0.96	0.96	0.96	0.96

Measurements 1, 2, and 3 were taken at equal intervals across the image of the 20 mm thick step. Especially noticeable at lower energies is the consistently higher first measurement. All measurements were taken far enough from the edges to avoid penumbra effects. This trend was present for other steps on the wedge as well.

This can only imply that portions of each step were more exposed than others. Since:

(2.2.6) $$N = N_0 \times (1\text{-atten.fraction})$$

this result means that some areas of the object had a greater photon flux than others. The inhomogeneity of the field is the cause for the anomalous results obtained.

This inhomogeneity in x-ray fields produced by bremsstrahlung in thick targets is well known, and even utilized in diagnostic radiology. Field inhomogeneity is, however, a very major obstacle to overcome in quantifying calcium salts since the OD variation it creates is of the order of the signals produced by significant levels of calcification.

2.2.4 mAs and Contrast Sensitivity

At the same time as the kVp vs. contrast experiments were performed, similar experiments to deduce the influence of mAs on contrast were performed. Again, the results of these experiments were readily predictable; mAs would not affect the contrast of large objects significantly unless it pushed the optical densities of interest onto the toe or the heel of the characteristic curve.

To verify this result the 6 step aluminum step wedge was placed upon two 6 cm thick water block phantoms and imaged at 34 (selected by AEC), 40, 45, 50, 55, 60, 65 and 70 mAs. All of these images were taken at 50 kVp. The wedge had steps of 0.5, 1, 2, 3, 4, and 5 mm thickness and was only 6 cm long (1 cm/step). It was used so that the field would vary less over it than it had for the larger 11 step aluminum wedge. Four pill bottle phantoms with concentrations of 0, 50, 100, and 400 mg/cm^2 were also imaged at the same time to provide an estimate of the equivalence between the x-ray attenuation of the tribasic calcium phosphate and aluminum.

The films, screens, and processing for the eight images were the same as before. Optical density was read at three points across each step in the wedge, one near each edge of the step and one at the center. Likewise optical density was read at three points within the image of each of the four pill bottle phantoms. The results for the step wedge are plotted in Fig 12, representative pill bottle results in Fig 13. The lines in Fig 12 were fitted by linear regression, and their slopes are shown in Table 3.

Table 3 Slopes of mAs vs. Al Thickness Curves

mAs	slope
34	-0.131507
40	-0.128822
45	-0.148384
50	-0.155452
55	-0.160000
60	-0.162356
65	-0.167781
70	-0.177890

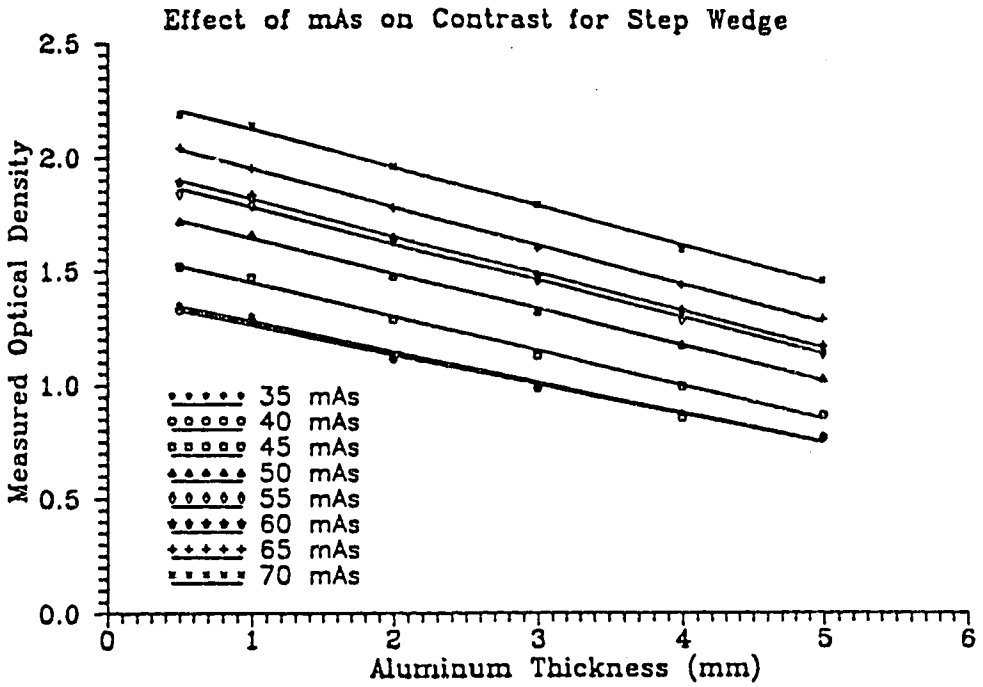

Fig. 12 The lines appear similar, but statistical analysis shows a significant change in slope with mAs.

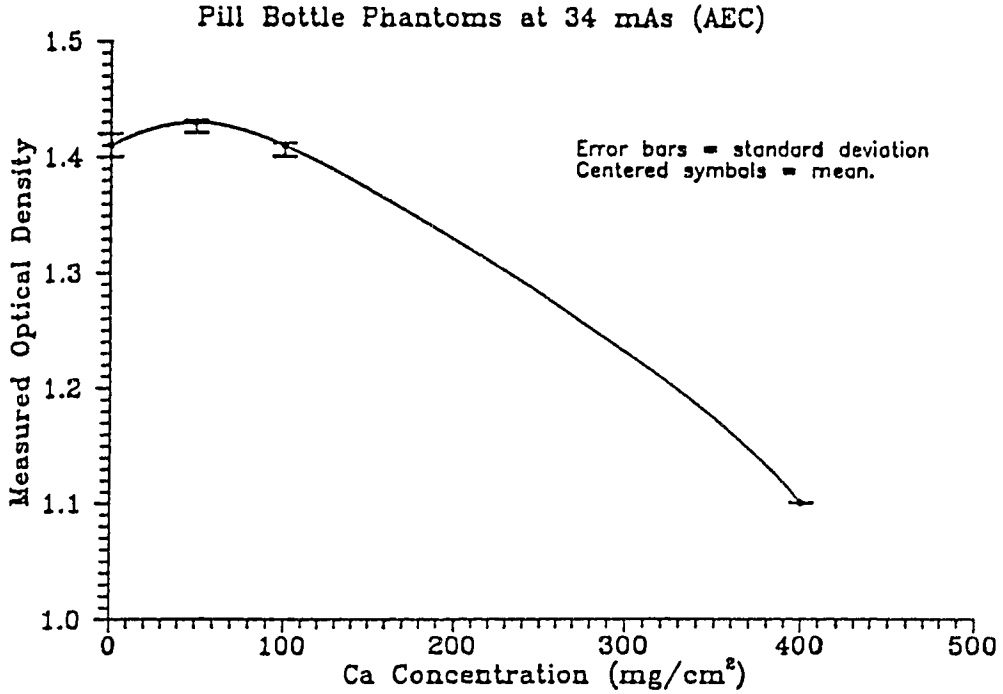

Fig. 13 mAs experiments using pill bottle phantoms produced anomolous curves like those for kVp.

Analysis of variance was performed on these slopes to test the validity of the hypothesis that the slope of the characteristic curve is unchanged by changes in mAs. The analysis shows a highly significant type one error for the null hypothesis that these slopes are the same. The reason for this is simply that changing the mAs shifts the characteristic curve. Thus, at lower mAs, such as 34 mAs, we are imaging closer to the toe of the curve, and have a smaller slope and consequently less contrast than at higher mAs. Fig 12 shows that the effect is slight, especially in comparison to the effect of kVp.

Figure 13 is representative of the pill bottle phantom data. It shows the characteristic noted earlier; a change in the sign of the slope for a set of phantom concentrations. This again demonstrates the problem of field inhomogeneity and the effect that it has on contrast detectability. This is obviously a problem that must be overcome in order to correctly quantify calcification in SPNs.

2.2.5 Object Detector Height and Scatter Reduction Grids

Two related factors that can influence field uniformity are imaging distance and the presence of scatter reduction grids. Imaging distance plays a part because the inherent nonuniformity of the bremsstrahlung field can be minimized by reducing the source to object distance (SOD) until the field is magnified to the point where the inhomogeneity of the field is of the order of the measurement error, in much the same way as the surface of the earth appears flatter as we get closer to it.

The use of grids can lead to a phenomenon known as grid cutoff. Scatter reduction grids are used to ensure that only x-ray photons travelling along rays from the source to the detector are detected. Photons travelling in other directions are absorbed by the lead interstices. Since the source is small in comparison to the detector (film) the x-ray photons do not travel in parallel paths and grids must be made to 'focus' at a certain distance (see Fig 14). When the source to film distance is not the focal length of the grid, the grid will absorb not only the scattered radiation, but portions of the primary beam as well (see Fig 15). This is known as grid cutoff.

To measure these effects, two 6 cm thick water block phantoms were imaged at table to grid distances of 20, 25, 30, 35 and 40 cm both with and without the use of the grid(the source to table distance is fixed at 38 cm). The images were made at 50 kVp and exposure was controlled by the AEC devices. Films were processed as usual. Optical density was measured along and perpendicular to the anode cathode axis at 2 cm intervals.

The results are shown in Figure 16. The expected flattening of the field is evident, however, even at maximum distance (40 cm) the field is not flattened enough to be considered homogeneous. Figures 17 through 19 show how the optical densities on the image in the direction perpendicular to the anode-cathode axis are altered by the presence of a grid. This is because the grid interstices are parallel to the anode cathode axis. The image taken at 30 cm table top to grid distance shows there is minimal distortion of the field. This then would approximately correspond to the grid focal distance. In order to prevent grid cutoff, therefore, images taken with the grid on this system should be taken

FOCUSSED GRID

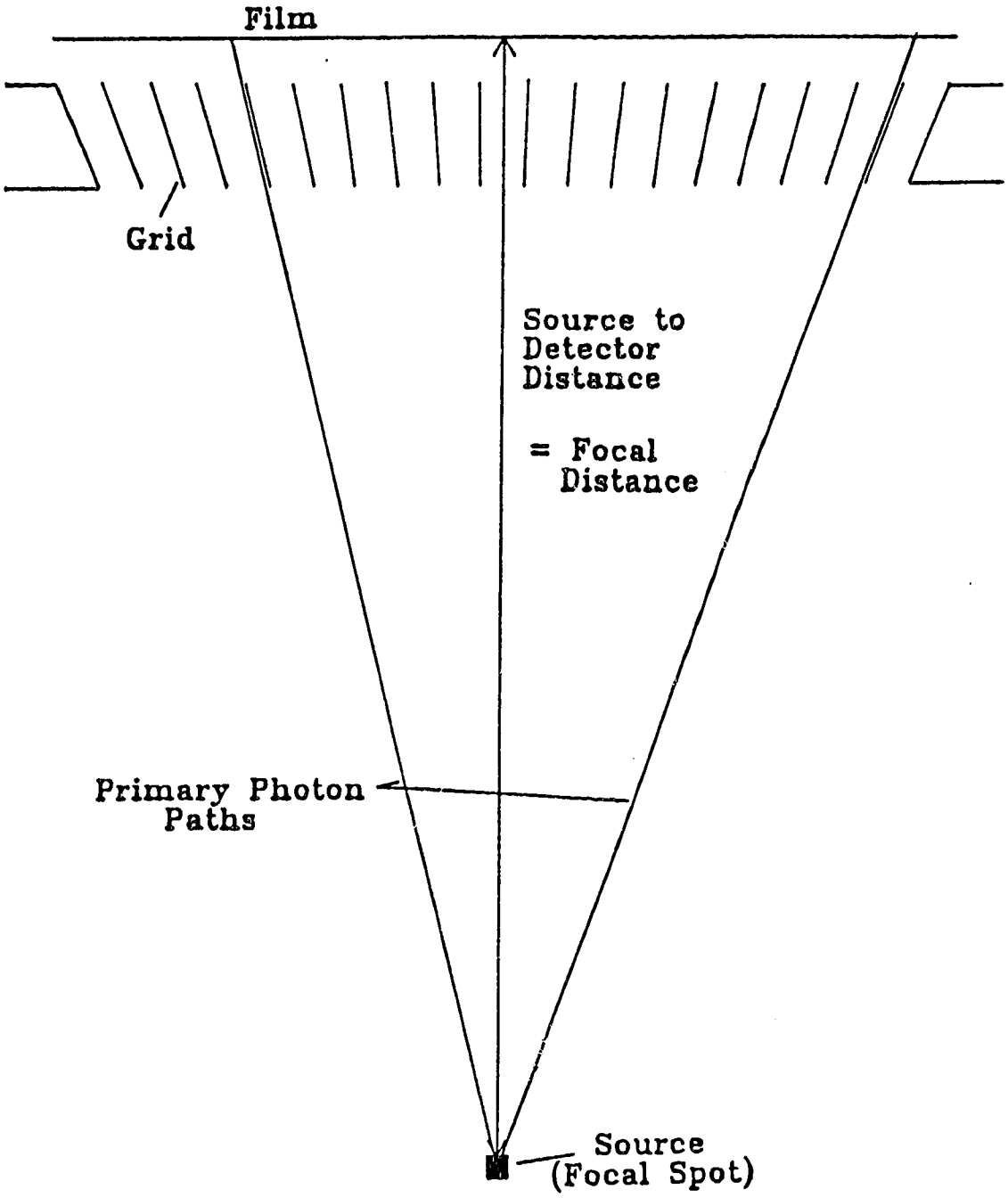

Fig. 14 A focussed grid does not alter the exposure field.

GRID CUTOFF

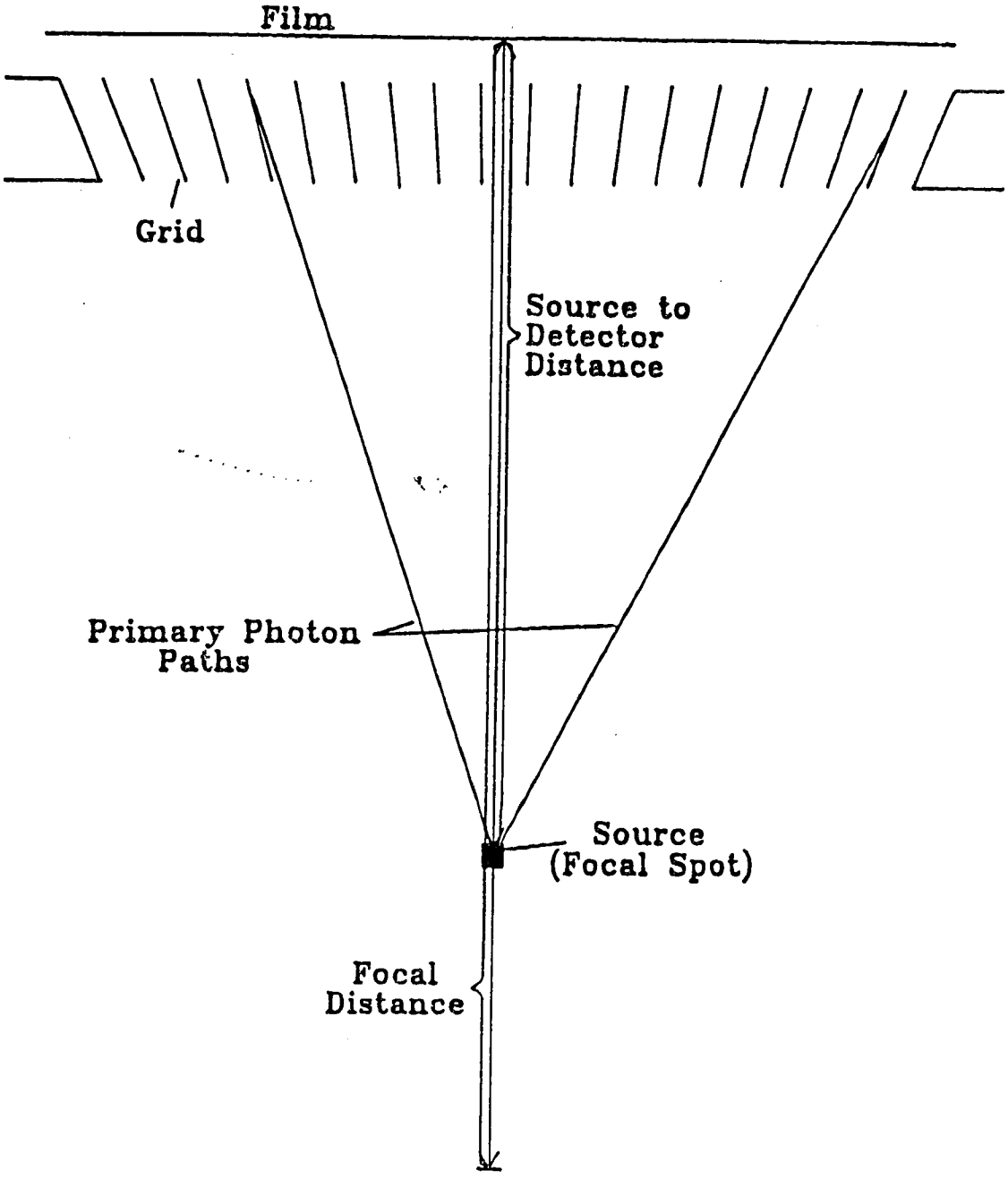

Fig. 15 An unfocussed grid absorbs primary photons and alters the exposure field.

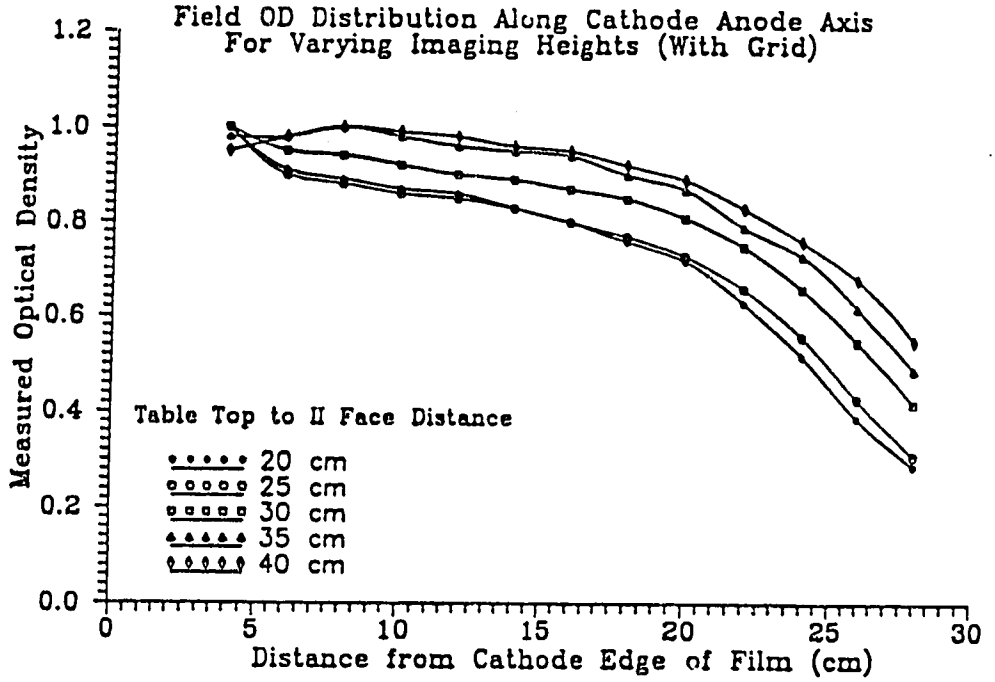

Fig. 16 As expected, the exposure field is flattened by increasing the source to image distance.

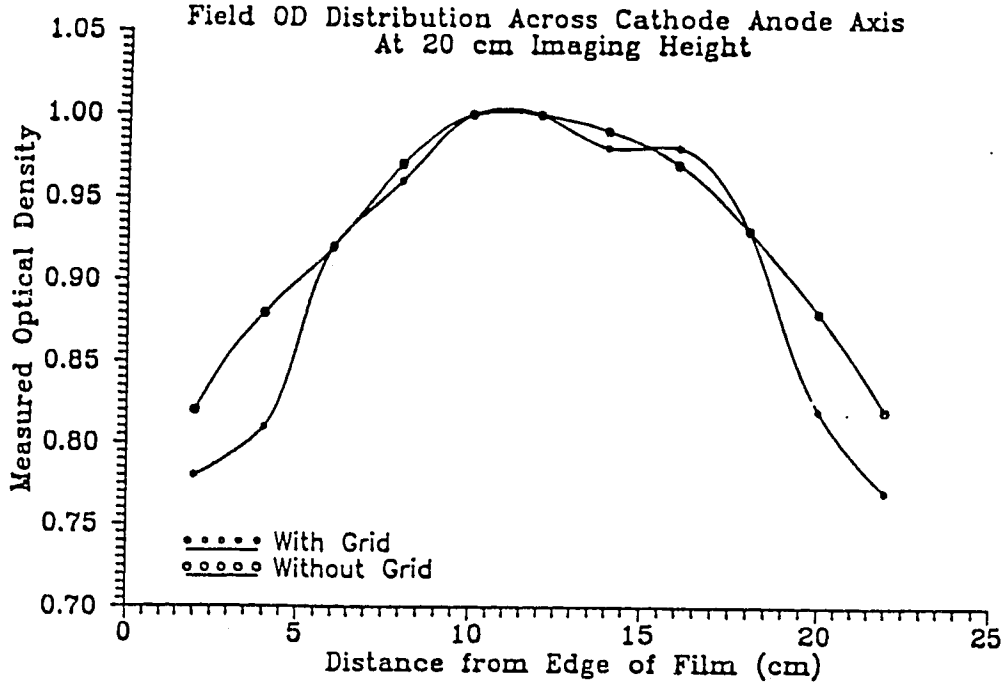

Fig. 17 At 20 cm table to II face distance, the grid absorbs some of the x-rays at the edge of the field.

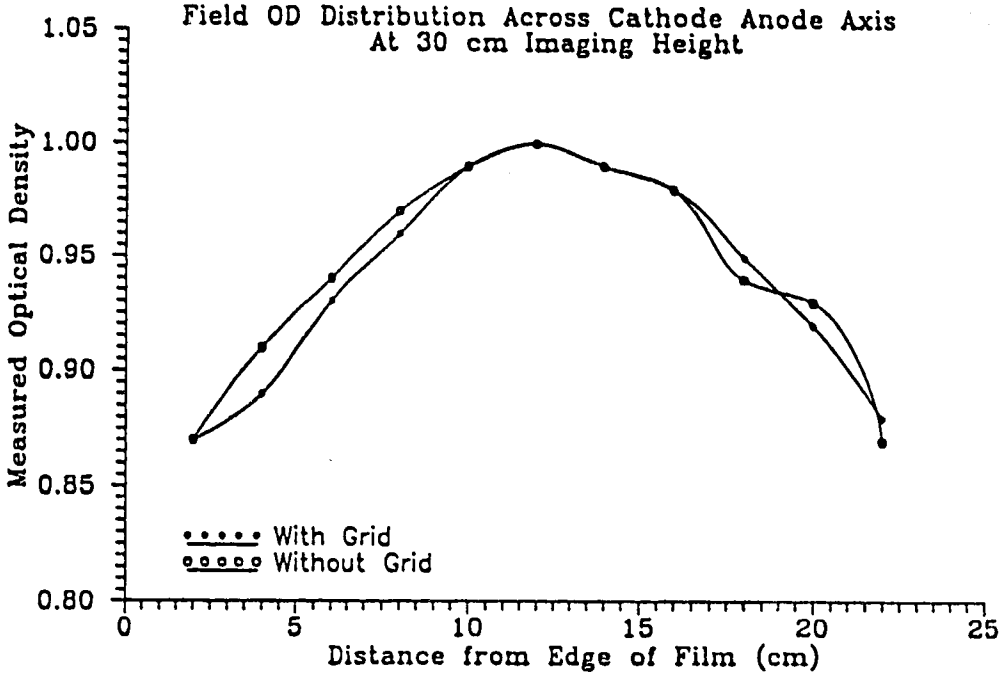

Fig. 18 At 30 cm table to II face, the grid is approximately properly focussed.

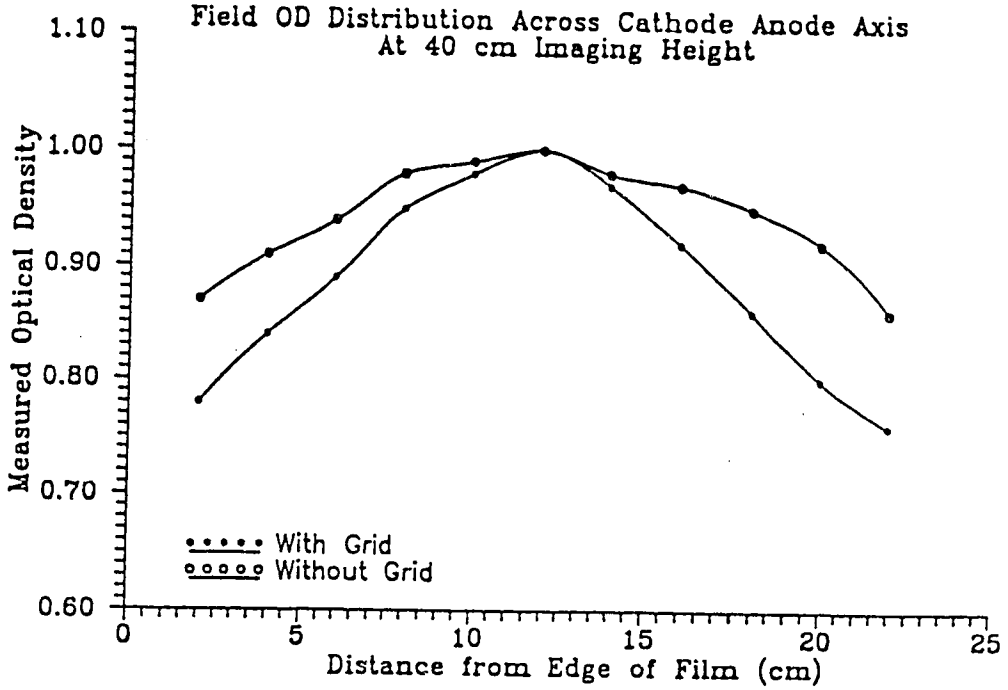

Fig. 19 At 40 cm the unfocussed grid is again absorbing radiation at the edges of the field.

with the image intensifier face at approximately 30 cm distance above the table top.

Clearly, though, varying the geometry will not be enough in itself to produce a uniform image field. kVp investigations showed that imaging should be done at the lowest kVp to increase contrast, as expected. mAs selection is not critical, but care should be taken to expose the film in the linear region of the characteristic curve. Images should be taken at 30 cm table top to image intensifier face distance to avoid grid cutoff. But even though the imaging parameters can be optimized, they do not eliminate the inhomogeneity of the field and parameter optimization will be of no avail if optical densities at different parts of the image cannot be directly compared. This problem is addressed in the next section.

2.3 Film Subtraction

2.3.1 Introduction

In order to use film radiography to measure the calcium content of SPNs an "overlay phantom" is useful. Such a phantom would be placed on the patient so that phantom and SPN would be imaged simultaneously. Measurements of the optical densities for the known calcium concentrations in the phantom would provide a calibration curve. By matching the optical density measured for the SPN one could then obtain a calcium quantity for the SPN.

However, if the image exposure field is not uniform, the optical densities at various portions of the film cannot be directly compared. In order to make the field more uniform film subtraction can be used. In film subtraction, two films are exposed: the image and the mask that will be subtracted from the image. A negative film is made from the mask, ie, a film in which the optical densities are reversed. This negative is overlaid onto the image film and these in turn are used as a mask for the resultant film, which is the subtracted image. Thus, by making a mask film of the exposure field, we can subtract this field from the patient image to eliminate (in theory) the field inhomogeneities.

A mathematical justification for the heuristic argument above will now be presented. If $I_0(x,y)$ is the intensity of visible light incident on a film at coordinates (x,y), and $I_t(x,y)$ is the intensity of the transmitted light, then:

$$(2.3.1) \qquad OD(x,y) = \log_{10}[I_0(x,y)/I_t(x,y)]$$

is the definition of the optical density of the film at position (x,y). We also know that on the linear part of the characteristic curve the optical density of an exposed film can be approximated by:

$$(2.3.2) \qquad OD(x,y) = \gamma \log_{10} k \int_0^{Emax} N(E,x,y)dE + const$$

where: γ = slope of characteristic curve

k = film-screen photon conversion ratio

N(E,x,y) = the number of x-ray photons detected at position (x,y) with energy E

Emax is the maximum energy (kVp) of the beam

and the constant represents the base + fog density

To a good approximation it is true that the energy spectrum of the beam does not change over the solid angle subtended by the film, so that:

$$N_0(E,x,y) = N_0(E)\cdot f_0(x,y) \tag{2.3.3}$$

where the subscript 0 indicates that this is the x-ray distribution with no object in the beam. The validity of (2.3.3) will be discussed later in this chapter.

Now, for the mask, we capture the exposure field in the image. Using equation (2.3.2) the optical density for this is:

$$OD_m(x,y) = \gamma_m \log_{10} k_m \int_0^{Emax} N_0(E,x,y)dE + \text{const} \tag{2.3.4}$$

where the subscript m indicates values for the mask film. Rearranging equation (2.3.1) we see that the visible light transmitted through the developed mask film is:

$$I_{tm}(x,y) = I_{0m}(x,y)/10^{OD_m(x,y)} \tag{2.3.5}$$

This is the portion of the visible light that will expose the negative of the mask. Since in Eq (2.3.2) k multiplied by the integral of N(E,x,y) represents the total number of visible photons produced by the screen to expose the film, this equation can be adapted to the case of a film exposed to visible light. By replacing the visible photons from the screen in Eq (2.3.2) with the visible photons transmitted through the mask onto the negative one obtains:

$$(2.3.6) \qquad OD_n(x,y) = \gamma_n \log_{10}[I_{tm}(x,y)] + \text{const}$$

where the subscript n indicates the values for the negative of the mask film.

Placing an object in the x-ray beam will cause attenuation and, ignoring scattered x-rays, lead to a resultant x-ray beam of:

$$(2.3.7) \qquad N_i(E,x,y) = N_0(E,x,y)e^{-\Sigma[\mu(E)l(x,y)]}$$

where:

$\mu(E)$ = the linear attenuation coefficients of the materials in the attenuating body

$l(x,y)$ = the corresponding path lengths of the x-rays through the attenuator.

the subscript i denotes values for the image film.

The resultant (subtraction) film is exposed by the visible light that is transmitted first by the mask negative and then by the image

film. Thus, the incident intensity of visible light on the subtraction film is:

$$(2.3.8) \qquad \begin{aligned} I_{0s}(x,y) &= I_{0i}(x,y)/10^{OD_i(x,y)} \\ &= I_{tn}(x,y)/10^{OD_i(x,y)} \\ &= I_{0n}(x,y)/10^{[OD_i(x,y)+OD_n(x,y)]} \end{aligned}$$

where the subscript s denotes the subtracted image film.

This would produce an optical density distribution on the subtracted film of:

$$(2.3.9) \quad OD_s(x,y) = \gamma_s\{\log_{10}[I_{0n}(x,y)]-OD_i(x,y)-OD_n(x,y)\}$$

Combining (2.3.7) and (2.3.2) we obtain:

$$(2.3.10) \quad OD_i(x,y) = \gamma_i \log_{10} k_i \int_0^{Emax} N_0(E,x,y) e^{-\Sigma[\mu(E)l(x,y)]} dE + const$$

Substituting (2.3.4) and (2.3.5) into (2.3.6) we get:

$$(2.3.11) \quad OD_n(x,y) = \gamma_n \left[\log_{10}[I_{0m}(x,y)] - \gamma_m \log_{10} k_m \int_0^{Emax} N_0(E,x,y) dE \right] + const$$

Substituting (2.3.10) and (2.3.11) into (2.3.9) and gathering together all the constant terms yields:

$$(2.3.12)\quad OD_s(x,y) = \gamma_s\Big[\log_{10}[I_{0n}(x,y)/(I_{0m}(x,y))^{\gamma_n}] - \gamma_i\log_{10}\int_0^{Emax} N_0(E,x,y)e^{-\Sigma\mu(E)l(x,y)}dE + \gamma_n\gamma_m\log_{10}\int_0^{Emax} N_0(E,x,y)dE\Big] + \text{const}$$

Now if we substitute (2.3.3) into (2.3.12) we have:

$$(2.3.13)\quad OD_s(x,y) = \gamma_s\Big[\log_{10}[I_{0n}(x,y)/(I_{0m}(x,y))^{\gamma_n}] - \gamma_i\log_{10}\int_0^{Emax} N_0(E)e^{-\Sigma\mu(E)l(x,y)}dE + \gamma_n\gamma_m\log_{10}\int_0^{Emax} N_0(E)dE - \gamma_i\log_{10}[f_0(x,y)] + \gamma_n\gamma_m\log_{10}[f_0(x,y)]\Big] + \text{const}$$

Thus if γ_i and $\gamma_n\gamma_m$ can be made the same, the dependence of the final subtracted image on the initial distribution of photons, $f_0(x,y)$, can be eliminated. This is generally possible since the same film-screen combination can be used for both mask and image films. This means that γ_i can be made equal to γ_m. A film with $\gamma \simeq 1$ is then used for the negative film with the result that the initial field non-uniformity is removed from the subtracted image. This treatment, however, is based on ideal steps in the subtraction process. The effects of non-ideal conditions is measured empirically in the next section.

2.3.2 Film Field Subtraction

To test the viability of actual film subtraction methods, two x-ray films were made, one with two water blocks and the ring phantom (the image film) and the other with only the water blocks (the mask film). Both were taken at 50 kVp with the use of the AEC devices. Lead numbers were placed on the water block phantoms for both films so that the films could be easily aligned for subtraction. Exposures and processing of all films were done within minutes so as to minimize variation in time dependent parameters.

A negative was made of the mask and subtraction films were produced for both the mask-negative and mask-image combinations. The films used were Kodak SUB for subtraction masks and Kodak SPF for subtraction images. The visible light source was a Newark CT-25 photographic lamp which acts essentially as a point source at a distance of 128 ± 2 cm from the films.

The first measurements were on both the mask and negative films. OD was measured along the anode-cathode axis at 1 cm intervals. Fig 20 shows these results. One would expect the negative and mask to vary inversely with each other. Thus, the addition of the values for these measurements should produce a constant value (to within 0.04 OD, the measurement error).

The upper line on Fig 20 represents this data. The mean value of these points is 1.924 OD and the standard deviation s = 0.019 OD. However, a close look at the points show that this variance is, in fact, not random. The values towards the edges of the film are lower in general than those in the middle. This indicates the negative may not

quite vary inversely as the mask. Further, the data shows a non-zero slope. The slope of the line is $1.49 \times 10^{-3} \pm 2.86 \times 10^{-4}$ OD/cm.

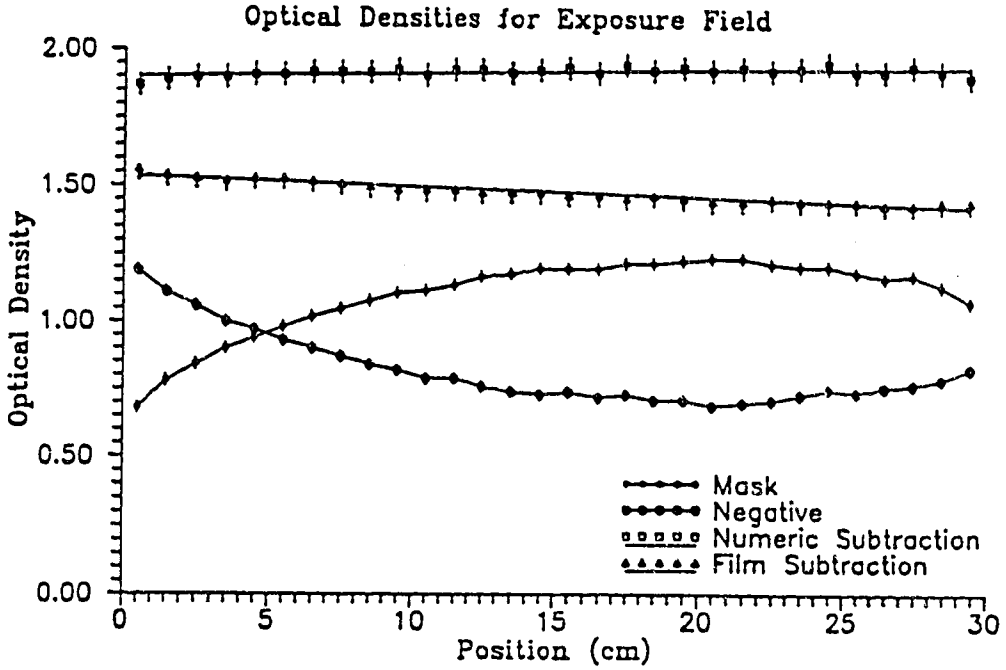

Fig. 20 Subtraction greatly improves field uniformity.

It is important to know if this slight variation has any affect on the actual film subtraction. To test this the mask-negative subtraction film was measured in the same manner as the negative and mask films had been measured. This is represented by the lower line on Fig 20. Since the subtraction is printed on reversal film, the line has a slightly negative slope of $-3.67 \times 10^{-3} \pm 2.14 \times 10^{-4}$ OD/cm. One can also see a pronounced pattern in the data points, the end points higher than the best fit line, the mid points lower.

Nonetheless, this effect contributes only about 20% of the uncertainty in measurement due to the densitometer alone. If this is the extent of the error induced by film subtraction, it will not be of major significance. A more realistic evaluation of the effects of

subtraction is the subtraction of a mask negative from an image which is not the mask. Such an experiment was performed. The mask was an image of two water block phantoms taken at 100 keV with an AEC controlled exposure. The negative was made as described above. The image was that of the ring phantom on top of the two water block phantoms. Subtraction films were made for both the negative-mask and the negative-image combinations. Table 4 summarizes the films:

Table 4 Films Made for Image Subtraction

Film	Made by
Mask	X-ray spotfilm of water block phantoms.
Negative	Negative print of mask film.
Mask-Negative Subtraction	Subtraction of negative from mask film.
Image	X-ray spotfilm of ring phantom on water block phantoms.
Mask-Image	Subtraction of negative from image film.

Measurements were made at 1 cm intervals along a line perpendicular to the anode-cathode axis and at 4.5 cm from the cathode end of the film. This allowed the ring phantom to be avoided in measurements involving the image film. The results of these measurements are shown in Fig 21 and Fig 22.

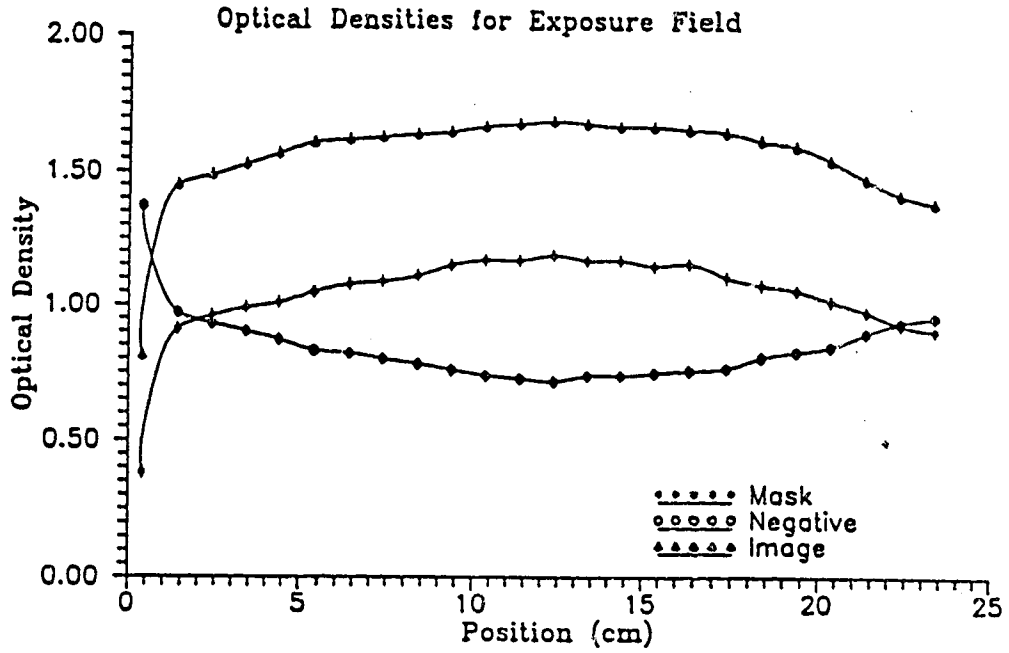

Fig. 21 Fields from two 'similar' films and the negative of one of them.

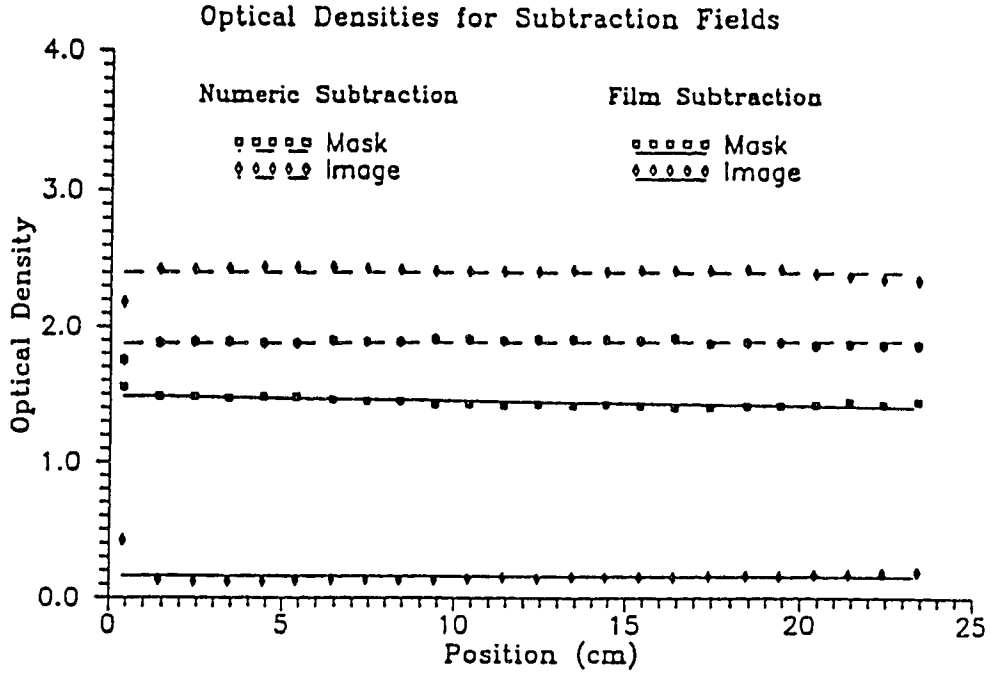

Fig. 22 The subtraction of similar films produces apparently uniform fields.

The curves in Fig 21 show the similarity between the exposure fields for the mask and the image of the phantom. The mask curve varies much as the inverse of these so one would expect good subtraction. The lines in Fig 22 represent both numerical and film subtraction of the data in Fig 21. Except for some points at the ends, the lines show that the field uniformity is good after subtraction. Table 5 below shows linear regression fit data for the lines in Fig 22.

Table 5 Statistics From Linear Regressions of Subtraction

Subtraction Type	slope (OD/cm)	error in slope	r
mask(numeric	1.06×10^{-3}	9.51×10^{-4}	0.230
mask(film	-3.23×10^{-3}	6.83×10^{-4}	-0.709
image(numeric	3.57×10^{-4}	1.59×10^{-3}	0.048
image(film	-2.96×10^{-4}	1.78×10^{-3}	-0.035

Like the data from the last experiment, the slopes are all slightly non-zero. For the image subtractions the two slopes are within their respective errors of zero, and the assumption that the field is flat appears valid. For the mask subtractions the non-zero slopes contribute little to the 0.02 OD measurement errors.

Two phenomena are notable at this point. One is the low correlation coefficients of the regressions in three of the cases. For the image subtractions the correlation coefficients produced would have better than a fifty percent chance of appearing for samples from a random population. This, however, can be explained purely by the fact that the slope is so small. The correlation coefficient measures the degree to which variation in the y variable corresponds to variation in the x variable. If the y variable is constant, then there is no variation in y and thus no correspondence with x. For lines with errors

of the order of half the range times the slope, r may not indicate the linearity of the data, since the error is comparable to the linear dependance of y on x.

Also of note is the fact that subtraction appears to flatten the image data better than the mask data (ie the slopes are smaller in the image data case). However, for both numeric and film subtraction the combined error in the slopes is greater than the differences between them.

For example, for numeric subtraction, the slopes vary by $1.64 \times 10^{-3} - 3.57 \times 10^{-4} = 1.28 \times 10^{-3}$ OD/cm between the film and the mask case. However, the combined errors in the two slopes is $9.51 \times 10^{-4} + 1.59 \times 10^{-3} = 2.54 \times 10^{-3}$ OD/cm, almost twice as great. Thus, we may consider the slopes to be the same, to within error.

Since the data is approximately constant, a more appropriate statistical analysis can be obtained by considering the mean and standard deviation of the data. One question that begs answering is whether or not there is a statistically significant increase in the error associated with film subtraction compared with that of numeric subtraction. This is the same as asking whether the standard deviations in the two cases are significantly different. Table 6 contains the standard deviations for these cases.

Table 6 Standard Deviations and Means of Subtractions

Subtraction Type	mean (OD)	Standard Deviation
mask(numeric)	1.89	1.48×10^{-2}
mask(film)	1.44	2.38×10^{-2}
image(numeric)	2.41	2.31×10^{-2}
image(film)	0.15	1.97×10^{-2}

It is, first of all, instructive to note that these standard deviations are similar to the densitometer error of 0.02. To compare the standard deviations in the numeric subtraction case with those in the film subtraction case, we make use of the statistical formula:

$$(2.3.14) \qquad P\left[\frac{\sigma_f^2}{\sigma_n^2} \leq \frac{s_f^2}{s_n^2 \times F\alpha(\theta_f,\theta_n)}\right] = 1 - \alpha$$

where: P[x] is the probability of x,

the subscript $_n$ denotes numeric subtraction values

the subscript $_f$ stands for film subtraction values

σ is the population standard deviation,

s is the sample standard deviation,

θ is the number of degrees of freedom of a sample,

α is the probability of type 1 error.

F_α is the F distribution

A type one error is the error of rejecting the null hypothesis if it is true. In this case the null hypothesis is that there is no difference between the standard deviations for the two populations. We choose α to be 0.01, which is equivalent to a two percent probability of rejecting the null hypothesis. Inserting the sample standard deviations of the mask subtractions into this formula yields:

$$(2.3.15) \qquad P\left[\frac{\sigma_f^2}{\sigma_n^2} \leq 1.07\right] = P\left[\frac{\sigma_f}{\sigma_n} \leq 1.04\right] \approx 0.99$$

This equation makes the statement that the probability of the film subtraction standard deviation being less than or equal to the numeric subtraction standard deviation is about 99%. Therefore we can conclude that the there is no significant increase in the standard deviation due to the extra steps involved in film subtraction. A similar test showed that film subtraction of the image film produced no significant increase in standard deviation when compared to film subtraction of the mask film. One can therefore use the process of film subtraction to eliminate field nonuniformity without adding statistical error.

One troubling aspect, however, was noted for the image film subtraction. When this film was viewed on a light box, there seemed to be a visible gradient in optical density from one corner to the corner diagonally opposed. Although this seemed not to affect greatly the statistical analysis of the experiment, it leads to concerns about the affect of the subtraction process over an entire field. It is all the more troubling when one considers that the optical density difference between diagonally opposed corners was 0.26 OD, over ten times as great as the error attributable to the densitometer. This is discussed in the following section.

2.3.3 Calibration Curves from Film Subtraction

It is important to determine whether or not the residual inhomogeneity in the film subtracted image is large enough to impair calcium quantification. To answer this question the optical density of

the calcium concentration in each of the rings was measured to provide a calibration curve. In order to minimize the affect of the residual inhomogeneity the optical density was measured along rays running radially through the phantom image in three different directions. Furthermore, each concentration was sampled three times along each ray.

Figure 23 displays the results of this analysis. The three curves represent the three different rays along which measurements were taken. Each point represents the average of the three samples of the calcium concentration on that ray. The error bars represent the 0.02 OD error of the densitometer. The problems introduced by the field inhomogeneity are evident. At five of the seven points the error bars do not overlap, indicating that the measurement error does not account for the differences in the observed optical densities. At no point do all the error bars overlap, which would be expected if these samples were from the same population.

To determine how significant the field nonuniformity is we can use the average of these three curves to generate a calibration curve. We can then fit this curve with a numerical Taylor expansion to second order and extrapolate the curve to obtain optical densities over a wider range of values. Zerhouni et al[4] determined that a 40 mg/ml was the concentration above which SPNs could be considered benign, so it is the change in optical density over a 40 mg/cm^2 range that we are interested in finding. Table 7 shows the Taylor coefficients for the expansion.

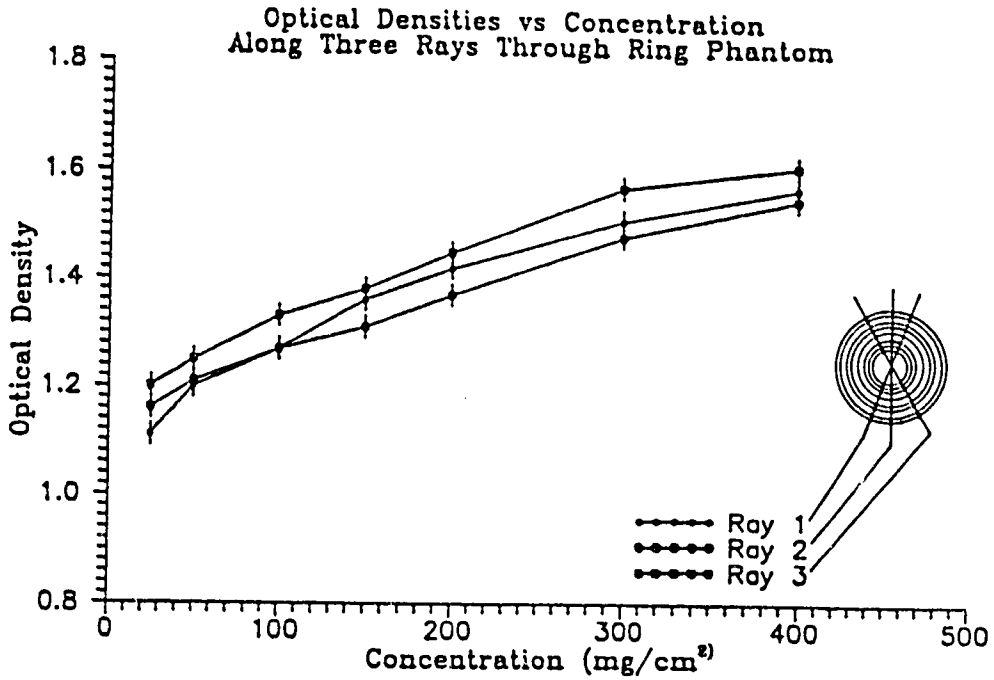

Fig. 23 Calibration curves from a film-subtracted image of the ring phantom.

Table 7 Taylor Expansion Coefficients For Ring Phantom

Ca Conc. $=x$ (mg/cm^2)	Mean OD $=f(x)$	$\Delta(f)$ $(\times 10^{-2})$	$\frac{\Delta(f)}{\Delta x}$ $(\times 10^{-3})$	$\Delta\left[\frac{\Delta(f)}{\Delta x}\right]$ $(\times 10^{-4})$	$\frac{\Delta^2(f)}{(\Delta x)^2}$ $(\times 10^{-6})$
25	1.16	-	-	-	-
50	1.22	6	2.4	-	-
100	1.29	7	1.4	-10	-13.3
150	1.35	6	1.2	-2	-2
200	1.41	6	1.2	0	0
300	1.52	11	1.1	-1	-0.67
400	1.58	6	0.6	-5	-2.5

Using these coefficients in a Taylor expansion to second order about x = 25 gives:

$$(2.3.16) \quad OD(0) = 1.16 + (0-25)\times(2.4\times10^{-3}) + (1/2)\times(0-25)^2\times(-13.3\times10^{-6})$$

$$= 1.10$$

and

$$(2.3.17) \quad OD(40) = 1.16 + (40-25)x(2.4x10^{-3}) + (1/2)x(40-15)^2x(-13.3x10^{-6})$$

$$= 1.19$$

The 0.09 OD difference between 0 and 40 mg/cm^2 of calcium is only approximately a third of the corner to corner field inhomogeneity of 0.26 OD for the subtracted film. Considering 0.09 OD as a signal to be detected and the 0.26 OD field inhomogeneity as background noise against which the signal is set produces only a 35% signal to noise ratio. In order to have reliable calcium quantification we require a signal to noise ratio of at least 100%.

However, the entire film field is not normally used for quantification. Accurate quantification may still be possible if the nonuniformity of the field is sufficiently small over the portion of the film used.

2.4 Numeric Subtraction

2.4.1 Introduction

To test for field uniformity accurately and precisely the scanning densitometer (as described previously) was used. The data obtained from the scanning densitometer was analyzed by FORTRAN, BASIC, and Pascal programs. Negative values, corresponding to readings off the film edge, were ignored by the computer. To maintain a reasonable data

pool, only data from half centimeter values of x were retained, where x = 0 cm at the beginning of the first raster pass. All values for the y direction were used. Three dimensional mesh plots of the data were made with Plot 88 (Plotworks, Inc).

This technique applied to the mask image shows the shape of the nonuniformity (Fig 24). The alignment markers and the patient ID field from the corner of the film were removed manually. An interpolation algorithm built into the plotting software has corrected for the resultant "holes" in the data.

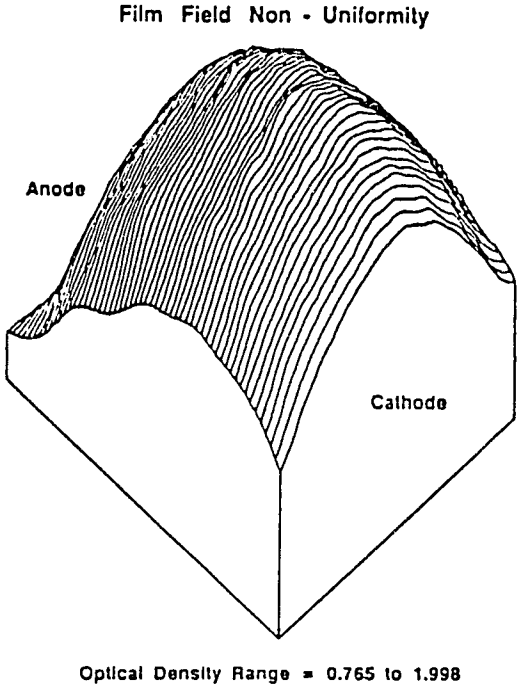

Fig. 24 A 3 dimensional representation of the field nonuniformity obtained with the scanning densitometer.

It is necessary at this point in the discussion to introduce some terminology. For this dissertation, the term 'similar' will refer to fields produced by different x-ray exposures, but with all the imaging parameters held constant. The term 'identical' will indicate fields produced by the same x-ray exposure. To illustrate, for the films of

Table 6, the mask subtractions represent subtraction of identical fields while image subtractions represent subtractions of similar films.

2.4.2 Numeric Field Subtraction

The next question which was explored was whether an OD distribution can be removed from a film by subtraction of a similar distribution. In other words, is the x-ray field reproducible or does it vary in some manner from exposure to exposure. The effect of x-ray tube anode heating was also examined. Four films were made; the first three were consecutive x-ray exposures taken with identical parameters, the fourth was made after having heated the anode of the x-ray tube by two 80 kVp, 5000 ms, 40 mA exposures (32 000 Heat Units). The heating exposures were separated by 1 a minute interval. 30 seconds after the second of these exposures the fourth image was obtained.

Each of the four films was scanned by the scanning densitometer and the data analyzed. The field produced by numeric subtraction of similar films is shown in Fig 25 and 26.

In Fig 25 the alignment artifacts have not been removed. Because the plotting package automatically scales the data in the z direction, retention of the alignment artifacts allows one to see visually the flatness of the field. Note the edge effects, which were removed in Fig 26. Fig 26 shows the finer details of the field, after the alignment artifacts have been removed. There is still some evidence of edge effects.

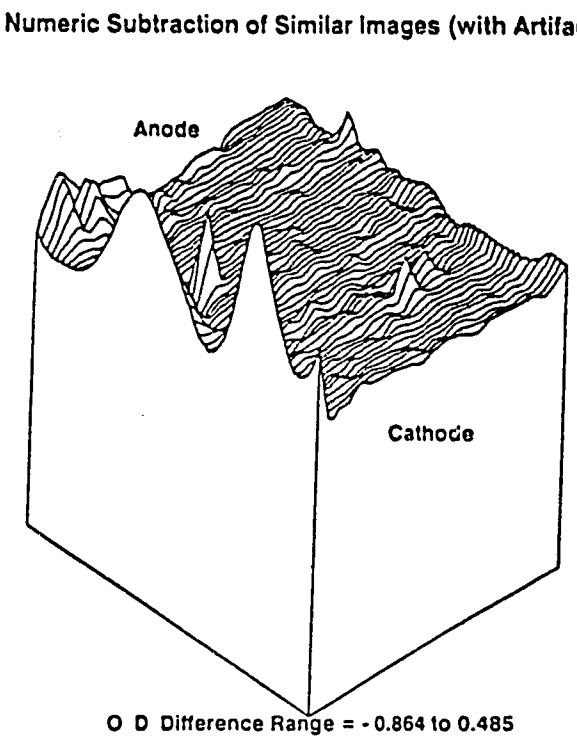

Fig. 25 Subtraction of similar films produces a field that appears quite uniform.

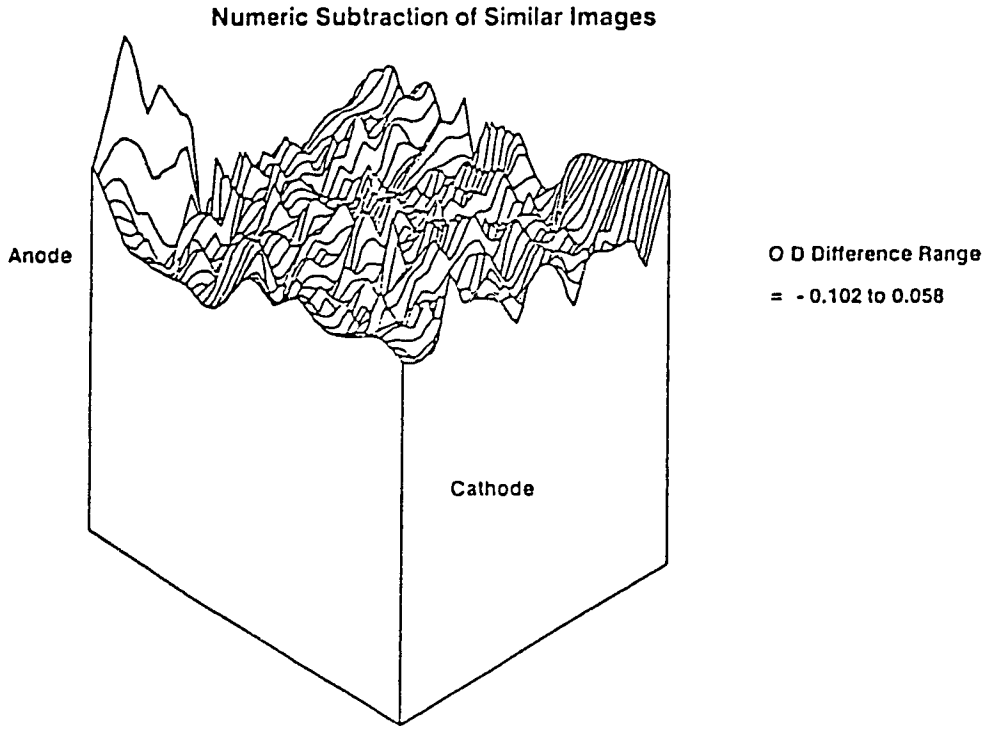

Fig. 26 After artifacts are removed, a magnified view shows substantial residual field inhomogeneity.

In order to determine the distribution of the OD values over the film the mean and standard deviation of the values was analyzed and the distribution plotted. This plot is shown in Fig 27. The mean of these data is -2.32×10^{-2} OD and the standard deviation is 1.67×10^{-2} OD. Clearly the subtraction is not producing the constant zero value expected. However, if this data is randomly distributed, then the distribution will be gaussian. For gaussian distributions, measurements separated by two standard deviations have less than a 2% probability of corresponding to the same actual value. This allows one to find 98% confidence statistical errors. Thus the total error in the measurement is $|-2.32 \times 10^{-2}| + |(2 \times 1.67 \times 10^{-2})| = 5.66 \times 10^{-2}$ or .057 OD.

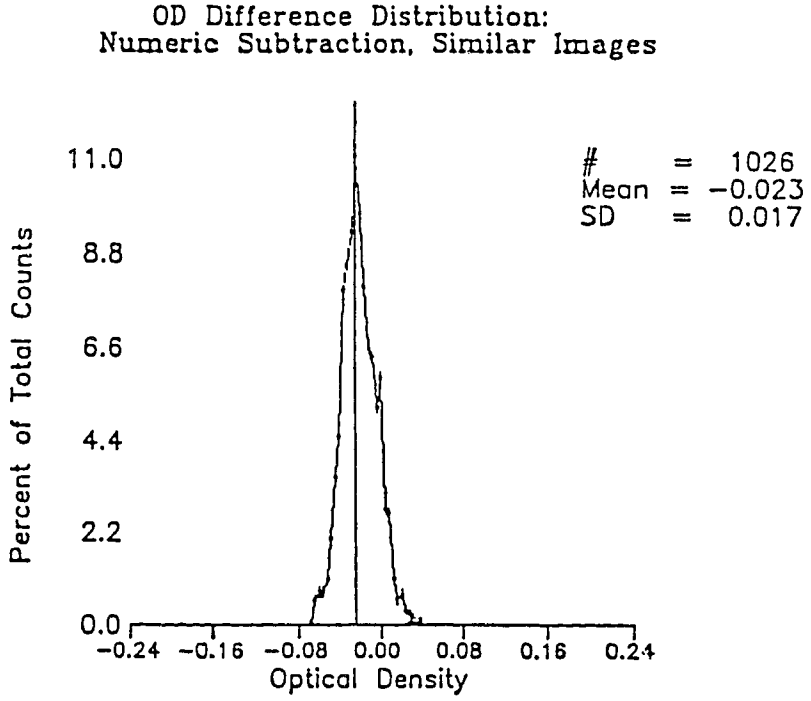

Fig. 27 The frequency distribution of optical density differences over the field appears to be approximately Gaussian, but statistical analysis reveals it is not.

This is large, but not so large that the 0.09 OD difference between 0 and 40 mg/ml concentrations of calcium are unidentifiable. To test whether this method of calculating the error is valid a Chi Square

test was performed on the distribution. The Chi square data is summarized in Table 8.

Table 8 χ^2 Statistics for OD Frequency Distribution for Numeric Subtraction of Similar Films

OD Range	Normalized Range	Expected Counts	Observed Counts	χ^2
< -0.076	< -3.104	1.3	2	0.431
-0.076 - -0.060	-3.104 - -2.225	15.3	14	0.106
-0.060 - -0.044	-2.225 - -1.345	96.0	76	4.165
-0.044 - -0.028	-1.345 - -0.465	297.1	327	3.015
-0.028 - -0.012	-0.465 - +0.415	424.4	412	0.363
-0.120 - +0.004	0.415 - 1.294	304.5	300	0.067
0.004 - 0.020	1.294 - 2.174	104.8	109	0.172
0.020 - 0.036	2.174 - 3.054	17.3	18	0.029
> 0.036	> 3.054	1.4	4	4.195
total	-	1262.0	1262	13.264

The χ^2 statistic on 8 degrees of freedom show that fewer than 0.1% of all random samples drawn from a gaussian would produce such a large value of χ^2. The conclusion that this distribution is not therefore gaussian requires that the data be analyzed in a different way to determine the error in the data. The proper method of analysis depends on the cause of the non-gaussian behavior of the optical densities. In view of the prior discussion, it seems reasonable to suppose that residual field nonuniformity is responsible for the non random nature of the OD frequency distribution.

To test this hypothesis the field was divided into a 4 x 4 matrix of areas, and these areas were statistically analyzed to determine how closely numeric subtraction produced a uniform field over different portions of the film. The data obtained from this 4 x 4 breakdown is presented in Table 9.

Table 9 Analysis of Field as a 4 x 4 Matrix

\ x= y= \	1	2	3	4
1	n = 69 $x=-5.51x10^{-4}$ $s=1.44x10^{-2}$	n = 84 $x=-1.74x10^{-3}$ $s=1.31x10^{-2}$	n = 83 $x=-6.21x10^{-3}$ $s=1.20x10^{-2}$	n = 78 $x=-1.33x10^{-2}$ $s=1.41x10^{-2}$
2	n = 75 $x=-1.50x10^{-2}$ $s=1.24x10^{-2}$	n = 96 $x=-8.58x10^{-3}$ $s=1.55x10^{-2}$	n = 84 $x=-1.96x10^{-2}$ $s=1.60x10^{-2}$	n = 90 $x=-2.40x10^{-2}$ $s=1.19x10^{-2}$
3	n = 54 $x=-2.38x10^{-2}$ $s=1.76x10^{-2}$	n = 96 $x=-1.95x10^{-2}$ $s=1.23x10^{-2}$	n = 84 $x=-2.93x10^{-2}$ $s=1.20x10^{-2}$	n = 90 $x=-2.94x10^{-2}$ $s=1.34x10^{-2}$
4	n = 55 $x=-2.90x10^{-2}$ $s=2.52x10^{-2}$	n = 77 $x=-2.90x10^{-2}$ $s=2.12x10^{-2}$	n = 84 $x=-3.53x10^{-2}$ $s=1.22x10^{-2}$	n = 84 $x=-3.00x10^{-2}$ $s=1.3x10^{-2}$

At this point it is worth noting that all the numeric subtractions between the four films in this set produced results similar to those shown above. This includes the subtractions involving the film for which the anode was heated; film 4 (see Fig 28). The only differences that occurred were in the ways the means varied from cell to cell. Whereas in Table 9 the means tend to increase as the y values increase, this was not true for other subtractions.

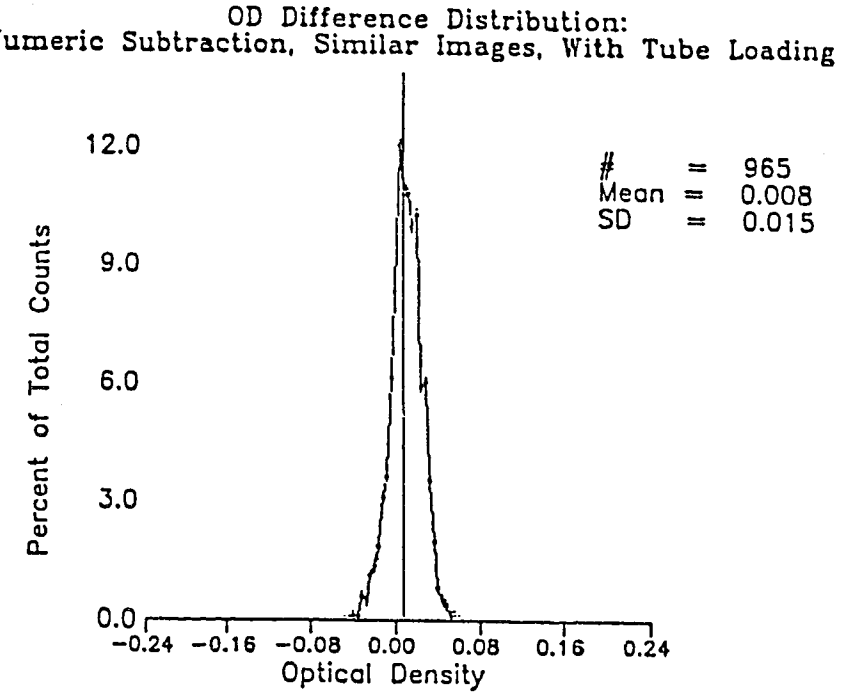

Fig. 28 Tube heating has no significant affect on field reproducibility.

Analysis of variance on the data in Table 9 gives the following results:

Table 10 Analysis of Variance for 4 x 4 Field Matrix

Data Grouping for Source of Variance	Corrected Sums of Squares	Degrees of Freedom	Variance	Ratio
Within Group	2.74×10^{-1}	1249	2.20×10^{-4}	-
Between Group	1.43×10^{-1}	15	9.54×10^{-3}	43.5
Total	4.17×10^{-1}	1264		-

The ratio in the last column of Table 10 is the ratio of the between group variance with that of the within group variance. The ratios of variances follows an F distribution, in this case with 15 and 1249 degrees of freedom. The null hypothesis is that the between group

variance is not significantly larger than the within group variance. $F_{15,\infty}(1\%)$ is 2.04. Therefore, the probability of obtaining such divergent variances where the null hypothesis is true is << 1%. One may safely conclude that the standard deviations over the various portions of the film are not from the same population, and thus that the field varies in a non-random way from portion to portion. The appropriate analysis then is to treat each of the areas in the 4x4 matrix separately, ie as a separate data pool. One source of error is the variation between the means of the different cells. This appears to be a systematic error. Indeed, it would be odd to suppose it a statistical error since the boundaries of the cells are set arbitrarily and thus there is no reason to suspect statistical variation between cells.

To estimate this error, then, we take the difference between the largest and the smallest of the means of the cells. The smallest mean belongs to cell (x=1,y=1) and is $-5.51\text{x}10^{-4}$. The largest is from cell (3,4) and is $-3.53\text{x}10^{-2}$. Our estimate of the systematic error will then yield the value:

$$\left|-5.51\text{x}10^{-4} - -3.53\text{x}10^{-2}\right| = 3.47\text{x}10^{-2}.$$

The other component of the error in this data is the statistical component. It is given in Table 10 and in the form of the within group variance. In fact, it is simply the within group standard deviation which is:

(2.4.1) $$\sqrt{2.195\text{x}10^{-4}} = 1.48\text{x}10^{-2}\ \text{OD}$$

A signal that is within two standard deviations of the base noise level is more than 2% likely to be missed. This means that a better estimate of the statistical error is two standard deviations or 2.96×10^{-2} OD. Combining this with the systematic error gives one an overall estimate of the error of:

(2.4.2) $\quad 2.96 \times 10^{-2} + 3.47 \times 10^{-2} = 6.43 \times 10^{-2}$ OD $\simeq$ 0.06 OD.

This does not bode well in light of the earlier estimate of the optical density corresponding to 40 mg/cm^2 Ca concentration (0.09 OD), since three subtractions must be made, thus tripling the systematic error and increasing the statistical error by $\sqrt{3}$.

In order to have any hope of being able to detect 40 mg/cm^2 of calcification in an SPN, then, it is essential to reduce the error. The source of the statistical error can not be readily identified. The systematic error on the other hand may be more readily identified.

2.4.3 Sources of Error

There are only three ways in which error may be introduced in numeric subtraction of similar films. One is that the field may, and likely does, change between exposures. This would be expected to introduce statistical errors since the only difference between such films would be expected to be the random variation in the photon flux and absorption in the emulsion.

A second source of error is the alignment of the films for subtraction. This would be expected to produce a systematic error, as the effect would be constant across the entire film. The third source of error would be introduced by the scanning densitometer. This could take two forms. Statistical error might be introduced by electronic noise in the circuitry and systematic errors could be caused by zero level drifts or the overlaying of the 60 Hz line voltage onto the signal.

To test the importance of these errors, one of the films from the last experiment was used. It was scanned on the scanning densitometer, removed, realigned, and scanned again. It was then scanned a third time without repositioning. By numeric subtraction of the first two scans we can measure alignment errors. Comparing this to the subtraction of similar films in the previous experiment will also measure the errors due to different exposures. A numeric subtraction of the film from itself without repositioning on the densitometer will measure the densitometer error.

Figures 29 and 30 show the field after numeric subtraction of identical films with realignment on the scanning densitometer. In Fig 29 the field is shown with the alignment artifacts still in. Some waviness can be seen in the image, much as with the similar film subtraction in Fig 27. Again some edge effects are apparent. Fig 30 shows the field after the alignment artifacts and most of the edge artifacts have been removed. Note that the range of ODs is somewhat less than for the similar films subtraction of Fig 27. The most notable feature of the graph in Fig 30 however is the apparent change in the base level of the z (OD) coordinate upon which the random fluctuations

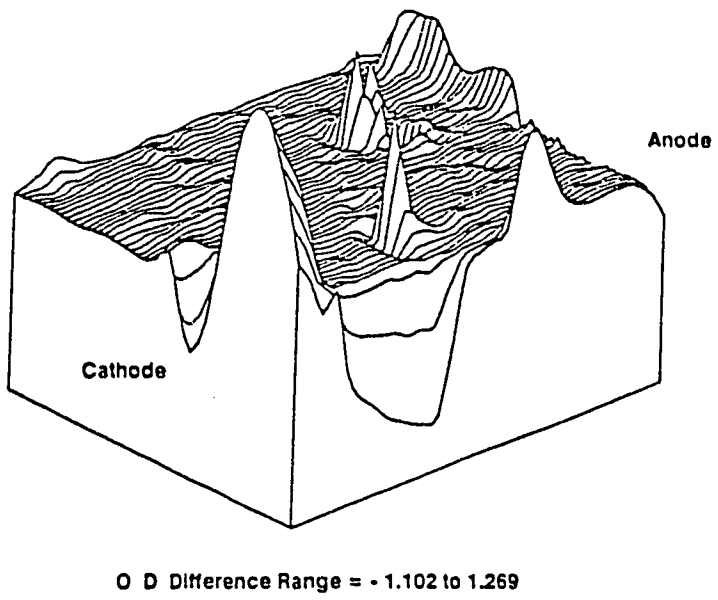

Fig. 29 Even if an image was subtracted from itself (subtraction of identical images) artifacts were produced.

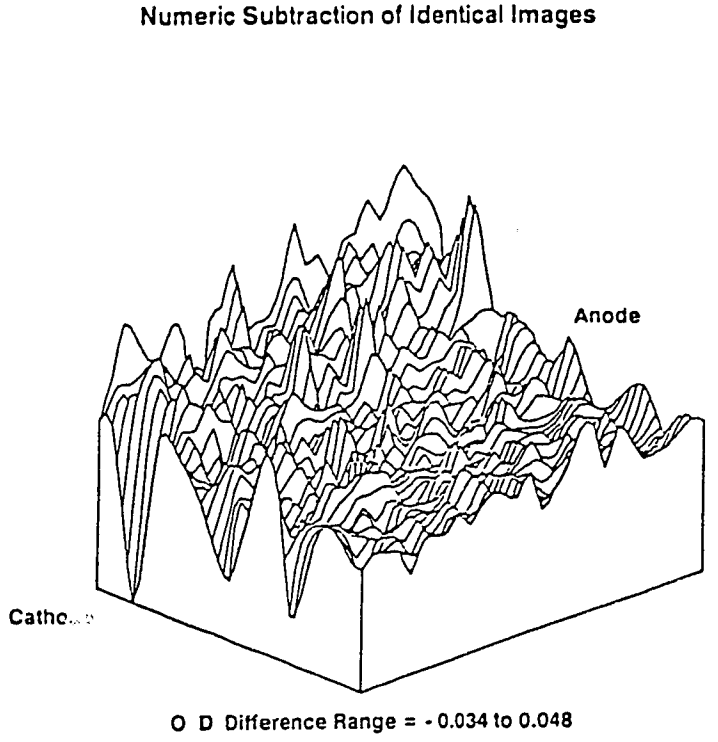

Fig. 30 Subtraction of identical films left residual inhomogeneity superposed on a gradient.

exist. This evidence suggests the importance of the alignment error.

Fig 31 is the frequency distribution of OD for the identical subtraction. Comparison with Fig 28 shows that while the standard deviation for the identical image case is slightly larger (of the order of 0.003 OD), the displacement of the mean from the expected value of 0 is reduced by $|2.23 \times 10^{-2} - 0.90 \times 10^{-2}| = 0.014$ OD.

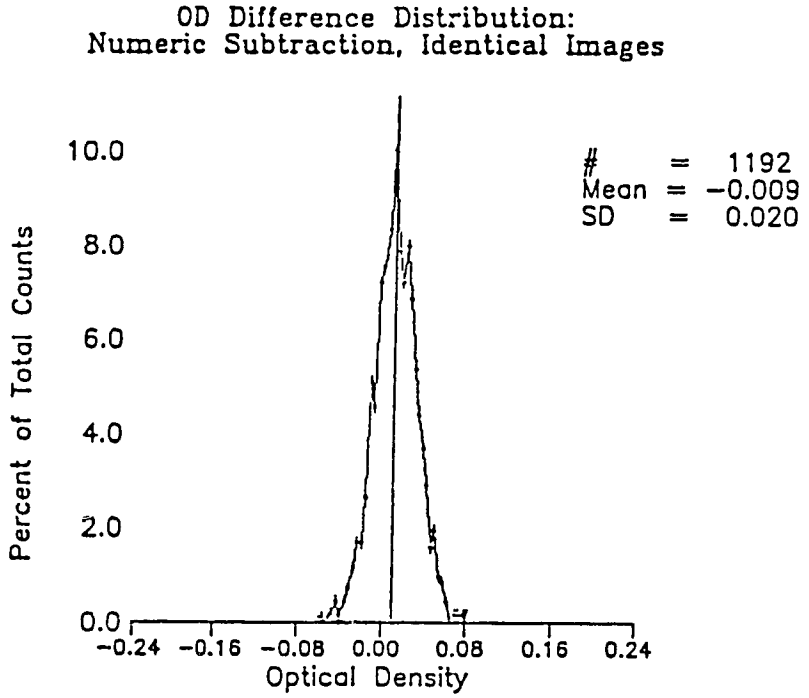

Fig. 31 There is clearly a significant error produced in the subtraction of identical images.

This can be explained entirely by the fact that the AEC device may vary the radiation exposure by as much as 10% between exposures. The maximum optical density of a normal film may be 2.0 OD. Thus, a 0.014 OD difference between two films constitutes a fluctuation in OD of less than 1%, and is well within acceptable levels. Although this may change the mean of the frequency distribution, it would change it in a uniform manner over the film. A change in the intercept of a calibration line created from the ring phantom might therefore be

expected, however a change in the slope would not, and thus the use of a calibration phantom in the image would circumvent this effect.

Apparently then, the random variation in x-ray photon flux between exposures does not lead to an error which is of any significance for the purpose of calcium quantitation. Indeed, such an error was undetected by the experiment above.

The second source of error which is of interest is the misalignment of the images for subtraction. To observe its effects we compare the subtraction of identical films: with realignment and without realignment.

Fig 32 shows the result of the subtraction of identical films without repositioning before alignment and edge artifacts have been removed. In principle, the alignment markers and edges should no longer be visible since the scanning densitometer should always produce the same z for a given (x,y) coordinate. Such is evidently not the case. Although the field appears smoother than that of the realigned case, there is still some significant variation visible which cannot be attributed to alignment markers or edges.

Fig 33 shows the alignment and edge artifacts removed. Along with random fluctuations in the field one can observe a general tendency towards decreased OD in the x direction. Thus, alignment of films for subtraction does not appear to be the only source of image misalignment. However, a decrease in the OD ranges between Figs 29 and 33 demonstrates that positioning of films likely leads to some of the error.

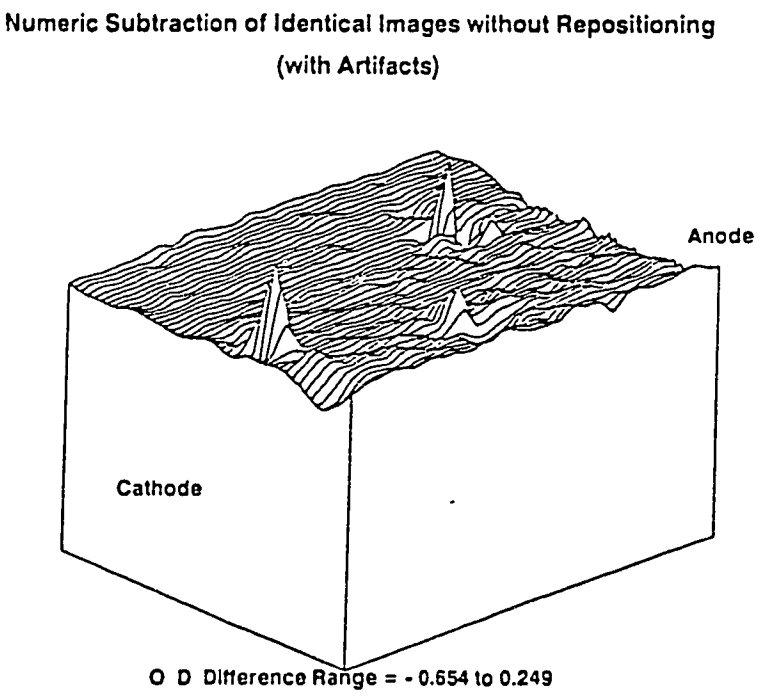

Fig. 32 When positioning error is eliminated (the film is not repositioned between scans) the field after subtraction is very uniform. There are still artifacts however.

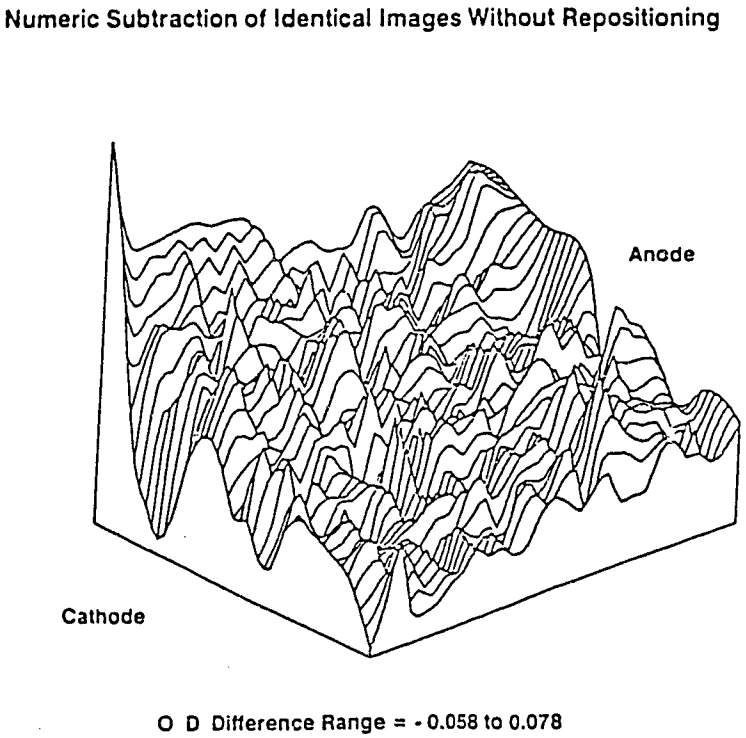

Fig. 33 A magnified view of the field show a perceptible gradient.

This is much more clearly identified by comparing the frequency distributions of the two types of images. Fig 34 shows this distribution for the non-realigned case. A comparison to Fig 31 (realigned films) shows that the mean shifts only by a small amount (0.004 OD) but that there is a large (1.19×10^{-2} OD) decrease in the standard deviation. Film misalignment is therefore one of the primary contributors to the error associated with subtraction of images.

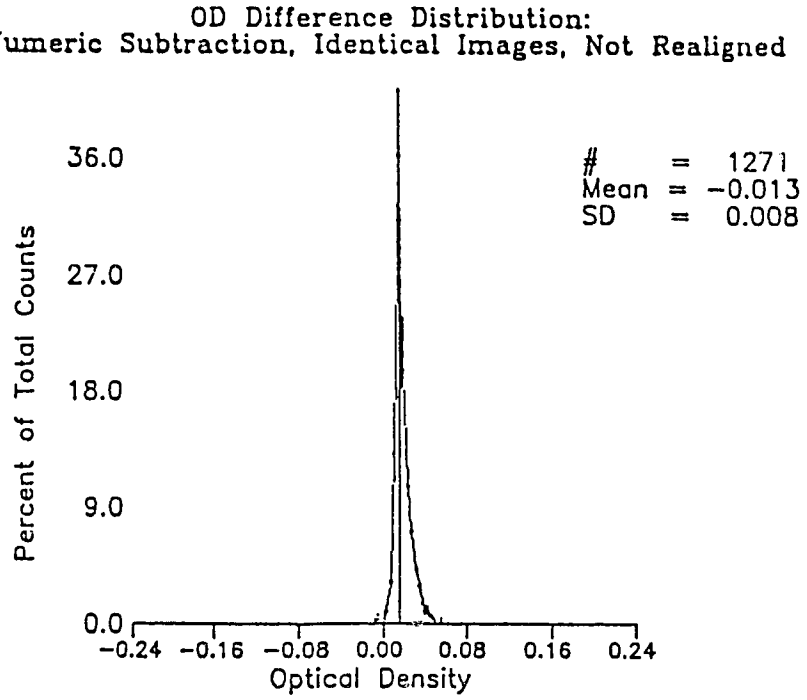

Fig. 34 For non-repositioned subtraction the error is substantially reduced, however, there are apparently other sources as well.

Another source of error is evident from inspection of Fig 34 which shows a frequency distribution of OD differences for the non-repositioned subtraction. The subtracted fields were identical in every way for this subtraction. One would therefore expect a mean and standard deviation of zero, that is, all optical density differences should be zero.

Clearly, this is not the case in Fig 34. The non-zero mean is probably due to an offset in the zero level between the two sets of z or OD measurements which would lead to a constant difference between these sets of measurements. The non-zero standard deviation is probably due to random electric noise in the signal voltages. It is beyond the scope of this work to investigate the source of these errors. The significant point is that the shift in the mean affects the entire image uniformly and thus the standard deviation represents the only machine error. This error is $2 \times 8.0 \times 10^{-3} = 0.016$ OD and is approximately consistent with the 0.02 OD error that is typical for densitometers.

In summary, then, there are two significant contributions to the error for numeric subtraction. One is the alignment error and the second is the densitometer error. The result is a systematic error in which the mean difference in a sub-area of the image varies monotonically across the image. There is also a statistical error in which individual differences fluctuate randomly about the mean within a given sub-area. The net result is that if one wishes to be 99% confident that a nodule density corresponds to more than 40 mg/ml Ca concentration, it must have the 40mg/ml OD plus the error of 6.43×10^{-2} OD. If, in fact, the OD corresponding to 40 mg/ml is less than 6.43×10^{-2} OD then we conclude that the entire process lacks the sensitivity to distinguish malignancy in SPNs.

2.4.4 Film Subtraction With the Scanning Densitometer

Film subtraction, as was used with the manual densitometer above, might better eliminate field non-uniformity. This is because the films are aligned directly with one another, rather than with external reference markers as was the case for numeric subtraction.

To test this possibility two more films were made by x-ray exposure. The objects imaged in both cases were two 6 cm water blocks. Two 2 mm diameter wires were placed on the blocks, adjacent to and parallel with two orthogonal edges of the film. These wires were used as alignment references. Their length and well defined edges allowed better alignment than had the lead numbers.

From the first of these two films a negative was obtained. Exposure A and its own negative were subtracted using film subtraction for one image, while exposure B and the negative of exposure A were subtracted for a second. These, then, were film subtractions of identical and similar images respectively.

Fig 35 and 36 show the 3-D mesh graphs for the similar and identical subtractions respectively. The alignment and edge artifacts have already been removed from both images. There is a huge trough clearly evident in the middle of both subtraction images. Optical density ranges are nearly identical for the two subtractions. The frequency distributions for these two images are shown in Fig 37 and 38. These bear little resemblance to a Gaussian distribution, or to the distributions obtained by numeric subtraction. Both distributions have standard deviations of approximately 0.035 OD.

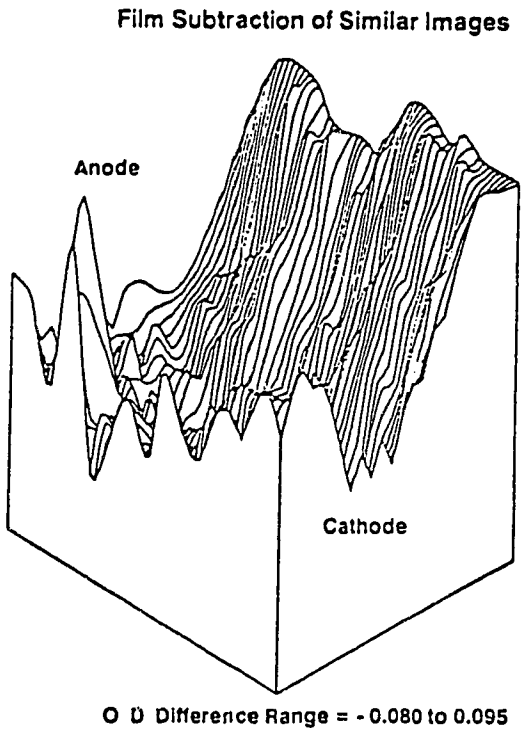

Fig. 35 Film subtraction produces a trough in the field.

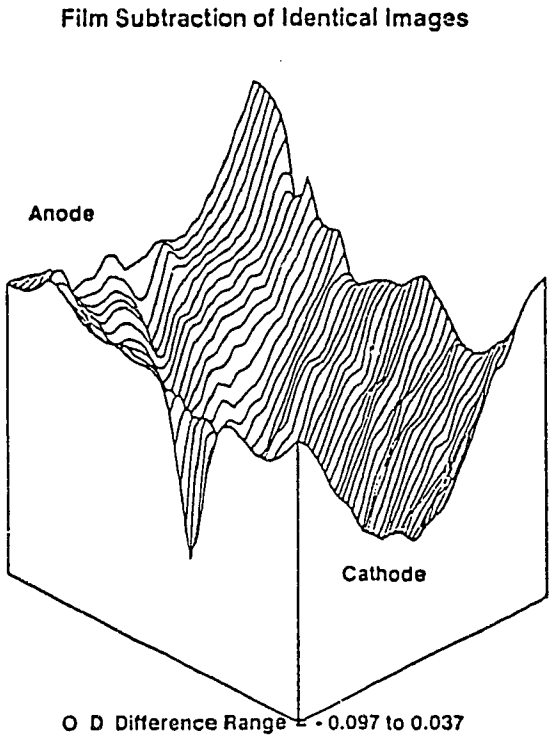

Fig. 36 There is also a trough created in film subtraction of identical images.

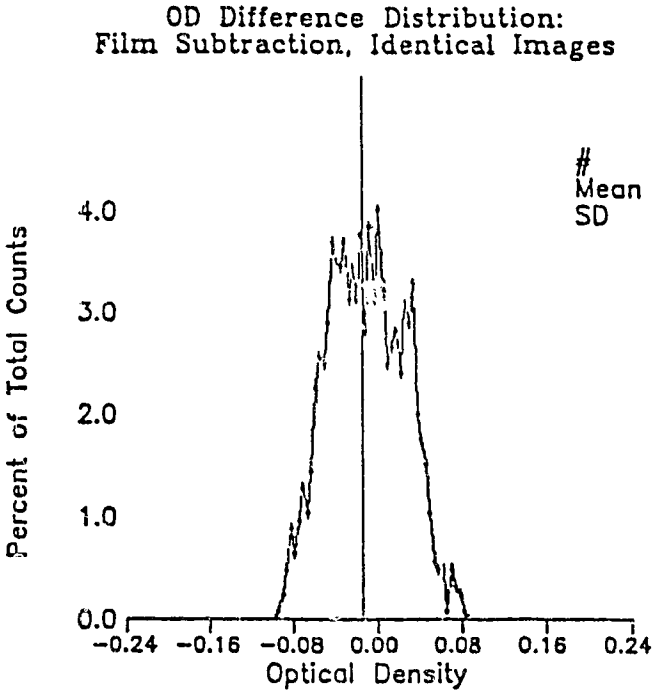

Fig. 37 The frequency distribution for the film subtracted field shows very large errors after subtraction.

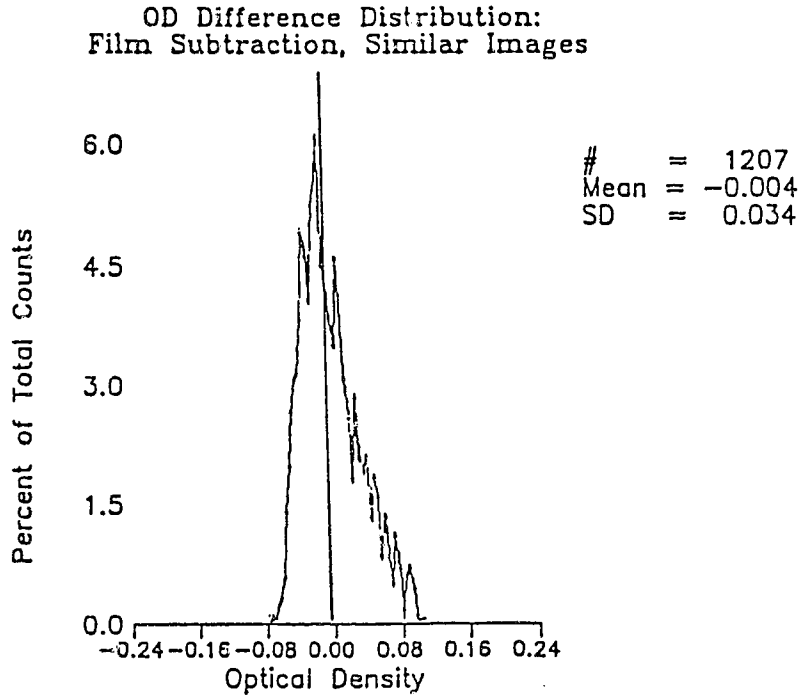

Fig. 38 Again, the frequency distribution shows a large error.

The shape of the mesh graphs (Fig 35 & 36) suggest that the center of the image is in some way subtracted differently from the edge. Also, the trough seems to be shifted between subtractions; it is closer to the anode and the front of the image for the similar films subtraction. The most probable explanation for this would be that the visible light used to expose the mask and the subtraction films does not have a constant intensity over the entire film.

Visible light non-uniformity is caused simply by the fact that the lamp approximates a point source. The light from such a source has a higher intensity at the center of the film, since intensity varies as r^{-2}.

To determine whether the "point source" approximation was causing the trough during subtraction a simple experiment was devised. Two subtraction images were made in which the center of the point source (lamp) was aligned with the center of the films. A third was made with the point of maximum illumination shifted from the center of the films by approximately 2 cm along each axis. A plumb line was used to align the images and the point source.

Figures 39 - 41 show the resultant fields from such a subtraction. Although there is little visible difference between the fields, a program was written to detect the minima of the troughs for each case. In order to prevent a false reading due to noise, a nine point linear smoothing algorithm was used in the program. The results are shown in Table 11.

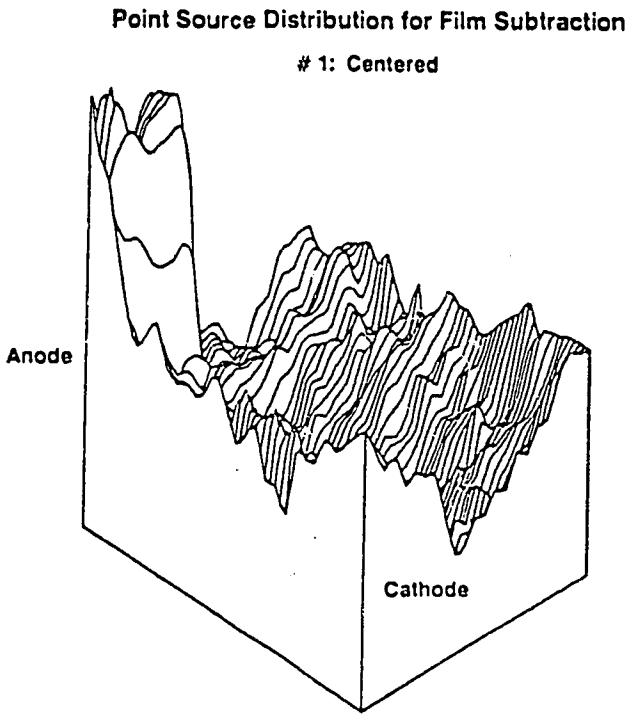

Fig. 39 The first centered subtraction field.

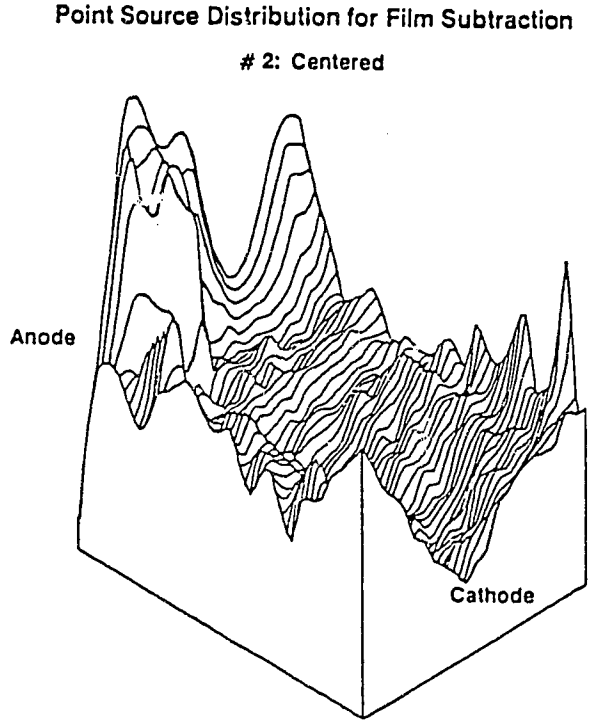

Fig. 40 The second centered subtraction field.

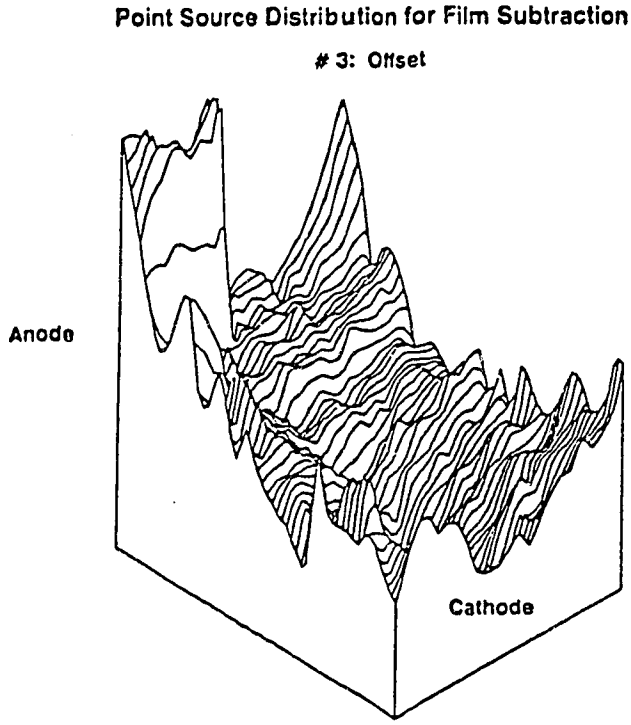

Fig. 41 The offset film subtraction field looks like the other two, but closer analysis reveals an offset in the minimum.

Table 11 Positions of Minima For Film Subtraction

Alignment	Distance from X Edge	Distance from Y Edge
centered	12 cm	10 cm
centered	12.5 cm	10 cm
non-centered	13.5 cm	8 cm

Because only data at every half centimeter in x and every centimeter in y were used, the first two readings are in fact from adjacent points. Although optimally there should be no shift between the minima coordinates of the first two subtractions, a shift to an adjacent point 0.5 cm away is not unreasonable considering the error induced by noise even after the smoothing. The shift between the first

and third cases of 1.5 cm in the x direction and 2.0 cm in the y is close to the 2 cm shift expected in each.

Thus, it seems that the point-source-like nature of the lamp does cause the trough effect in film subtraction. To correct this problem a plane source of visible light would be necessary. The point source was 128 ± 1 cm from the center of the films. For our 30 x 24 cm film the edge of the film was therefore 129.4 cm from the source. Since intensity falls off as r^2 the maximum variation of intensity over the film would be:

(2.4.3) $$100 \times (1 - [128/129.4]2) = 2\%$$

Figures 37 and 38 show that this corresponds to an optical density difference (range) of 0.174. One can use these numbers to calculate the height at which we would get illumination uniformity to within 0.02 OD as follows:

(2.4.4) $$\frac{0.02\ OD}{1.74\ OD} = \frac{n\ \%}{2\ \%} \quad \rightarrow \quad n = 0.023\%$$

Thus

(2.4.5) $$99.977\% = \frac{r^2}{r^2 + 12^2 + 15^2} \rightarrow$$

$$r = \sqrt{(99.977/0.023) \times (12^2 + 15^2)} = 400 \text{ cm}$$

This distance of 4 meters from lamp to film is larger than would be readily available in most clinical settings. A plane source would be ideal, but these are usually approximated by simply placing a diffusing medium over a light source and a homogeneity of 0.023% might not be readily achievable.

2.4.5 Calibration Curves for Numeric Subtraction

The graph in Figure 23 was used to provide an estimate of the optical density corresponding to the critical 40 mg/ml concentration of calcium. This graph was obtained by measuring a film subtraction image of the ring phantom. In light of the preceding data, a large error may have been present in the estimated value of 0.09 OD. In fact, a subtraction of empty fields yielded an optical density range of 0.174 OD.

Although numeric subtraction also has an error associated with it (0.064 OD), it is substantially less than that introduced by film subtraction. Furthermore, almost half of this error is statistical in origin. Thus, by taking many measurements, this source of error can be minimized. It is likely, then, that numeric subtraction would give a better estimate of the optical density corresponding to 40 mg/ml.

In order to obtain this estimate, the ring phantom image and empty field mask used for the graph in Fig 23 were used again. These images were scanned using the scanning densitometer and their optical densities subtracted. For this purpose, 1 mm spacing was used in the y direction and a 24 cm x 5.6 cm area through the center of the phantom was scanned.

The resultant image is shown in Fig 42. Data for a calibration curve were taken from this image. One of the lines from the center of the image (y = constant) was analyzed to obtain this data. The data from the rings were selected manually at 1 mm intervals in the x direction along this line. Data from within 1 mm of the walls separating the rings were ignored to avoid partial area effects.

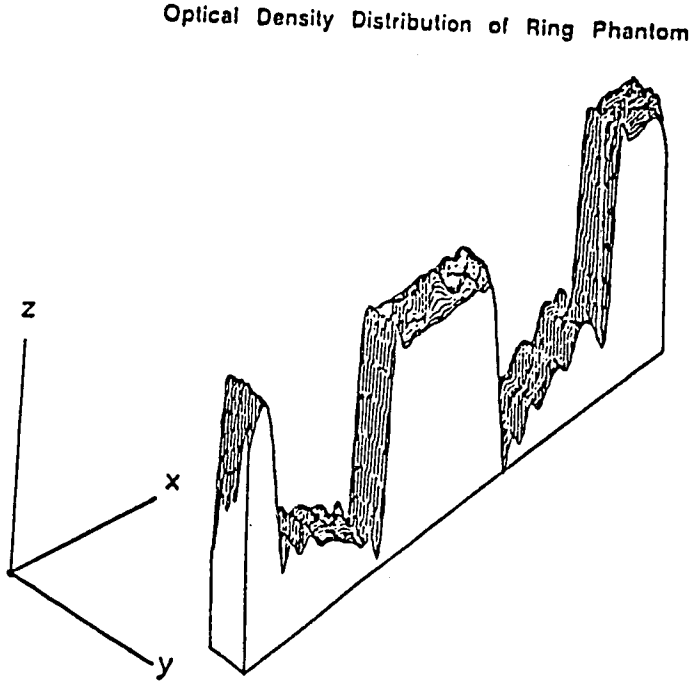

Fig. 42 A section from an image of the ring phantom was scanned and subtracted.

An average of five data points was used as data for each ring. The average OD values for these five points were plotted versus Ca concentration to obtain calibration curves (see Fig 43). Curves for both portions of the rings left and right of the center of the phantom were obtained in order to provide more data sampling. Performing an analysis similar to that for the film subtraction curves in Fig 23 yields the following results (Table 12):

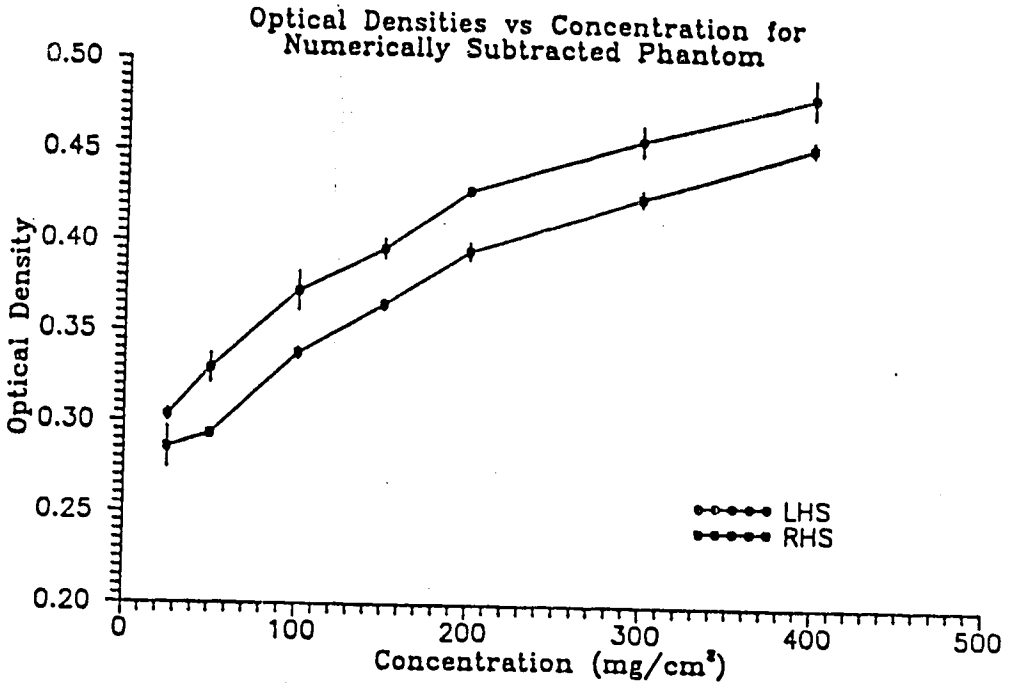

Fig. 43 Two calibration curves were obtained from the numerically subtracted ring phantom.

Table 12 Taylor Expansion Coefficients For Numerically Subtracted Ring Phantom

Ca Conc. $=x$ (mg/cm^2)	Mean OD Diff. $f(x)$	$\Delta(f)$ ($\times 10^{-2}$)	$\frac{\Delta(f)}{\Delta x}$ ($\times 10^{-4}$)	$\Delta\left[\frac{\Delta(f)}{\Delta x}\right]$ ($\times 10^{-4}$)	$\frac{\Delta^2(f)}{(\Delta x)^2}$ ($\times 10^{-6}$)
25	-0.211	-	-	-	-
50	-0.193	1.8	7.2	-	-
100	-0.149	4.4	8.8	1.6	2.1
150	-0.122	2.7	5.4	-3.4	-3.4
200	-0.089	3.3	6.6	1.2	1.2
300	-0.059	3.0	3.0	-3.6	-2.4
400	-0.031	2.8	2.8	-0.2	-0.1

The values for f(x) are the average optical density difference (ODD) readings over both sides of the phantom (RHS & LHS). Using these coefficients in the same way as for the film subtraction case yields:

(2.4.6) ODD(0 mg/ml) = -0.223

ODD(40 mg/ml) = -0.200

Thus, our best estimate shows that 40 mg/ml corresponds to an optical density difference of 0.023 OD. This result is discouraging since densitometers found in clinical settings usually have errors of 0.02 OD. Further, it would appear very unlikely that even after only one subtraction process one could reduce field inhomogeneity to less than 0.02 OD. Since it has already been stated that three subtractions would be necessary for a final image, and since the field nonuniformities will add, it appears impossible to measure the 0.023 ODD for 40 mg/ml Ca.

2.5 Thick Target Bremsstrahlung Theory

There is yet another method in which the x-ray field distribution might be eliminated. Since the distribution is created almost entirely by the bremsstrahlung process a suitable theory of this process could allow us to predict the field distribution. Corrections could then be applied to the measured ODs in order to create a flat field.

A suitable theory for thick target bremsstrahlung does not exist, although theories for the thin target case have met with good success[17]. A discussion and analysis of a semi-classical approach to this problem will illustrate some of the difficulties.

To begin this derivation we borrow from Jackson[18]. The development of thin target bremsstrahlung cross sections in chapter 15 of Jackson

is self explanatory, and no further elaboration is required. For the present development we begin with:

(2.5.1)

$$\frac{d\chi'(\omega')}{d\Omega} = \frac{16}{3}\frac{Z^2e^2}{c}\frac{(e^2)^2}{(m_0c^2)^2}\frac{c^2}{v^2}\ln\left[\frac{\lambda\gamma m_0 v^2}{\hbar\omega'}\right]\left[\frac{3}{16\pi}(1+\cos^2\theta')\right]$$

where:

χ = Bremsstrahlung cross section (area·energy/frequency)

ω = angular frequency of bremsstrahlung radiation

Ω = the solid angle variable

Z = the atomic number of the target (74 for tungsten)

e = the electronic charge

c = the speed of light in a vacuum

m_0 = the rest mass of the electron

v = the speed of the electron

λ = an error factor introduced by Jackson in derivation

γ = the relativistic factor $(1 - v^2/c^2)^{-1/2}$

$\hbar$ = Planck's constant

θ = the angle between the direction of v and the observer.

and ' denotes in the electron's rest frame.

Implicit in the derivation of this formula were various assumptions. They are:

1) The angle of deflection of the electron during the radiation process is very small.

2) Only radiative collisions occur and those occur only once for each electron.

3) The nuclear fields are fixed and the atomic electron field is negligible.

Assumptions 1) and 2) are essentially a statement that this is a thin target cross section. Assumption 3) really contains two statements, that the mass of the electron is much less than the mass of a target nucleus, which is certainly true in the imaging domain, and that the atomic electrons do not screen the nuclear field. For tungsten, screening is not significant for electrons with energy $\geq$ 2 keV.

First, for simplicity, let:

$$A = \frac{1}{\pi}\frac{Z^2e^2}{c}\left[\frac{e^2}{m_0c^2}\right]^2 \cdot \frac{c^2}{v^2} \quad \text{and} \tag{2.5.2}$$

$$a = \frac{\lambda\gamma m_0 v^2}{\hbar} \tag{2.5.3}$$

Then one can use the Lorentz transformations to obtain[19]:

$$\omega' = \omega\gamma(1-\beta\cos\theta) \quad \text{and} \tag{2.5.4}$$

$$\tan\theta' = \sin\theta/[\gamma(\cos\theta-\beta)] \tag{2.5.5}$$

where the relativistic factor $\beta = v/c$.

Now from (2.5.5):

$$1+\cos^2\theta' = 1 + \frac{1}{1 + \tan^2\theta'} = \left[\frac{\sin^2\theta + 2\gamma^2(\cos\theta - \beta)^2}{\sin^2\theta + \gamma^2(\cos\theta - \beta)^2}\right] \tag{2.5.6}$$

Substituting (2.5.2), (2.5.3), (2.5.4), and (2.5.6) into (2.5.1) gives:

$$\frac{d\chi(\omega)}{d\Omega} = A \ln\left[\frac{a}{\omega(1 - \beta\cos\theta)}\right]\left[\frac{\sin^2\theta + 2\gamma^2(\cos\theta - \beta)^2}{\sin^2\theta + \gamma^2(\cos\theta - \beta)^2}\right] \tag{2.5.7}$$

Again, we may simplify by letting:

$$(2.5.8) \qquad B(\theta) = \left[\frac{\sin^2\theta + 2\gamma^2(\cos\theta - \beta)^2}{\sin^2\theta + \gamma^2(\cos\theta - \beta)^2} \right] \text{ and}$$

$$(2.5.9) \qquad b(\theta) = \frac{a}{(1 - \beta\cos\theta)}$$

This simplifies (2.5.7) to:

$$(2.5.10) \qquad d\chi(\omega)/d\Omega = A \cdot \ln(b(\theta)/\omega) \cdot B(\theta).$$

$d\chi(\omega)/d\Omega$ is a measure of the likelihood of a unit amount of energy released in photons of frequency ω into a unit solid angle in direction θ, since the cross-sectional area of an interaction is related to its probability of occurrence. This can be converted into a measure of the energy released into a unit solid angle in direction θ as the particle travels a distance dx by the following relation:

$$(2.5.11) \qquad \frac{d^2E_{rad}(\omega)}{d\Omega \cdot dx} = \rho_z \cdot \frac{d\chi(\omega)}{d\Omega}$$

where ρ_z is the proton density of the target material.
This can further be converted to the number of photons of frequency ω in a unit solid angle about θ by:

$$(2.5.12) \qquad \frac{d^2N(\omega)}{dx \cdot d\Omega} = \rho_z \cdot \frac{d\chi(\omega)}{d\Omega} \cdot \frac{1}{h\omega\gamma(1-\beta\cos\theta)}$$

where the $\gamma(1-\beta\cos\theta)$ factor arises from the transformation from the electron's rest frame.

Earlier the assertion was made that the bremsstrahlung energy spectrum was relatively independent of the emission angle. We are now in a position to test this assertion. The spectrum will remain

unchanged if, for any two frequencies ω_1 and ω_2, the ratio of the number of photons emitted with these frequencies is independent of angle. Thus we examine the ratio:

$$(2.5.13) \qquad \frac{d^2N(\omega_1)}{d^2N(\omega_2)} = \frac{(1/\omega_1)[\ln(b(\theta)) - \ln(\omega_1)]}{(1/\omega_2)[\ln(b(\theta)) - \ln(\omega_2)]}$$

Contrary to our previous assumption, there is some θ dependence in this spectrum. However, the variation is as $\ln(b(\theta))$, which should change slowly. For our geometry the film center is at $\theta_1=\pi/2$ while the corner is at angle:

$$(2.5.14) \qquad \theta_2 = \pi/2 + \arctan\left[\frac{\sqrt{12^2 + 15^2}}{70}\right] \approx \pi/2 + 0.27$$

since the edges of the film are 15cm and 12cm from the center and the source to detector distance is about 70cm. For these two angles b is:

$$(2.5.15) \qquad b_1 = b(\theta_1) = a \quad \text{and}$$

$$(2.5.16) \qquad b_2 = b(\theta_2) = a/(1 - 0.27\cdot\beta)$$

Thus, the difference in the flux between these two angles would be:

$$(2.5.17) \qquad \frac{dN(\omega_1,\theta_1)}{dN(\omega_2,\theta_1)} - \frac{dN(\omega_1,\theta_2)}{dN(\omega_2,\theta_2)} =$$

$$\frac{\omega_2}{\omega_1}\left[\frac{\ln(a/\omega_1)}{\ln(a/\omega_2)} - \frac{\ln[a/\omega_1(1-0.27\beta)]}{\ln[a/\omega_2(1-0.27\beta)]}\right]$$

$$= \frac{\omega_2}{\omega_1}\left[\frac{\ln(a/\omega_1)}{\ln(a/\omega_2)} - \frac{\ln(a/\omega_1) + \ln(1 - 0.27\beta)}{\ln(a/\omega_2) + \ln(1 - 0.27\beta)}\right]$$

Over the diagnostic energy range this difference is practically 0. For instance, for 50 and 100 keV photons from a 100 keV electron beam the difference in the photon ratios from corner to center of film is only 0.05. This five percent fluctuation over the film means that the assumption that the spectrum is invariant is a good approximation.

Another interesting question can be answered at this point: what portion of the total photon flux is emitted into the unit solid angle about the center of the film ($\theta = \pi/2$)? Since the energy distribution is approximately angle independent, this is equivalent to asking what portion of photons with frequency ω_1 are emitted into this solid angle. The angular dependence in (2.5.12) makes this quantity difficult to calculate. However a similar expression for the number of photons released into a unit solid angle could be obtained in the electron's rest frame by using the cross section (2.5.1). Since the number of photons emitted must be a Lorentz invariant (the number of objects observed cannot change with inertial frames) this will yield the flux in the target rest frame.

Although the number of photons emitted is Lorentz invariant, the angle at which they are emitted is not; it transforms according to:

$$(2.5.18) \qquad \cos\theta' = \left[\frac{\cos\theta - \beta}{1 - \beta\cos\theta} \right]$$

Thus for $\theta = \pi/2$ we have $\theta' = \arccos(-\beta)$. The total number of photons emitted at frequency ω is given by:

$$(2.5.19)\quad \frac{dN(\omega')}{dx'} = \frac{\rho_z A}{\hbar\omega'} \cdot \ln\left[\frac{a}{\omega'}\right] \int_{-1}^{1} d\cos\theta' \int_{0}^{2\pi} d\phi' (1+\cos^2\theta')$$

$$= \frac{\rho_z A}{\hbar\omega'} \cdot \ln\left[\frac{a}{\omega'}\right] \frac{16\pi}{3}$$

The portion of this emitted at $\theta = \pi/2$ for 100 keV electrons (β=0.55) will be:

$$(2.5.20)\quad \frac{dN(\pi/2)}{dN_{tot}} = \frac{1+(-\beta)^2}{16\pi/3} \approx \frac{1}{4\pi}$$

A theoretical estimate of the field nonuniformity may now be obtained by comparing this to the field at a corner. This will be $\theta = \pi/2 + 0.27$ as in (2.5.14). The number of photons of frequency ω at the corner relative to the number at $\pi/2$ is:

$$(2.5.21)\quad \frac{dN(\theta=[\pi/2+0.27])}{dN(\theta=\pi/2)} = \frac{1+[(-0.27 - \beta)/(1+0.27\beta)]^2}{1 + \beta^2}$$

$$= 1.16$$

Likewise, at the corners represented by $\theta = \pi/2 - 0.27$ the flux would be less than at the center by ~16%, for a net difference of 32%. This indicates a field that increases monotonically from on end to the other. The data presented earlier, and especially Fig 24, show that this is not evident in practice. This inconsistency is due to the fact that we have been working with a thin target approximation for our theoretical cross section. If we wish to have a theory which properly expresses the experimental situation of the x-ray tube, it will be necessary to develop a thick target theory. It is noteworthy that the above equations are approximate even for the thin target case. A

rigorous treatment of bremsstrahlung would require the use of quantum electrodynamics, and is well beyond the scope of this dissertation.

The approximate nature of this treatment can be seen by calculating the total number of photons of all frequencies emitted into the unit solid angle about θ. The calculation of such a quantity leads to the integral:

$$\int_0^{\omega max} \frac{d\omega}{\omega} \ln[b(\theta)/\omega] \tag{2.5.22}$$

which is singular.

One would like, then, to find a thick target expression equivalent to (2.5.12). One of the primary differences between the two treatments is that in a thick target the electron will lose all of its energy while in the thin target case the energy remains essentially constant.

We wish to integrate (2.5.12) over the path length in order to calculate the entire contribution to the spectrum. To do this, we must first express v, and consequently β and γ as functions of x. In general, v will change due to both radiative and collisional energy losses of the electron with the nuclear fields. However, in the diagnostic energy range (approximately 10 to 100 keV), the losses are predominantly collisional[20], and we will assume that the bremsstrahlung energy loss is negligible. A theory of the collisional energy losses of a particle was developed by Hans Bethe. A modern version of this theory is presented by Seltzer and Berger[21]. They state:

$$\frac{dE}{dx}_{coll} = - \frac{0.153536}{\beta^2} \frac{\rho Z}{A} B(T) \tag{2.5.23}$$

where:

(2.5.24) $$B(T) = B_0(T) + b_0$$

(2.5.25) $$B_0(T) = \ln\left[\frac{1}{2}\left(\frac{T}{m_0c^2}\right)^2\left(\frac{T}{m_0c^2}+2\right)\right] + \left[\frac{T}{m_0c^2}+1\right]^{-2} \times \left[1 + \frac{1}{8}\left(\frac{T}{m_0c^2}\right)^2 - \ln 2\left(\frac{2T}{m_0c^2}+1\right)\right]$$

and:

ρ = the density of the target

A = the atomic mass of the target

b_0 = a dimensionless constant dependent only on the target

T = the kinetic energy of the electron.

This is the form of the expression given by Seltzer and Berger for electron energies $\leq$ 554 keV. $B_0(T)$ depends only on the energy of the electron, not the target material. Analysis of this expression reveals that over the 10 - 100 keV range of electron energies the second (non-logarithmic) term is negligible. Thus we have simply:

(2.5.26) $$\frac{dE}{dx}_{coll} = \frac{-\alpha}{\beta^2}\cdot\ln\left[\frac{e^{b_0}}{2}\left(\frac{T}{m_0c^2}\right)^2\left(\frac{T}{m_0c^2}+2\right)\right]$$

where:

(2.5.27) $$\alpha = 0.153536\cdot\rho\cdot Z/A$$

Now the relativistic energy of a particle is given by:

(2.5.28) $$T = E - m_0c^2 = (\gamma-1)m_0c^2$$

$$\rightarrow \quad (T/m_0c^2)^2 + 1 = 1/(1-\beta^2)$$

(2.5.29) $$\rightarrow \quad \beta^2 = \frac{[(T/m_0c^2)^2 + 2T/m_0c^2]}{[T/m_0c^2 + 1]^2}$$

Letting:

(2.5.30) $$u = T/m_0c^2$$

we obtain the differential equation:

(2.5.31) $$\frac{du}{dx}_{coll} = \frac{du}{dx} = \frac{-\alpha(u+1)^2}{u^2+2u} \ln\left[e^{b_0} \cdot \frac{u^2(u+2)}{2}\right]$$

Restating (2.5.31) as an integral equation yields:

(2.5.32) $$x + c = -\frac{1}{\alpha}\int du\ \frac{u^2+2u}{(u+1)^2} \ln^{-1}\left[e^{b_0}\ \frac{u^2(u+2)}{2}\right]$$

where:

c = the integration constant

$\ln^{-1}(x) = 1/\ln(x)$

This is not an integrable form, but it may be simplified by noting that in the energy range 10 - 100 keV, u is relatively small:

(2.5.33) $u = T/m_0c^2 << 2$ and

(2.5.34) $u^2 << 1$

Thus, (2.5.32) becomes:

(2.5.35) $$x+c = -\frac{2}{\alpha}\int du\ \frac{u}{2u+1} \ln^{-1}[u^2e^b]$$

By letting:

(2.5.36) $$v = ue^{b_0/2} \rightarrow dv = e^{b_0/2}\cdot du$$

equation (2.5.35) becomes:

$$(2.5.37) \qquad x+c = \frac{-1}{\alpha e^{b/2}} \int \frac{dv \quad v}{(2v+e^{b/2})\ln[v]}$$

This integral may be solved only in terms of the well known logarithm-integral:

$$(2.5.38) \qquad li(x) = \int_0^x dt\ \ln^{-1}[t]$$

Through some rather messy integration we may reduce (2.5.38) to:

$$(2.5.39) \quad x+c = \frac{-1}{\alpha e^{b/2}} \left[v(2v+e^{bo/2})li(v) - 2v\int dv \cdot li(v) - \int dv(2v+e^{bo/2})li(v) + 2\int dv \int dv \cdot li(v) \right]$$

No further simplification of (2.5.39) is apparent. The best one might be able to do at this point is to substitute (2.5.39) into (2.5.12) and integrate numerically along x. One would expect limited success however, since the form of (2.5.12) relies strongly on the condition that the electron be deflected through a small angle. While this is a reasonable condition for a single collision, it does not model well the stopping of an electron in the thick target geometry.

Furthermore, even to produce the very limited success obtained here many assumptions were made, each adding a small error to the theoretical result. To proceed further, it would be necessary to introduce even more assumptions. The continuous-slowing-down approximation that $dv/dx \propto v$ is often used. In order to use theoretically calculated corrections for field non-uniformity in the detection of SPNs our error must be very small. In fact, given that 40

mg/ml corresponds to 0.023 OD and the densitometer error is 0.02, our accuracy must be better than $3x10^{-3}$ OD out of approximately 2.0 OD, or 0.2%, which would seem unattainable, in light of the previous discussion.

2.6 Conclusions

This chapter describes attempts to establish a method of absolute calcium quantification in SPNs with the spotfilm device of a fluoroscopic unit. A phantom of circular geometry was developed for this purpose. The use of such a phantom would eliminate error arising from changes in imaging conditions between a reference image of known calcium densities and the SPN to be measured. Preliminary investigation into the optimal imaging parameters (kVp, mAs) led to the discovery of inhomogeneity in the film exposure, or optical density field. As a result, optical density differences over a film were not simply representative of changes in the object imaged.

Three methods were explored to overcome this field non-uniformity. The first was conventional analog film subtraction, which is routinely used in clinical settings. A quasi-theoretical argument was used to demonstrate the validity of this approach. Preliminary investigation showed that most of the field non-uniformity could be eliminated by this method. Some residual non-uniformity remained however. The causes of this remains unknown at this time. An estimate of the required sensitivity was obtained. 40 mg/cm^2 Ca was estimated to correspond to 0.093 OD.

The second method explored was numerical subtraction of films. a scanning densitometer was employed to obtain optical densities from the entire film. Field non-uniformity became apparent with this technique. Similar films (films taken under the same conditions) were subtracted pointwise in an attempt to remove the inhomogeities.

The resultant image had both systematic and statistical errors, combining to produce a total error of 0.064 OD. This was compared to an estimate of the required sensitivity. Due to the addition of errors from the three subtraction processes necessary for quantification, it was shown that the error was too large to permit the 40 mg/cm^2 threshold to be measured. The causes of these errors were investigated. They proved to be from two sources: the misalignment of films and inherent error in the densitometer. Neither of these sources seemed to be correctable in a way reasonably available in a clinical setting.

Further investigation of film subtraction was undertaken to determine if misalignment, which accounted for the majority of the error, could be reduced. Using the scanning densitometer, subtracted films were investigated and shown to have significant OD distributions. This was shown to be due to the non-planar nature of the light source used in exposure of masks and subtracted images. As a result, the previous estimate of 0.093 OD for 40 mg/ml became questionable. A more accurate estimate of 0.023 OD was obtained through numeric subtraction. This was highly discouraging in that most standard densitometers have errors of ± 0.02 OD.

Thus, it was determined that the errors induced by either film or numeric subtraction were too great to allow detection of the critical level of 40 mg/ml in a 1 cm nodule.

A third method of non-uniformity correction was also explored in this chapter: theoretical calculation of the thick target bremsstrahlung distribution and applying resultant corrections to OD measurements. These calculations came to an inauspicious end, but provided insight into the complexity of the physical principles involved in thick target bremsstrahlung and the extent to which we are forced into a heuristic understanding of them.

To conclude, analog radiography as it exists today is severely limited in its ability to quantify calcium in SPNs. Two other modalities will be explored in subsequent chapters: computed tomography, which is becoming widely used for radiological quantification, and digital radiography, which is expected to play an important part in the future of diagnostic radiology.

Chapter 3 : Digital Radiography

3.1 Materials and Methods

As mentioned in the introductory chapter, digital radiography has been successfully applied to quantifying calcium in SPNs. This modality has the potential to provide the great dynamic range of electronic detectors with the simplicity and comparatively low dose of radiography. It might, therefore, provide an adequate alternative to CT as a method of determining the benignancy of SPNs.

Two general types of digital radiography are in use today. One is based on the use of an image intensifier system. In these systems, an x-ray sensitive phosphor, usually cesium iodide, is used as an input phosphor. This phosphor is like a scintillator in that it converts x-ray photons to visible photons. The visible photons are then converted to photoelectrons via the photocathode. The electrons are accelerated through an electrostatic lens to an anode, which is an electron sensitive fluorescent screen (output phosphor) of zinc-cadmium-sulfide. This screen releases light photons where it is excited by the very energetic electrons.

Thus, the x-ray distribution is converted to a distribution of visible light. The acceleration of the electrons, along with the conversion of the x-ray energy into the lower energy visible photons, produces a great gain in photon flux and energy. This is further enhanced by the fact that the image is minified at the output phosphor. The light photons from the output phosphor are fed into a TV video

chain. The video signal is digitized by an analog to digital converter (ADC).

Two problems with image intensifier (II) based systems are veiling glare and scatter. Compton scattered radiation produces a base noise level and in effect decreases the exposure range of the system. It is present in all types of imaging processes, but is of particular significance in II based digital radiography. It can be removed by collimation, but removal of scatter through collimation increases the patient dose.

Veiling glare is the scattering of visible light within the image intensifier and video system. It produces effects much like those of compton scattered radiation, decreasing dynamic range and thus contrast.

Another method of digital radiography is to have an electronic detector array (much like in CT). This would then provide a digital image with each detector corresponding to a pixel. Scan projected digital radiography (SPDR) is limited in that it produces radiographs of significantly lower resolution than analog radiographs. For qualitative investigations this is a severe handicap in detecting and identifying anatomical detail. The resolution of SPDR is limited by the size and packing of the detectors. Only recently has detector packing become sufficient to allow reasonable resolution in SPDR, and only for some specialized applications. As a result these systems are costly and not, as yet, common. There are virtually no radiographic devices employing SPDR currently on the market.

However, SPDR is used for anatomical reference in CT. It is produced by holding the x-ray tube and detectors in one orientation and

then moving the couch (and patient) linearly through the image plane. This produces a series of one dimensional projections from which the two dimensional image is formed.

Image intensifier based digital radiography is currently used in digital subtraction angiography (DSA), where high density contrast agents are injected intravenously to provide contrast for vascular structures. Background structures can obscure the vascular structure, so images with and without the contrast agent are taken, and the digital images are subtracted to produce an image in which the vascular structure is relatively unobscured.

Each of these two types of digital radiography was investigated: II digital radiography (IIDR) with a Siemens Digitron 2 DSA unit and SPDR with two of the CT scanners: the Picker 1200 and the Siemens DRH. Pixel values could not be obtained in SPDR mode from the GE 9800.

For the IIDR system the stepwedges and ring phantom described in chapter 2 were used. A new phantom was built for SPDR work (see Fig 44). This phantom is a 30 mm wide x 195 mm long x 22 mm deep block of lucite with 7 cylindrical cells, 25 mm in diameter x 20 mm deep, drilled into it. The cells are closed over with a 2 mm thick sheet of lucite. A threaded hole was drilled into each of the seven cells and stopped with a screw and a rubber O ring.

The cells in the "cell phantom" were filled with 0, 5, 10, 20, 30, 50, and 75 mg/ml concentrations of $CaCl_2$ in water. This corresponds to a projected concentration of 0, 10, 20, 40, 60, 100, and 150 mg/cm^2 Ca respectively. Two 6 cm thick water filled blocks were used to simulate scatter from the chest walls for both types of DR.

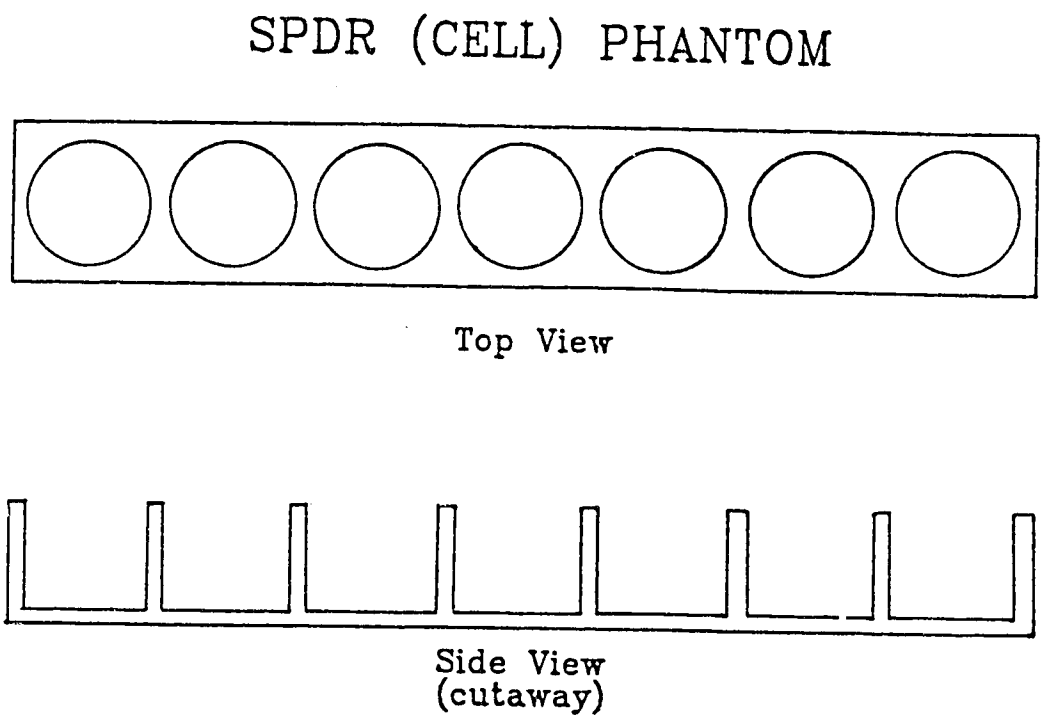

Fig. 44 The cell phantom, designed and built for SPDR experiments.

3.2 Image Intensifier Digital Radiography

For IIDR experiments, the geometry used was similar to that for analog radiography, with the phantom placed atop the two water blocks. Unfortunately, pisel values could not be obtained from the ADC with this particular model, nor were there any systems available in nearby hospitals that could produce such numbers.

This meant that the only advantage of using IIDR was that the alignment error could be reduced by using digital subtraction. However, optical density would still have to be measured from a film with a densitometer, meaning that the minimum error achievable would be 0.01 - 0.02 OD.

Fig 45 shows a comparison of the OD measurements for a subtracted stepwedge using numeric subtraction from analog radiography and a

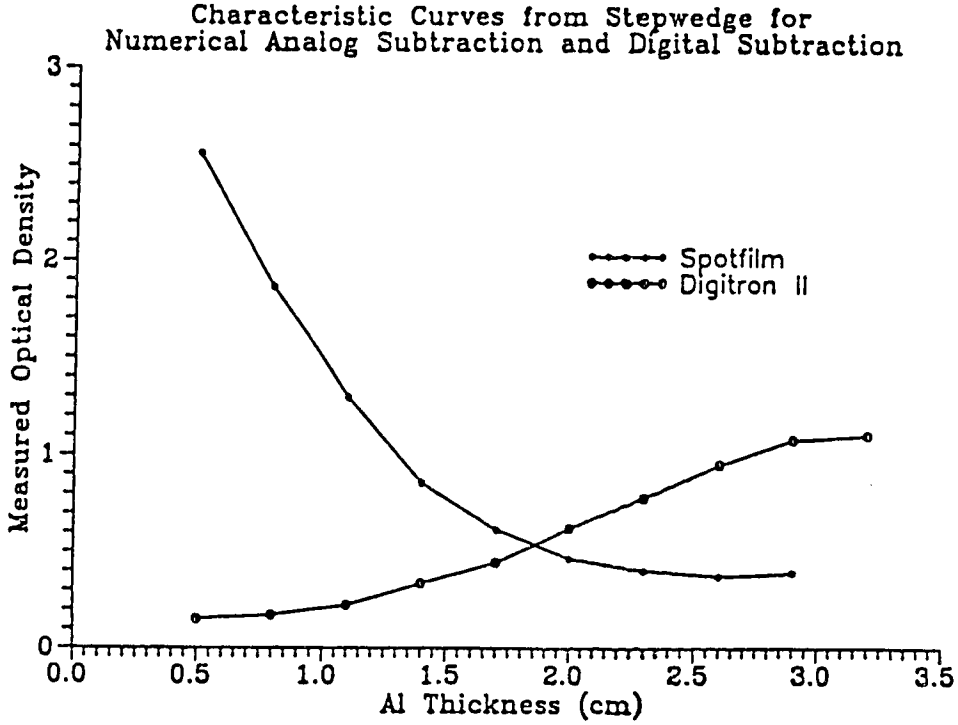

Fig. 45 Subtracted DSA films have poorer contrast characteristics than spotfilms.

digitally subtracted image. The IIDR image was produced on a multiformat camera. The maximum slope for the analog subtraction is -2.33 OD/ml of aluminum. For the digital subtraction it is 0.6 OD/ml of aluminum. This means the analog contrast resolution is nearly four times better. Since the OD range corresponding to 40 mg/ml for analog subtraction was 0.02 OD, one would expect the OD range for digital subtraction to be $\approx$ 0.005.

It might be possible to find a film for the multiformat camera that has better contrast, but the corresponding loss of latitude would detract from the increase in range. Furthermore, the software for our DSA system is limited in its applicability to quantitation. It does not readily allow subtraction of more than two images. Since dual energy subtraction would be necessary for quantification, and uniformity

corrections would be required for both energies, four images must be involved in the subtractions.

Lastly, even if IIDR films provided the same contrast capabilities as analog films, the error would still correspond to 40 mg/ml under ideal circumstances. Residual tissue contributions from dual energy subtraction and patient motion would increase the error significantly.

Stated simply, the strong abilities of digital systems to provide contrast information rely heavily on the pixel values. When further steps are needed to obtain quantitative information, such as transference to film, the ability of the system as a whole will be that of the weakest link in the chain. Although IIDR might be a reasonable alternative to CT for quantification of low levels of light elements, research into this possibility will have to await a system in which the pixel numbers are available directly. Current systems on the market do provide this capability.

3.3 Scan Projected Digital Radiography

3.3.1 The Scanners

Three computed tomography systems were used for this study. System 1 was a GE 9800 (from the University of Alberta), system 2 a Picker 1200 SX (from the University of Alberta), and system 3 a Siemens DRH (from the Grey Nuns'). Each of the three scanners had some design characteristics not found in the other two. For simplicity, the systems

will be referred to by this numbering scheme rather than by manufacturer and model.

System 3 used a pulsed x-ray tube. The pulse width was either 1.5 or 3 msec, depending on the software protocol selected. The main advantages of a pulsed system are decreased patient dose and better control of mechanical and electronic systems during the course of the scan.

Systems 1 and 3 are third generation scanners. This means that the x-ray tube and an arc of detectors are mounted on a rotating assembly. System 2 is a fourth generation scanner, containing a tube rotating inside a fixed circular array of detectors. Systems 2 and 3 differ from 1 in that the former have scintillation detectors while the latter has xenon gas detectors. The differences between these will be discussed later.

Of the three available CT scanners, the GE 9800 did not provide direct access to numerical data from SPDR images. The other two systems were therefore used to evaluate SPDR: the Picker 1200 (system 2) and the Siemens DRH, system 3.

Since SPDR on CT scanners is considered an auxiliary function to tomography, little operator control of parameters is allowed. What little there was varied significantly between the two systems. It was also found that SPDR image production was handled very differently between the two systems.

3.3.2 System 2

Little information is available on the use of commercial CT scanners for SPDR. There was, therefore, no certainty among those familiar with the scanners what sort of information the pixel numbers might contain. Thus, system 2 was first tested for field uniformity. The field was found to be not entirely uniform; pixel values having a gradient diagonally across the field. However, it was possible to use a system software supplied subtraction algorithm to subtract images. This technique provided a uniform field.

Next the linearity of system 2 was tested with the 9 step stepwedge described in chapter 2. The stepwedge was attached to one of the two water blocks which were placed on edge on a platform supported by the couch. The tube to detector array direction was set to horizontal via the system software (see Fig 46).

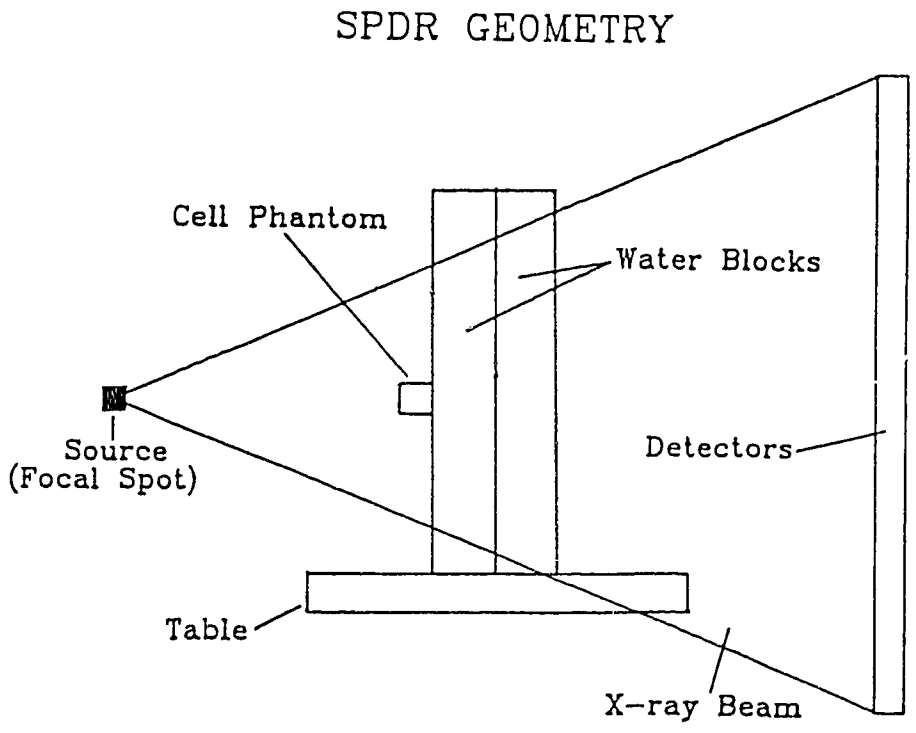

Fig. 46 Geometry for SPDR experiments on a CT scanner.

Regions of interest were defined on each of the steps and means and standard deviations obtained. These are shown in Fig 47. The points represent means and the error bars one standard deviation. Because the standard deviation was so small, the error bars are not visible. It is clear from this graph that there is a general linear relationship between attenuation and detection (mean pixel) number for these images.

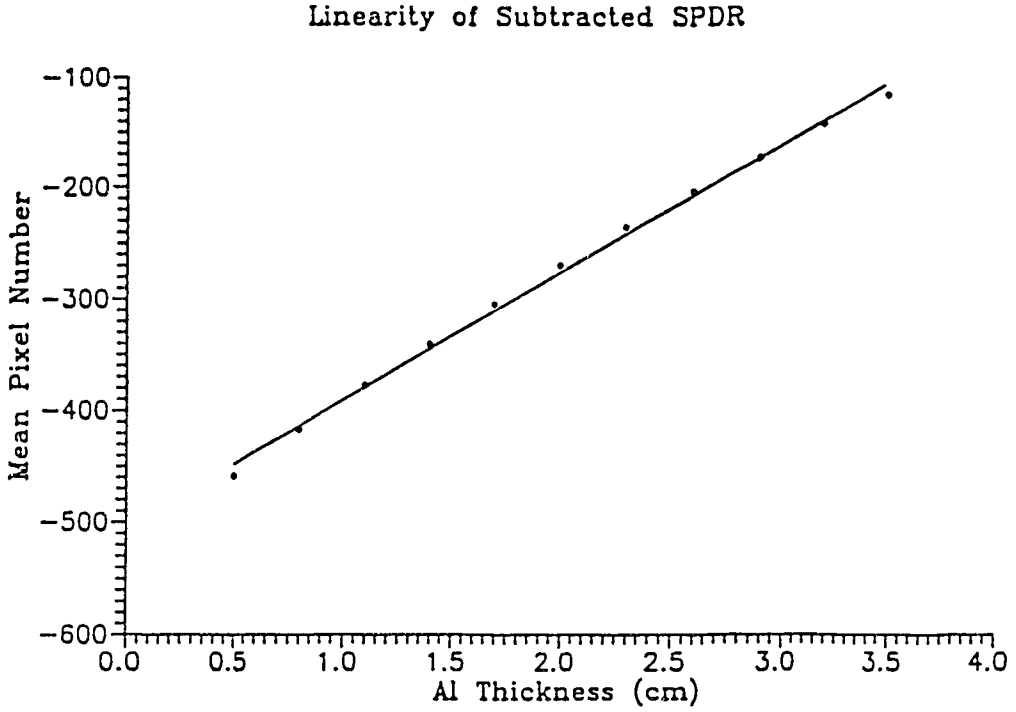

Fig. 47 An image of a stepwedge demonstrates the linearity of a CT scanner for SPDR.

Given this linearity, one can reasonably expect to use SPDR as a quantitative imaging modality. Further experiments on system 2 were carried out to test Ca quantification. The horizontal system geometry was used for all of these experiments. On a platform resting on the couch, two water blocks were placed on edge and the cell phantom taped to the side. Unless it is stated otherwise, experiments for system 2 were performed at the following default parameters: 130 kVp, 20 mA,

cell phantom on the detector side of the water phantoms. Subtraction masks for non-uniformity correction were made with the same geometry with the cell phantom removed. Subtraction was performed on all images.

As mentioned before, the ability to alter parameters on CT scanners for SPDR is limited. Three parameters were varied for this system. kVp and mAs were changed via special service software routines. The affect of beam hardening was examined by placing the cell phantom on the x-ray tube side of the water blocks, in between the water blocks, and on the detector side of the water blocks.

Finally, when the optimal kVp and mAs were determined, a calibration line was plotted as was done for CT and the minimum detectable calcium concentration was found. This was again estimated by the product of the standard deviation and the inverse of the slope of the calibration line. For this, the cell phantom was placed between the water blocks to best approximate thoracic geometry.

To study the affect of kVp on quantitation, the cell phantom was placed on the detector side of the water blocks and imaged at four different kVps: 80, 100, 120, and 140. The mA was 20 for all of these. Subtraction masks were made with the same parameters for each of these scans. Fig 48 shows the data from these scans. Centered symbols correspond to mean pixel values and error bars to one standard deviation.

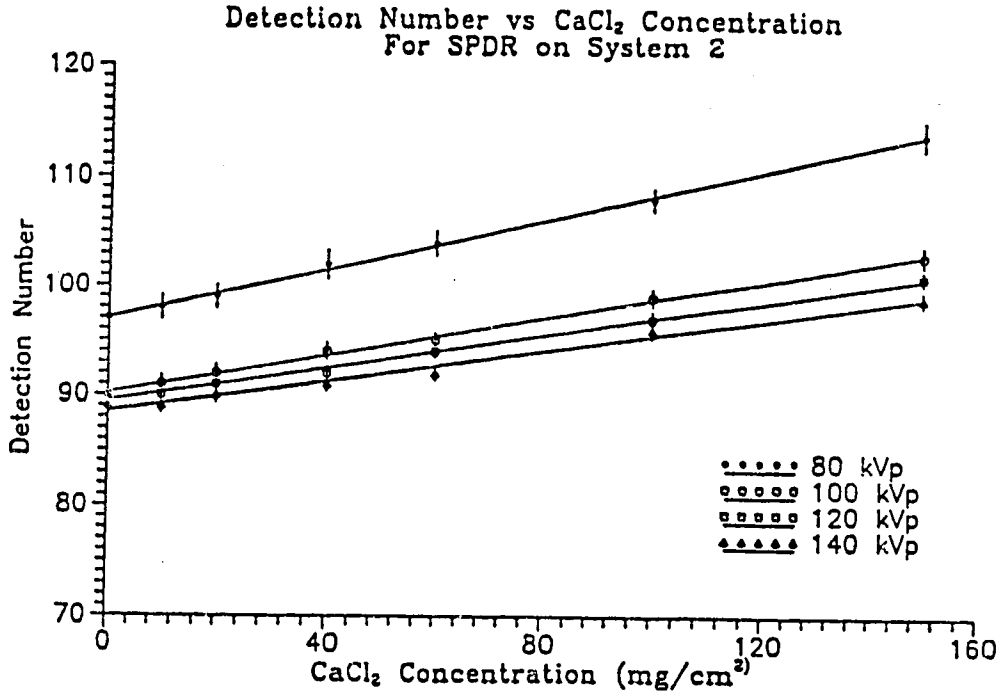

Fig. 48 Calibration lines at four energies on system 2. Slope increases with decreasing energy.

There is an increase in both slope and standard deviation as the energy decreases. These trends can be seen more clearly in Figs 49 and 50 which show the change in standard deviation and slope with kVp respectively. The change in detectability with kVp is shown in Fig 51. Note that the error in quantification reaches a minimum at about 120 kVp.

This can be explained as follows. The minimum detectable calcium concentration is a product of the error (standard deviation) and the inverse of the contrast (slope). These are affected in opposite ways by photon energy: higher energies lead to lower statistical errors but increase the inverse of the contrast (or decrease contrast). As the energy increases below 120 kVp, the corresponding decrease in standard deviation dominates over the decrease in contrast. However, at around 120 kVp, the standard deviation curve starts leveling out more quickly

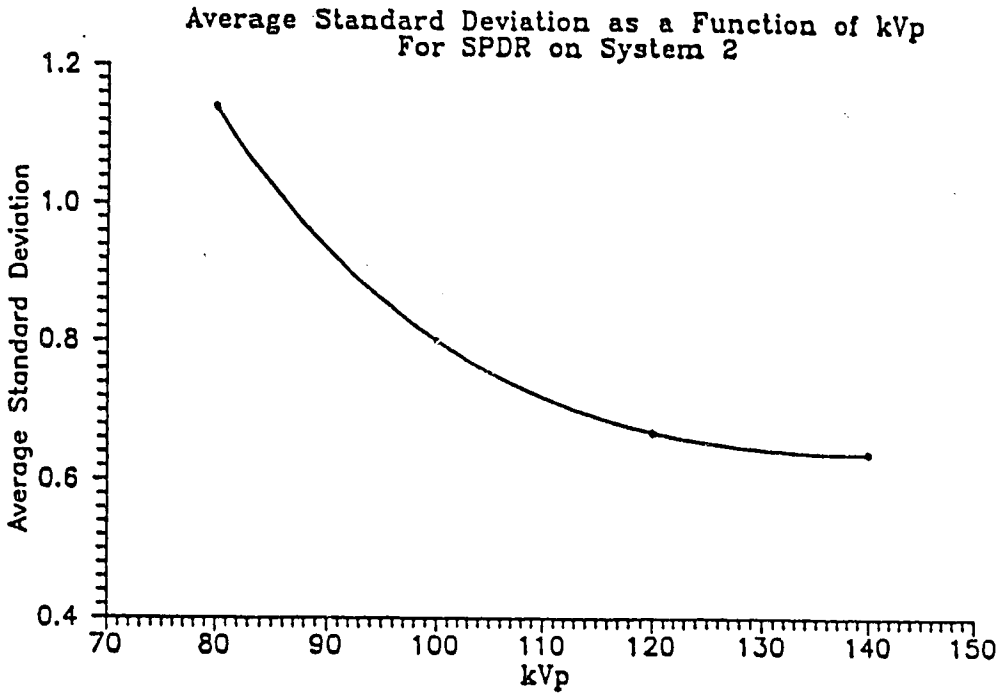

Fig. 49 The standard deviation of the pixel values within the cells dropped with increasing energy.

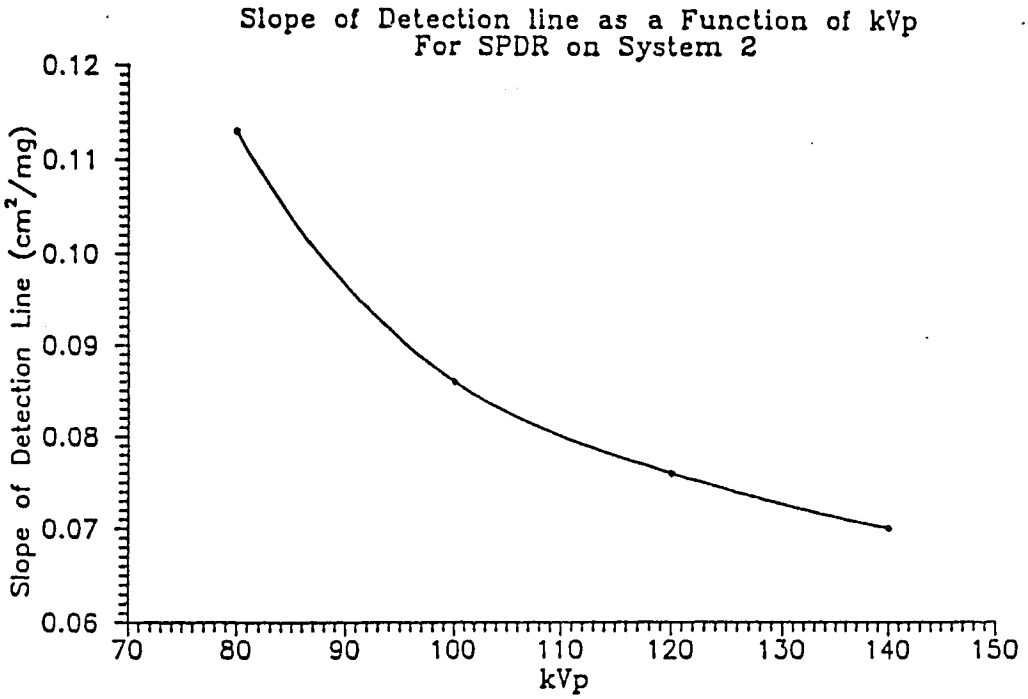

Fig. 50 The slope of the calibration lines drops as kVp is increased.

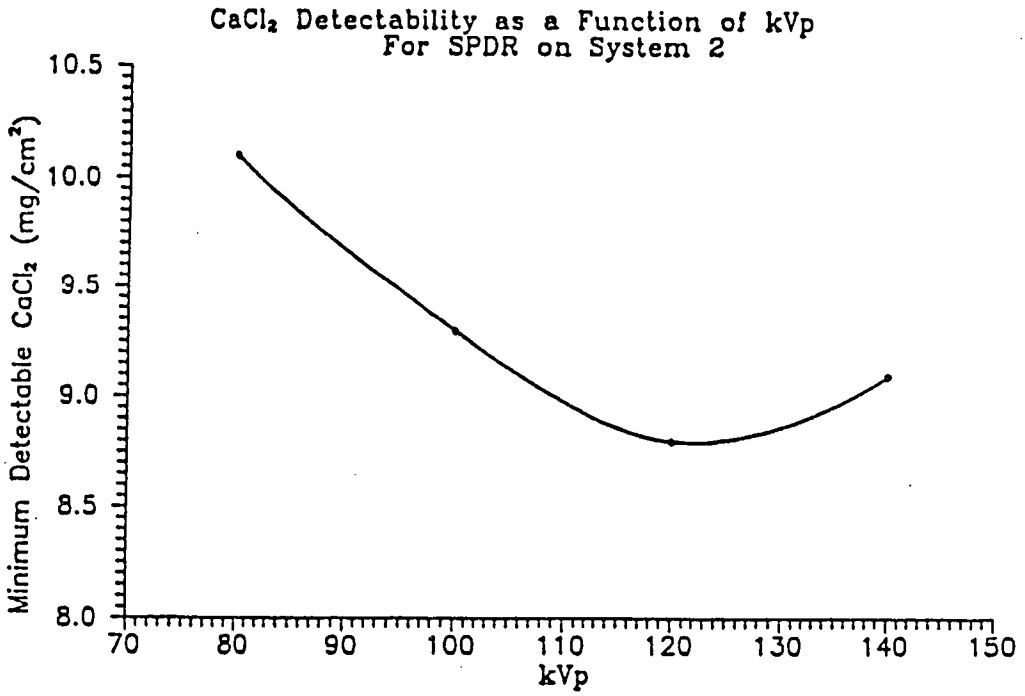

Fig. 51 The optimal peak kilovoltage for detecting Ca on system 2 is approximately 120 kVp.

with kVp than does the contrast curve. Thus, we obtain the best balance between influences of these parameters at around 120 kVp, which becomes our optimum imaging energy.

The affect of mA on standard deviation is shown in Fig 52. Four values of mA were selected: 5, 20, 35, and 50. 130 kVp was used for these scans. Higher mA, corresponding to increased sampling, in general reduces the standard deviation. As the ma increases without bound, the standard deviation would be expected to approach some asymptotic line representing the base level of noise. However this also increases patient dose. The curve changes sufficiently slowly after 35 mA for that to be considered an optimal value.

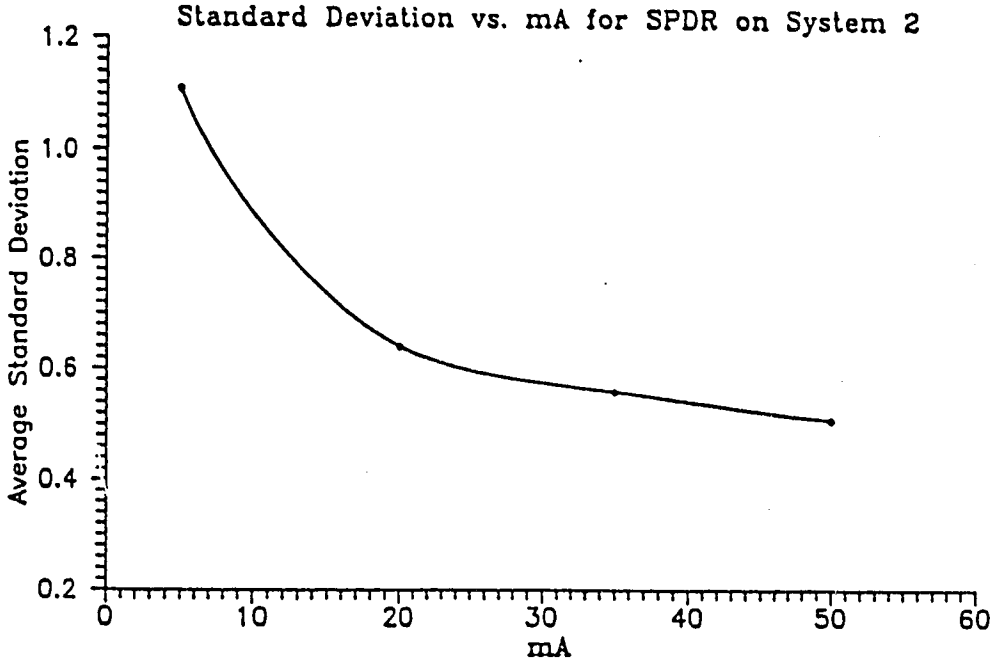

Fig. 52 The standard deviation of the pixel numbers in the cells decreased with increasing mA.

Lastly, the affect of beam hardening on standard deviation is shown in Fig 53. On this graph, 0 cm pre-phantom absorber corresponds to the cell phantom being on the tube side of the water blocks. This parameter would, of course, be determined by the patient geometry. It is, however, interesting to see what effect patient size has. Thoracic geometry is best approximated by the cell phantom being between the water blocks and this is the configuration that will be used for best case analysis.

The best case parameters then are a centered phantom, 35 mA, and 120 kVp. The detection line obtained under these conditions is shown in Fig 54. The centered symbols again represent the mean, with one standard deviation error bars. The minimum detectable calcium is given by the average standard deviation multiplied by the inverse of the

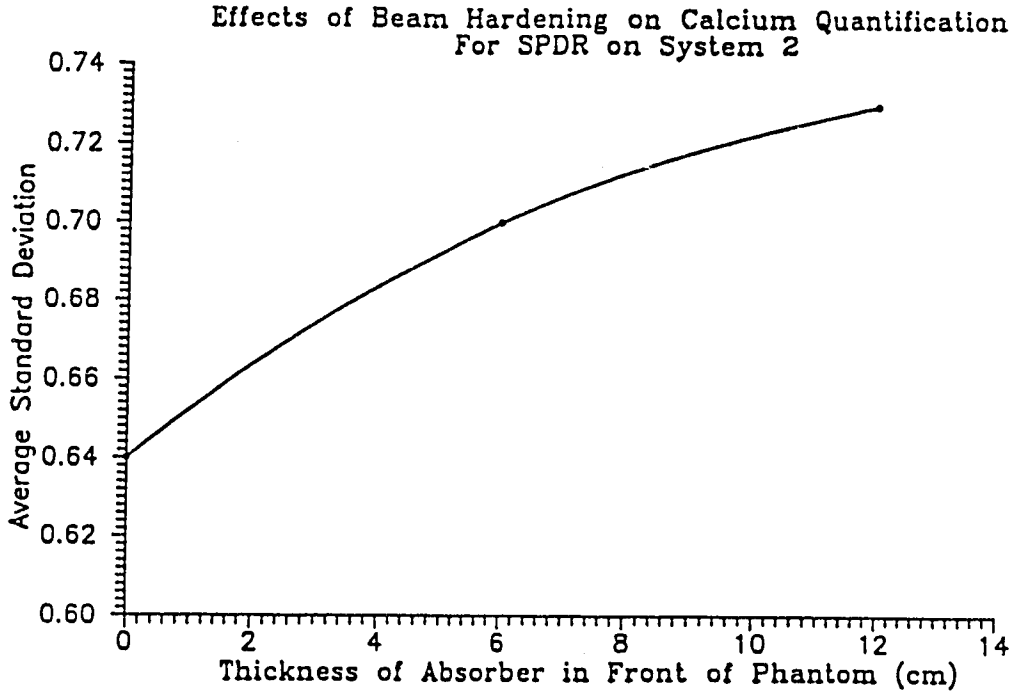

Fig. 53 Beam hardening can lead to poorer Ca detection in SPDR.

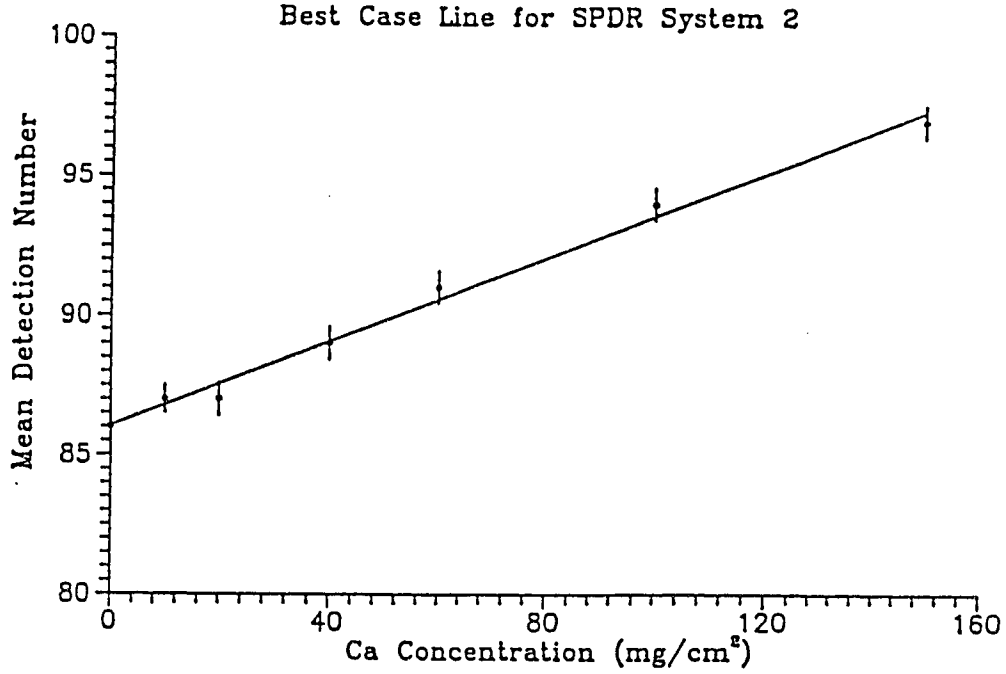

Fig. 54 The optimal SPDR calibration line for Ca detection on system 2.

slope. It is 7.8 mg/cm^2, which corresponds to 7.8 mg/ml in a nodule of 1 cm depth.

3.3.3 System 3

System 3 was significantly different than system 2. This was a pulsed scanner, and so pulse width could be selected to be 1.5 or 3 msec. Also, this system allowed a selection of two slice thicknesses for SPDR: 2 and 4 mm. However, kVp was fixed however at 125 kVp. Service routines might have been capable of changing the kVp, but because system 3 was not from the University Hospitals vendor service functions were not explored. mA values were unavailable.

Also, unlike system 2, system 3 applied convolution to the data before displaying it as a radiograph. A choice of four kernels was available: 1, 2, 3, & 4. Like system 2 however, system 3 had a software feature that allowed image subtraction. This feature was used for all experiments. The following defaults were used for measurements on system 3 unless stated otherwise: 125 kVp, 3 ms pulse width, 4 mm slice thickness, and the cell phantom on the detector side of the water blocks. Kernels were selected as individually listed.

The only experiment on system 3 which had a direct counterpart on system 2 was the beam hardening experiment. This was performed in the same manner as for system 2. The kernel used was kernel 2, pulse width was 3 ms, and the slice thickness was 4 mm. The results are shown in Fig 55. The curve has roughly the same shape as that for system 2. Quantitative comparison would not be valid since parameters are not optimized for either system.

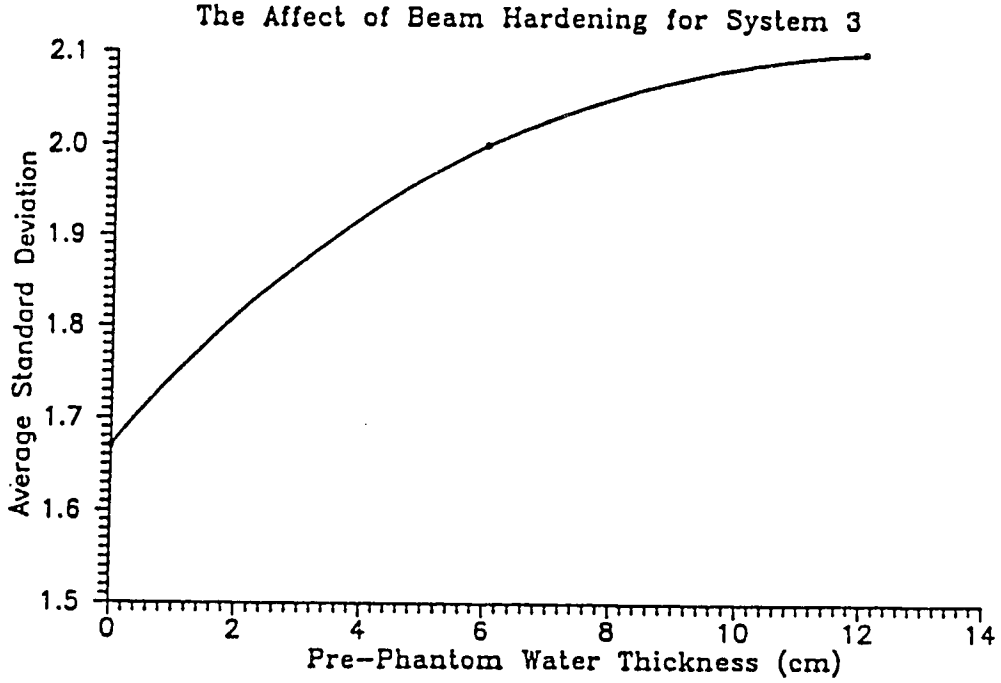

Fig. 55 The effects of beam hardening for SPDR on system 3.

Four convolution kernels were available. The effect of each of these kernels is shown in Fig 56. This data was taken with 3 msec pulse width and 4 mm slice thickness. A linear fit was used, although the data would be better fitted by a curve. This is especially evident for kernels 1 and 4. This is not an exposure nonuniformity, since subtraction from a uniform phantom has been performed. Also note that the lines with the largest slopes correspond to the kernels which produce the largest standard deviation, as displayed by the error bars.

The error in quantification (and thus the minimum detectable Ca) was calculated for each of these lines to determine the optimal kernel. The results are shown in the bar graph in Fig 57. Kernels 2 and 3 are similar at 70.2 and 63.6 mg/cm^2 detectable calcium respectively. Kernels 1 and 4 are considerably worse at 165.8 and 116.9 mg/cm^2 detectable Ca respectively.

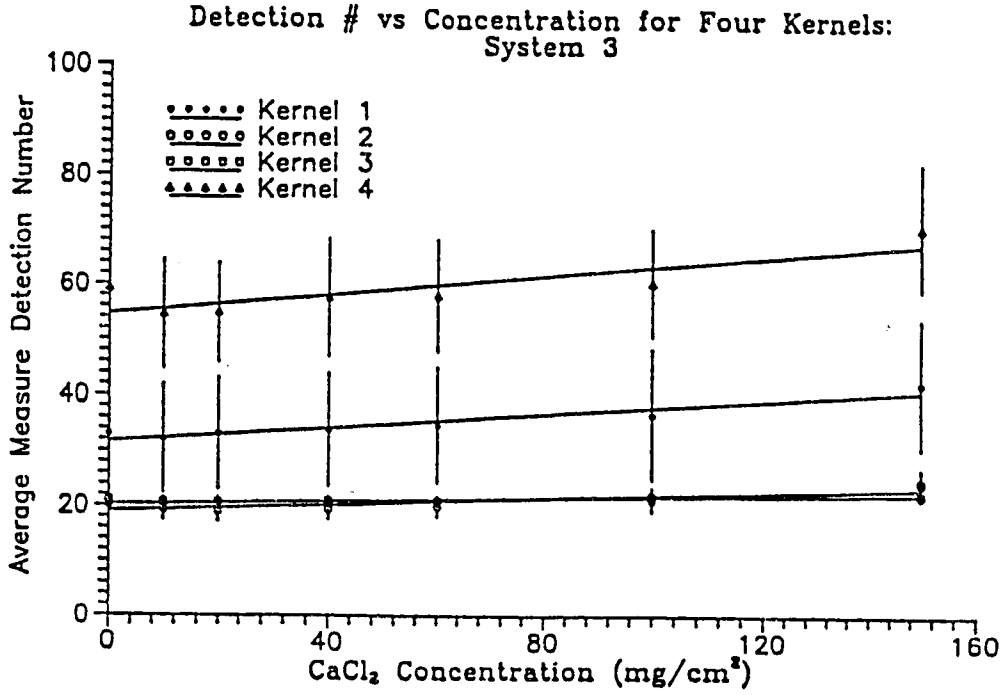

Fig. 56 The use of kernels in the reconstruction of SPDR images on system 3 led to nonlinearity.

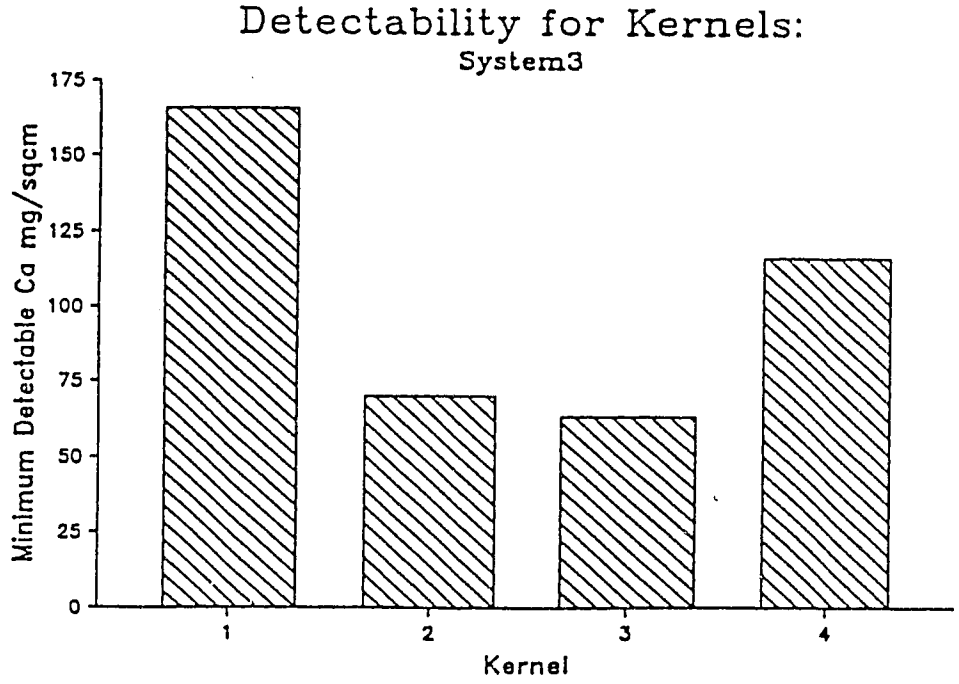

Fig. 57 The choice of kernel led to significant differences in Ca detectability for SPDR images on system 3.

System 3 allowed two choices for both pulse width and slice thickness. Experiments on these parameters were performed with kernel 3. Both parameters affected only the standard deviation. The results of these experiments are shown in Figs 58 and 59. With only two points per parameter the choice of a linear fit is arbitrary. Increases in either pulse width or slice thickness increase the volume sampling, and thus create the expected reduction in standard deviation.

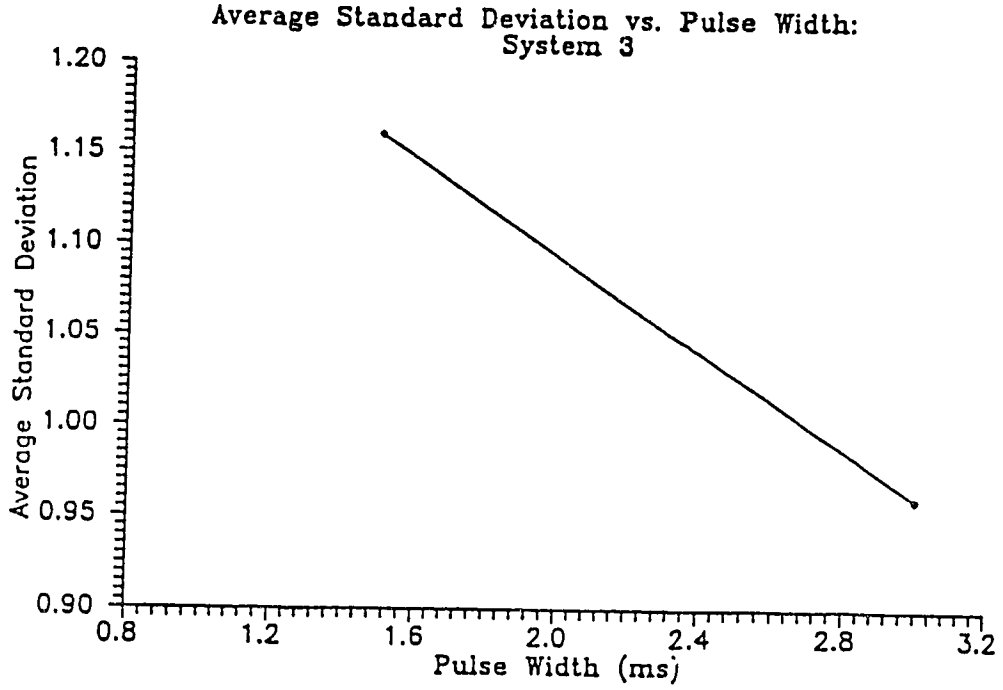

Fig. 58 Increasing the pulse width decreased the Ca detection error for system 3.

The optimal quantification parameters for system 3 were thus: kernel 3, 4 mm slice thickness, 3 ms pulse width, and cell phantom placed between water blocks. The results are shown in Fig 60. The detectability formula can be applied to obtain a minimum detectable concentration of Ca of 64 mg/cm^2.

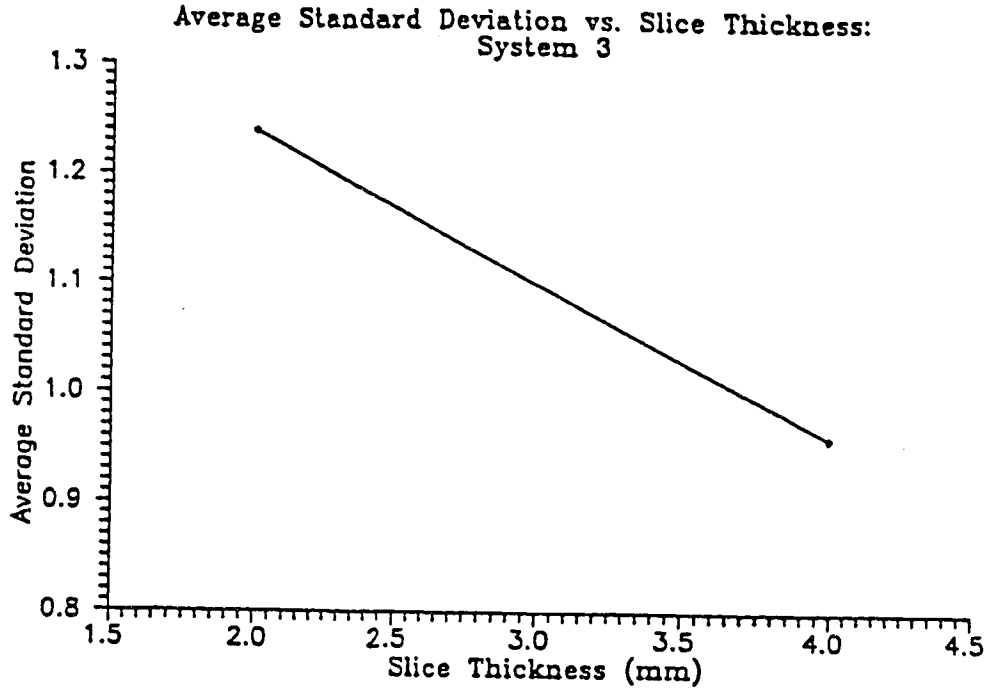

Fig. 59 Increasing the slice thickness decreased the error on system 3 for SPDR images.

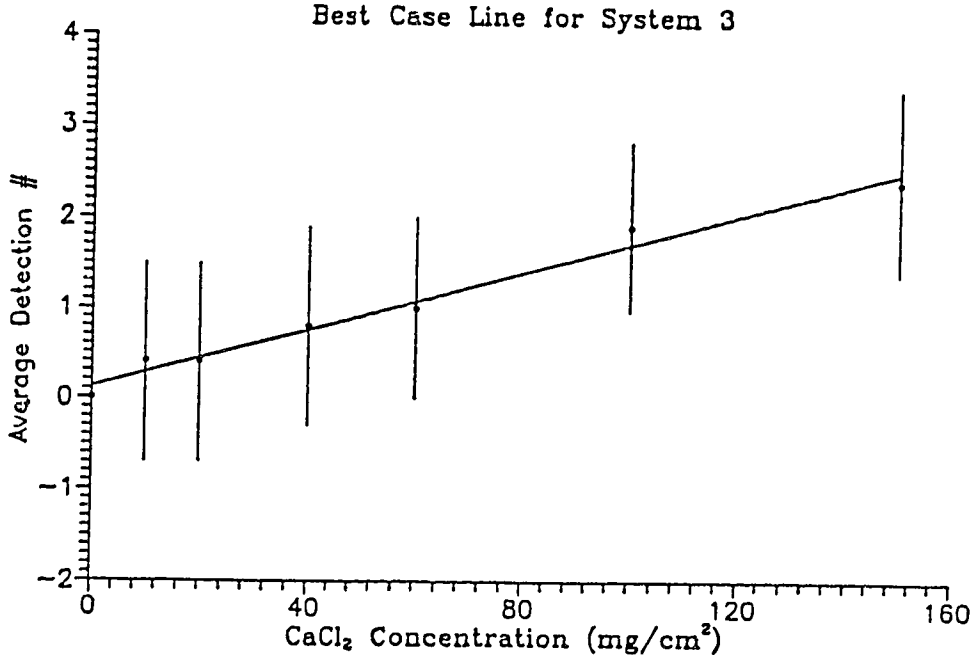

Fig. 60 The optimal SPDR calibration line for system 3 has huge errors.

3.3.4 Comparison of SPDR Units

Comparing the best case line for systems 2 and 3 in Fig 61 it is apparent that system 2 has a greater slope and smaller error bars than system 3. This is reflected in their respective minimum errors of 7.8 mg/cm^2 Ca for system 2 and 64.0 mg/cm^2 Ca for system 3. This comparison is shown graphically in Fig 62.

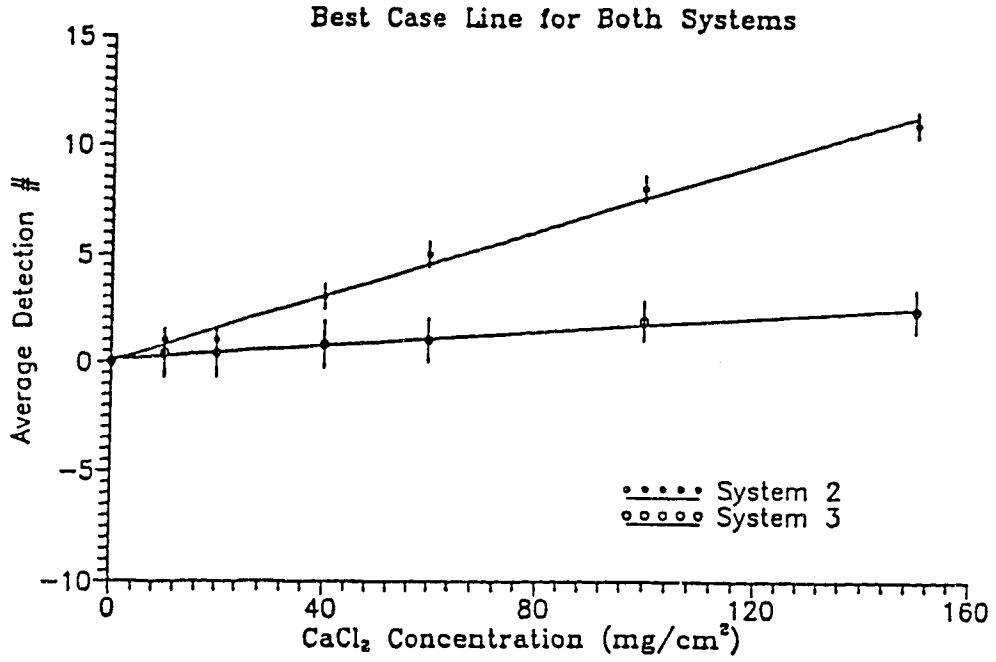

Fig. 61 A comparison of the optimal SPDR calibration lines for systems 2 and 3.

The average optimal standard deviation for system 2 was approximately 0.6 while for system 3 it was approximately 1.0, or about 67% greater. The major difference is in the slope of the lines. This is most likely due to the fact that system 3 convolves the projections before creating an image from them, producing nonlinear results.

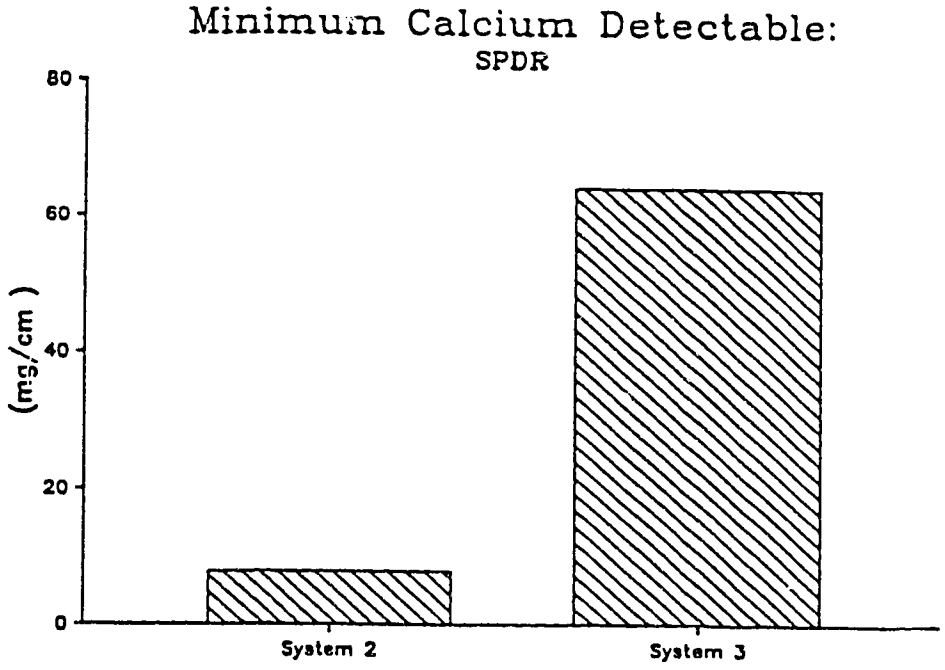

Fig. 62 System 2 is vastly superior for Ca quantification using SPDR.

This nonlinearity is not evident in Fig 56. Unfortunately, the kernel producing the most linear image also has the least contrast, and thus the smallest slope. However, this kernel also produces the smallest standard deviation and therefore provides optimal quantification. The lowest standard deviation in the most linear kernel is not surprising since there would be no superimposed variation of pixel values over the region of interest defined by the cell.

3.4 Conclusions and Summary

In this chapter, two methods of performing digital radiography were investigated. Image Intensifier (II) based systems were not fully explored due to a lack of suitable equipment. The investigation of this modality that was undertaken showed only that multiformat camera film

lacks the dynamic range to make Ca quantification feasible. Further investigation of this modality is warranted when appropriate equipment is available.

Although a prototype chest unit using SPDR has been used[2] for detection of calcification in SPNs, this work could be made of much greater value if applied to CT scanners. Scan projected radiography is currently the method whereby anatomical reference is provided for slice selection for CT. Experiments as to the feasibility of this were discussed in this chapter.

At present, most CT manufacturers do not provide SPDR for quantification purposes. The GE 9800 did not provide the ability to obtain pixel values from a digital radiograph. The Picker 1200 SX did, and even allowed selection of kVp and mA through service routines. Image subtraction was also possible. The Siemens DRH provided pixel values, but it is uncertain whether or not kVp could be altered. Subtraction of images was also possible for this machine.

Of the two systems for which quantitation was possible, system 2, the Picker 1200 SX, provided an error of only 7.8 mg/cm^2. System 3, the Siemens DRH, applied convolution to its radiographs which seems to have altered the reliability of the pixel values for quantitation. A Ca quantitation error of 64.0 mg/cm^2 was observed for this unit.

For future SPDR work, dual energy subtraction could readily remove the contributions of non-uniform tissue depth. This further processing would certainly induce some additional error. This additional error has not yet been investigated, but is crucial to the eventual comparison of the quantitative usefulness of digital radiography and CT.

Chapter 4 : Computed Tomography

4.1 Materials and Methods

Of the three imaging methods discussed in this thesis, the one most commonly employed at present for light element quantification is computed tomography (CT). There is good physical reason for this. During a single CT tomogram, approximately 10 times as many x-ray photons may interogate a volume of tissue as for a single analog x-ray image. Furthermore, less than a tenth of the object volume included in an analog image is typically imaged in the tomogram. Thus, although the collimated fraction of photons is higher for CT, the volume sampling density is substantially higher than in analog radiography case, and thus the composition of the object volume can be determined more accurately.

This greater sampling and the fact that there is no overlaying of object structures in CT give it a substantial advantage in low contrast detectability which has been applied to calcium quantitation in SPNs[1]. However, one important consideration that has not been adequately addressed is the minimum calcium concentration that can be accurately detected.

A calcium concentration of 40 mg/ml has been used as the critical level for detection of benignancy in SPNs. This figure was in fact obtained in a study performed with a CT scanner[4], one of the pioneering works that has led to the subsequent commercial development of calcium detection systems for CT. In this chapter an estimate of the error in

this critical concentration will be obtained based on physical considerations. Furthermore, since CT has become the standard for quantification, this error will provide a measure of the minimum calcification detectable against which other modalities may be compared.

In order to do this a phantom purchased by the University of Alberta Hospitals Department of Radiology as part of a bone mineral measuring package was employed. This phantom is a bi-truncated pseudo-elliptical cone (see Fig 63). The walls of this cone are ~5 mm thick perspex and the interior is filled with water. Through the cone, parallel to the "bottom" wall, runs a right circular cylindrical hole. The phantom is designed to mimic a range of abdominal thicknesses, and calcium filled rods are placed in the cylindrical hole to simulate vertebral bone calcium.

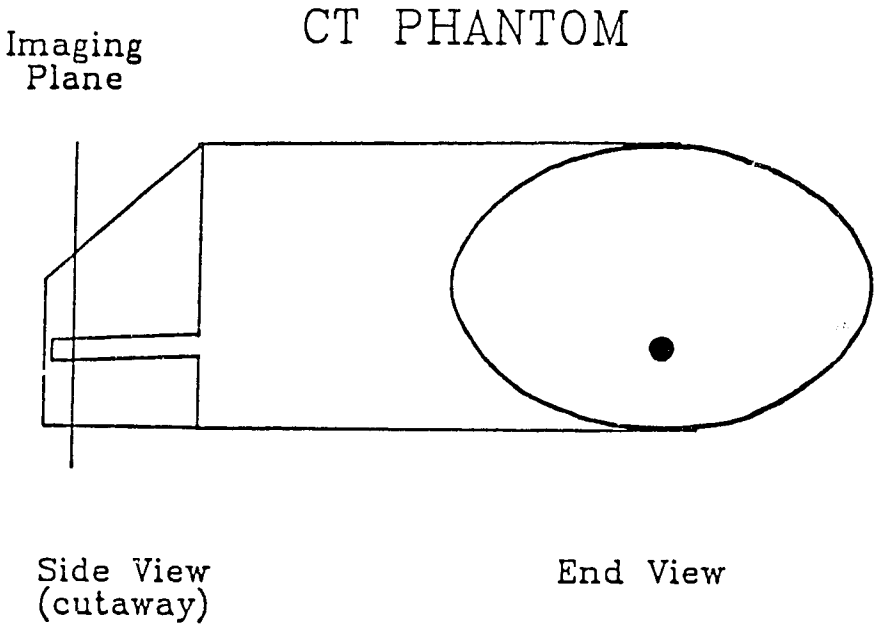

Fig. 63 The commercial bone mineral phantom used for CT experiments.

The phantom was supplied with three plastic cylinders, each containing a different concentration of K_2HPO_4. The concentrations are 50, 100, and 200 mg/ml. To augment this selection, three more cylinders were constructed. These were 2.5 cm outside diameter perspex tubes with 1 mm wall thickness. They contained 25, 75, and 150 mg/ml concentrations of $CaCl_2$ solutions.

In order to provide representative data three CT imaging systems were studied: two from the University of Alberta Hospitals and one from the Grey Nuns' Hospital in Edmonton. Data was collected by aligning the phantom's Ca cylinder with the CT gantry center and obtaining a tomogram. Region of interest (ROI) algorithms supplied in the manufacturers' software were used to obtain means and standard deviations of pixel values over a circular region within the imaged cross section of each cylinder.

Experiments were performed by adjusting various imaging parameters such as kVp and slice thickness. Two parameters, however, were held constant. Slices (tomograms) were always taken over a 360° arc and image reconstruction matrices were always taken to be 512 x 512.

Two values characterize the ability of a system to quantify. One is the change in the mean value of the measurement (m) of a quantity with respect to the actual change in the quantity itself (x). The second is the error in the measurement (Δ). If the mathematical relationships between the quantity (x) and the measurement ($m = m[x]$) and the quantity and the error ($\Delta = \Delta[x]$) are known, one can estimate the ability of a system to quantify any quantity.

Detectability (d) is the smallest quantity that can be distinguished from 0. It is given by:

$$(4.1.1) \qquad d = \frac{\Delta(x)}{dm/dx}\Big|_{x=0}$$

Note that *increasing* detection capability corresponds to *decreasing* detectability.

For the case of calcium quantification in CT, the measurement is given by the mean CT# and the error is given by the standard deviation (s). The CT# should be linear with respect to the calcium density (x) (CT# = ax + b, a and b constant) and the standard deviation should change slowly enough with the concentration that it can be considered to be constant. Thus the detectability will be:

$$(4.1.2) \qquad d = s/a$$

The detectability of calcium for a CT scanner can therefore be determined by measuring the standard deviation and the slope of the line relating mean CT# to calcium concentration.

4.2 Imaging Parameters in CT

In section 4.1 it was stated that detectability can be calculated from the slope of the linear relationship between mean CT# and calcium concentration (the calibration line) along with the standard deviation. The intent is to optimize imaging parameters in order to obtain the best possible detectability. Various parameters are expected to influence the two numbers needed to calculate detectability. They are:

kVp, mAs, slice thickness, digital filter, and patient geometry (the thickness of the absorber around the measured concentration). Experiments were performed to vary each of these parameters individually and observe the affect on the two measurements needed for calculating detectability.

Differences between systems led to differences in parameters for experiments performed on them. Parameters that were not those studied in a given experiment were set to default values. The default values for each system are shown in Table 14.

Table 13 Default Parameters for CT Experiments

Parameter	System 1	2	3
kVp	80	100	96
mAs	200	210	240
slice (mm) thickness	10	10	8
algorithm	standard	adult head	smoother body

An average water thickness of 10.5 cm was the default for all systems. These defaults were always used except where stated.

4.2.1 kVp

kVp can affect the detectability through both the slope of the calibration line and the standard deviation. The slope was affected in two competing ways. Because low energy x-ray photons are absorbed preferentially to high energy photons, the lower the effective energy of the poly-energetic beam from the x-ray tube, the greater the number of photons that will be absorbed. This increases the percent difference

between the number of photons absorbed by attenuators of different density (ie. increases the contrast). Thus, the slope of our calibration line would be expected to increase, improving (ie decreasing) the detectability.

However, the effective energy of the unabsorbed photons increases towards the center of the phantom because less energetic photons are absorbed preferentially. This 'energy shift' due to attenuation is called beam hardening. Beam hardening decreases sensitivity to the density difference between cylinders and thus the slope of the line. Since lower kVp beams are hardened more, this affect tends to oppose the one mentioned above. However, the increase in contrast with decreasing kVp is always greater than the beam hardening affect.

There are two kVp dependant phenomena affecting the standard deviation of the pixel values. At lower kVp, beam hardening in the surrounding water leaves fewer photons to sample the calcium cylinder. Since the standard deviation is given by $\sqrt{N}$ this increases the standard deviation. Also, beam hardening in the cylinder itself will further deplete the supply of photons sampling the center. This creates a nonuniform sampling within the cylinder and thus a nonuniform distribution of CT#'s over the cylinder's circular cross section, further increasing the standard deviation.

To test the contributions of each of the above effects all six of the calcium rods were measured at various energies on all three systems. The energies used for each system are shown in Table 14.

Table 14 kVp's Used for Experiments on Three CT Units

System	Energies (kVp)
1	80, 120, & 140
2	100, 120, & 140
3	96 & 125

Figs 64-66 contain the calibration lines for the three systems. Error bars represent ± 1 standard deviation. Lines were fit using linear regression. Note that there are two lines for each energy, one for the K_2HPO_4 cylinders and one for the $CaCl_2$ cylinders. This is not surprising. Generally, different attenuators will produce different detection characteristics.

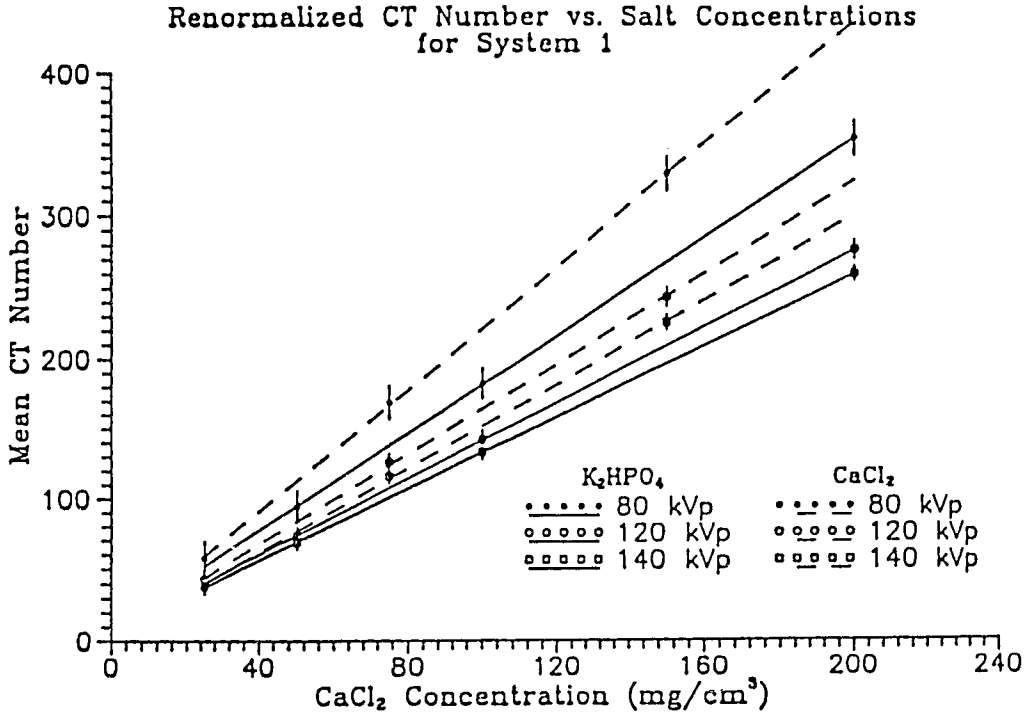

Fig. 64 The calibration lines for three imaging energies and both salts on system 1.

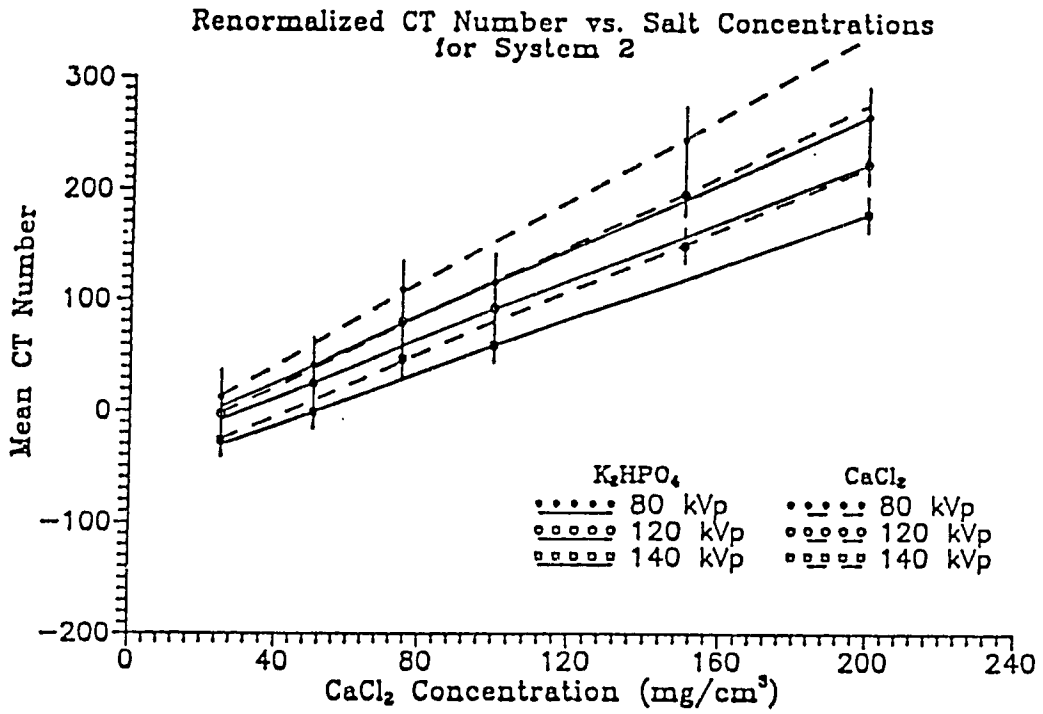

Fig. 65 Calibration lines for both salts at three energies for system 2.

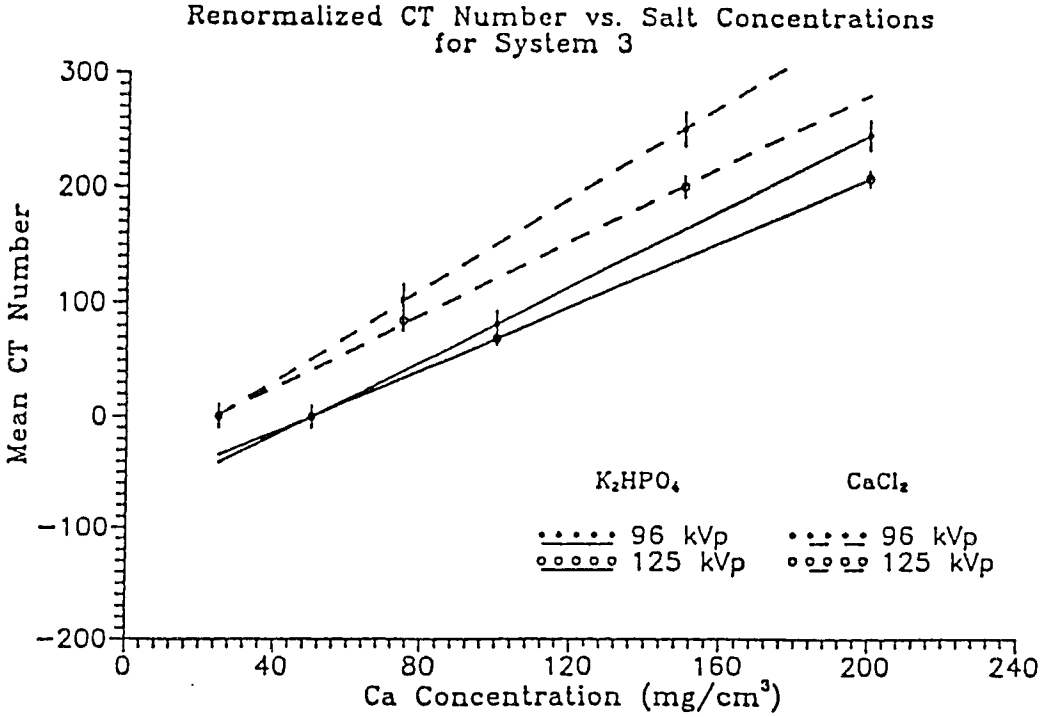

Fig. 66 Calibration lines for both salts at three energies on system 3.

Several features are evident from this graph. The standard deviations seem generally to increase for lower kVp's as predicted above. This is explicitly shown in Fig 67, where the mean standard deviation for a given energy (both salts) is plotted with respect to kVp for all three systems. Likewise, the expected increase in slope at lower kVp is shown in Fig 68. Using equation (4.1.2) one can determine how the detectability of Ca for this system varies with kVp. This is shown graphically in Fig 69. The data in these last three graphs were fitted with cubic splines.

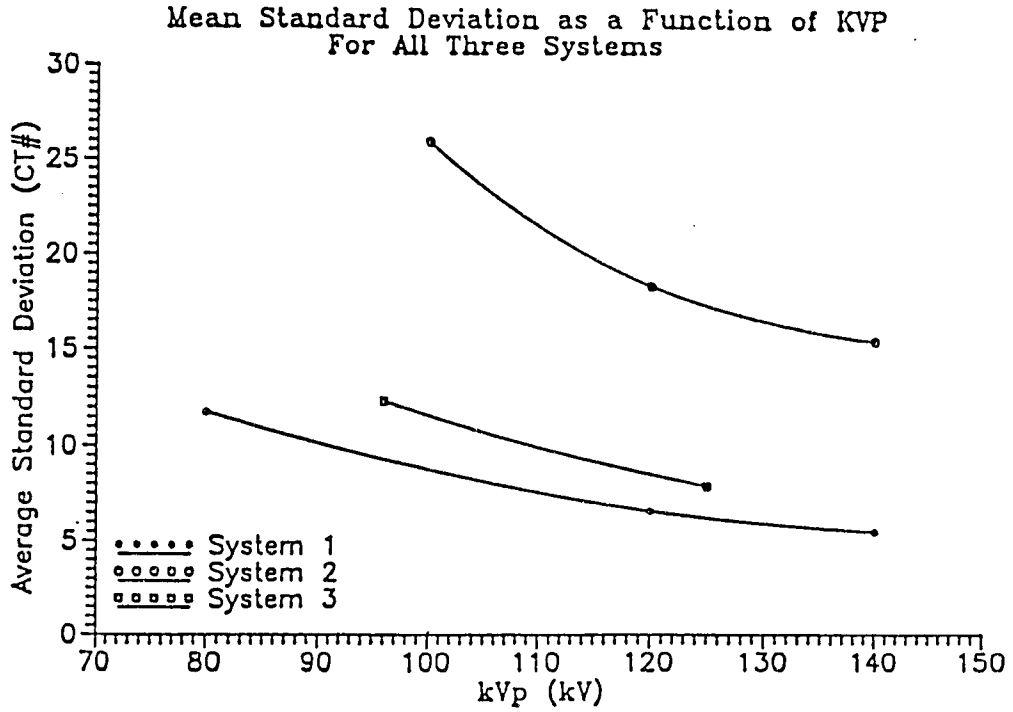

Fig. 67 The standard deviation of CT#'s decreases as the imaging energy increases on all three systems.

It is interesting to note that the detectable concentration for both salts decreases with kVp on all three systems. This means that the increase in standard deviation due to beam hardening is affecting the detectability more strongly than the increase in slope due to contrast sensitivity. It implies that the patient should be scanned at higher

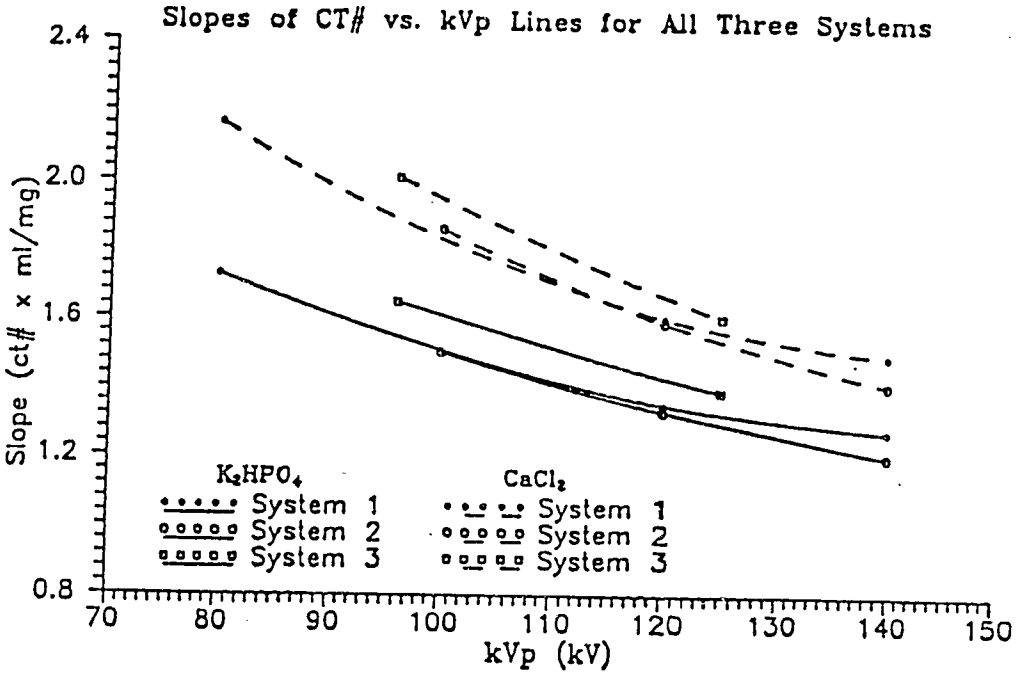

Fig. 68 The slopes of the calibration lines decrease with increasing energy on all three systems.

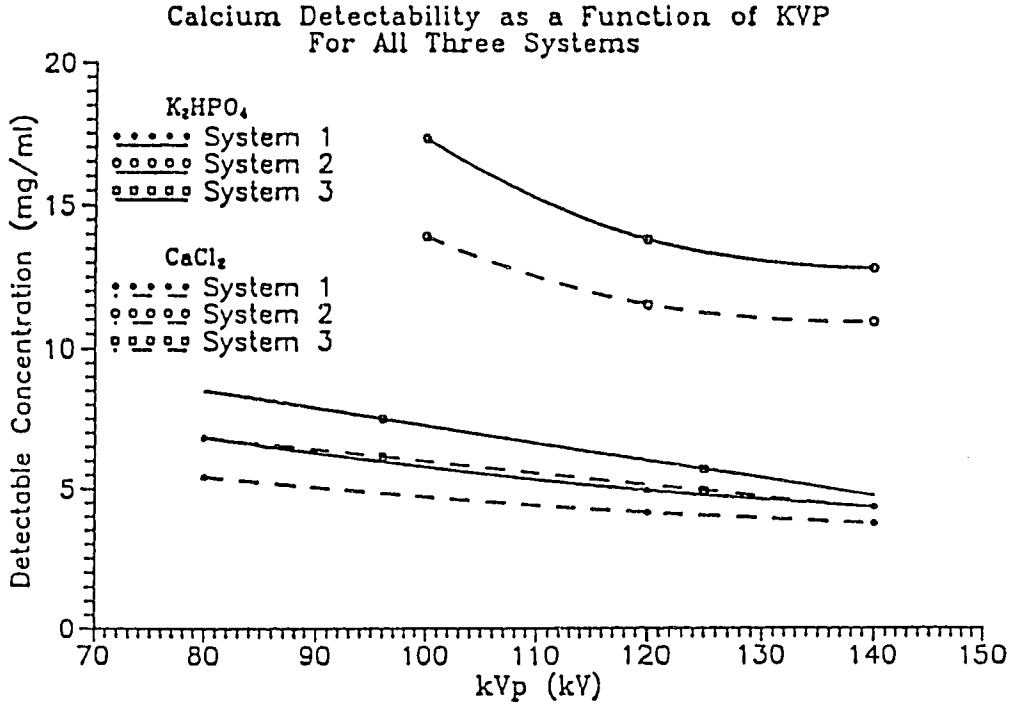

Fig. 69 Ca detectability improves with kVp on all 3 CT systems.

energies, which will fortunately lead to less absorption of x-rays in the patient and thus a decreased radiation dose. Also interesting is that the potassium salt is significantly harder to detect than the calcium salt for all systems. This will be discussed later.

Figs 64-69 show significant differences between the affects of kVp on calcium quantification capabilities for the three systems. However, at this point the systems cannot be compared meaningfully because all parameters have not yet been optimized. This is especially significant with respect to the choice of algorithm, where defaults were chosen fairly randomly. The information of primary importance to be gained here is that detectability is optimized at the highest kVp for CT systems.

4.2.2 mAs

mAs is simply a measure of the number of photons emitted during a scan. As discussed previously, it is generally higher for CT than planar radiography. The number of photons produced would not be expected to change the slope of the calibration line, since the percent difference of photons absorbed by different absorbers would remain constant. However, it should affect the standard deviation, since there will be more photons to sample a given volume of the object.

Preliminary results showed no change in calibration slope with mAs. To observe the change in standard deviation as a function of mAs the 25 mg/ml cylinder was measured on all three systems at various mAs's, listed in Table 15.

Table 15 mAs's for Experiments on Three CT Systems

System	mAs's
1	60, 200, 480, & 960
2	100, 120, & 140
3	96 & 125

The results are shown in Fig 70. The points were fitted with a cubic spline. This led to the appearance of a minimum between the last two points for systems 1 and 3 which is simply a feature of the fit and has no physical significance. The manner in which this curve flattens out suggests that one might not attain significantly better results with an mAs above 500 on any of the systems. This will be taken as the optimal value for this parameter.

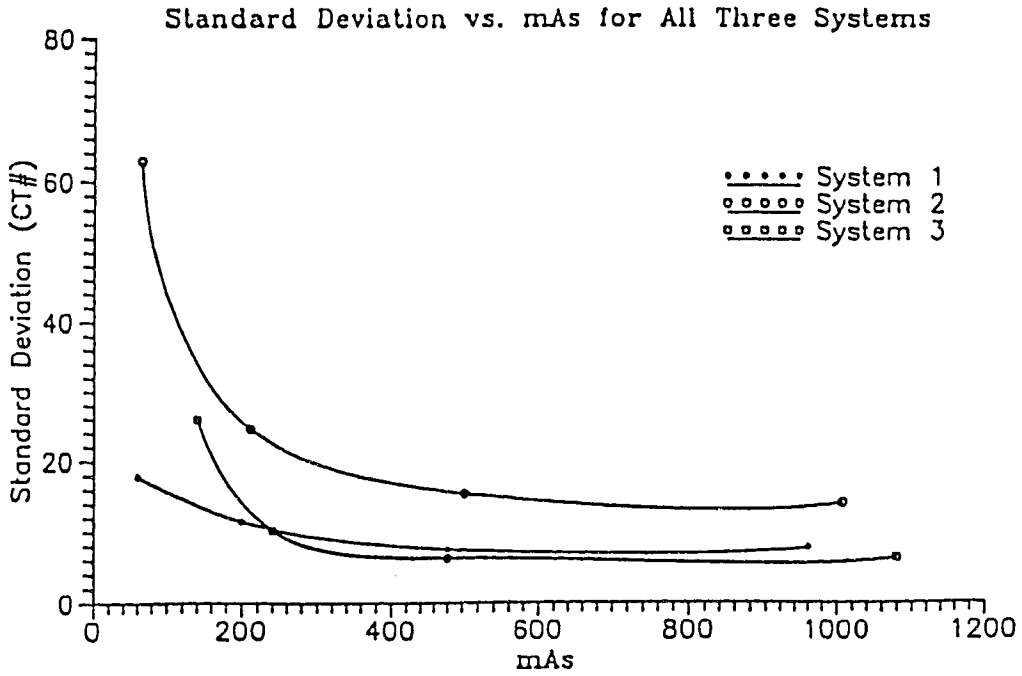

Fig 70. The standard deviation of CT#s decreases as mAs is increased for all three CT systems.

Although the data points in Fig 70 cannot be compared, as was explained in the last section, the shapes of the curves can. It is interesting to observe that the standard deviation of pixel values for systems 1 and 3 have a much stronger dependance on mAs at lower mAs than system 2. Since standard deviation proved to be the more significant contribution to detectability in the kVp experiments, this suggests that systems 1 and 3 will have greater ranges of detectabilities than did system 2. Whether these larger ranges contain higher detectabilities than the system 2 range can only be determined after parameter optimization.

4.2.3 Slice Thickness

Increasing the mAs increased the volume sampling and thus decreased the standard deviation over a given image area. There is another factor that affects standard deviation. The standard deviation varies with the sampling in an image *area*, but each image area corresponds to an object *volume*. Thus increasing the mAs actually increases the number of photons sampling a given patient volume.

An increase in image area sampling can be created in another way: one can increase the volume corresponding to an image area. This is done using slice thickness. Although the mAs, and thus the volume sampling, are held constant, slice thickness can be changed by collimators at the source and detectors. This leads to a change in image area sampling and thus to a change in standard deviation. Based on this, one would expect a lower standard deviation at larger slice

thickness. Of course, spatial resolution of the image is degraded by increasing slice thickness.

To investigate this phenomenon, the standard deviation over the 25 mg/ml cylinder was measured for various slice thicknesses on the three systems. The slice thicknesses used are shown in Table 16.

Table 16
Slice Thicknesses for Experiments on Three CT Systems

System	Slice Thicknesses (mm)
1	1.5, 3, 5, & 10
2	1, 3, 5, & 10
3	2, 4, & 8

The results of these experiments are shown in Fig 71, which shows graphically that the maximum practical slice thickness should be used for Ca quantification. This may not always be the largest slice thickness available for a system, as will be discussed later.

For all parameters that have been investigated so far, the qualitative behaviour of the systems has been similar. Slice thickness is the first parameter for which this is not true. The curve for system 3 in Fig 71 is convex in contrast to the concave curves for systems 1 and 2. One reason that a convex curve is anomalous is that it does not approach the x-axis asymptotically. Thus one would expect that at some slice thickness the standard deviation could be made to be 0 or even negative. Of course, this can never be.

The only plausible explanation for this behavior is that for some reason the collimation is not varying properly between the 2 and 4 mm slice thicknesses, and thus the standard deviation is not changing. Unfortunately, because this scanner belonged to another institution it

was not possible to do the detailed experiments necessary to verify this.

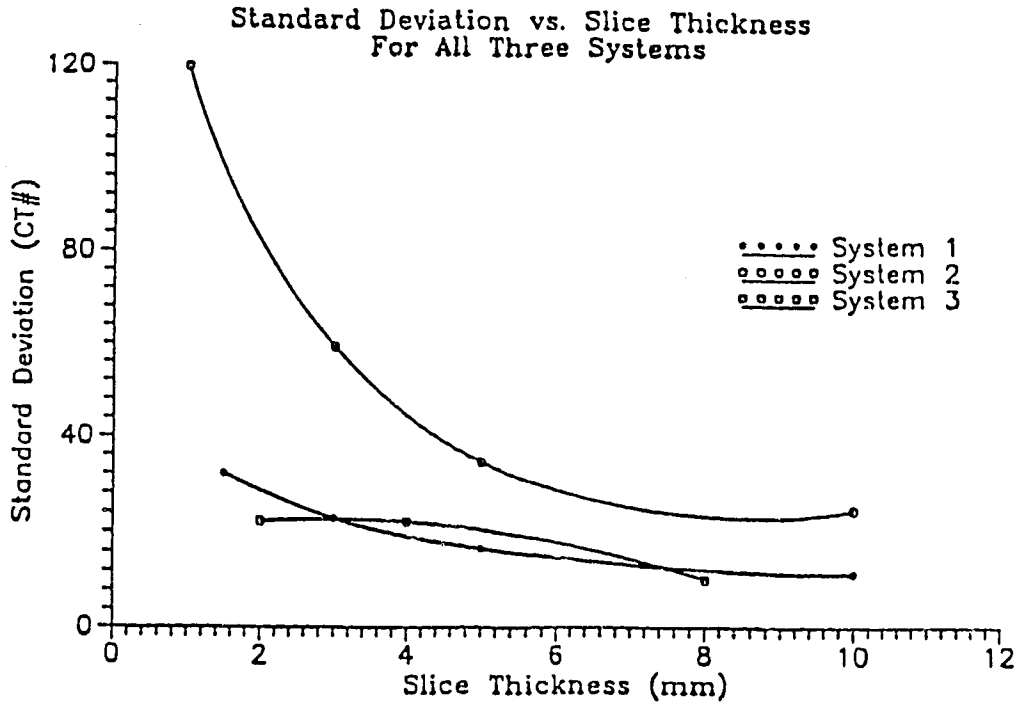

Fig. 71 CT# standard deviation decreases with increasing slice thickness, but system 3 behaves anomolously.

4.2.4 Patient Geometry

The amount of the water surrounding the calcium cylinder, which approximates the chest walls, will dictate the degree of beam hardening. An increase in wall thickness would be expected to produce more beam hardening and thus an increase in the standard deviation of the calcium measurements. To test this the 25 mg/ml cylinder was placed in the phantom , and the phantom was scanned at 10.5, 13.6, 16.8, and 19.9 cm average wall thicknesses on all three systems. These values for average wall thickness were obtained by measuring the circumference of

the pseudo-elliptical phantom at the center of the slice and calculating the radius of the circle with the same circumference.

The results are shown in Fig 72. Data are fitted with an exponential regression. The increase in the standard deviation with wall thickness is apparent. While detectability is optimized by the smallest wall thickness, for clinical purposes the wall thickness is fixed. It is clear, however, that beam hardening can play a significant role in Ca detectability.

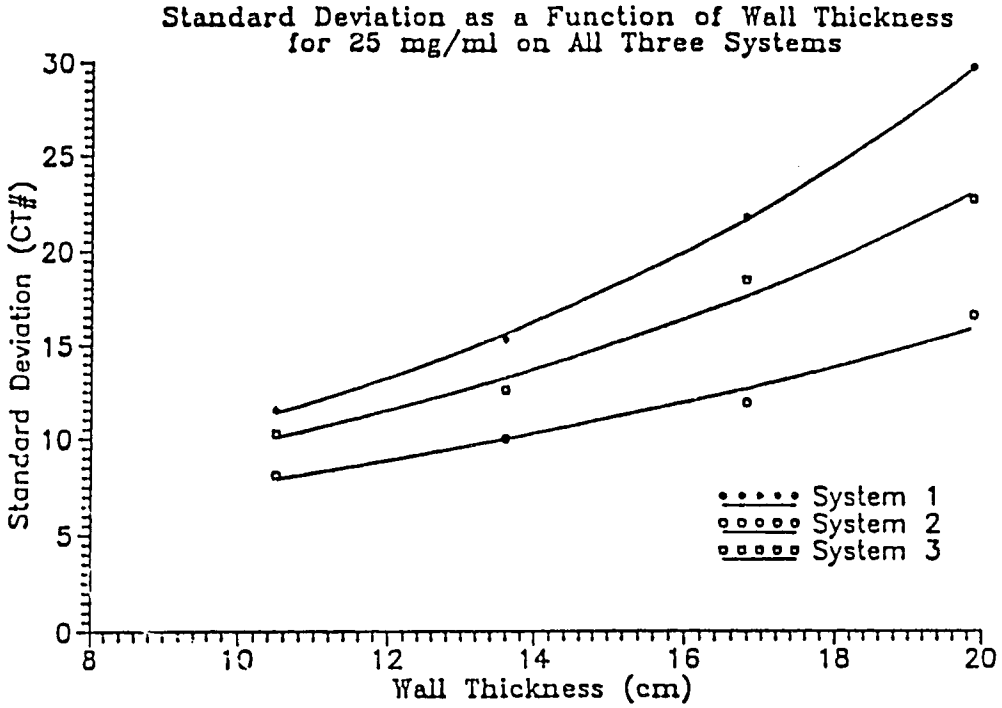

Fig. 72 The effects of beam hardening are apparent on all three CT systems. The data are fitted with exponential fits.

4.2.5 Digital Filter

The fundamental concept of CT is that the intensity profile of a transmitted x-ray beam contains information about the density of the object through which it was projected. But the intensity profile is only sampled by a finite number of detectors. When information about

the object density is gathered from the intensity profile, it is implicitly assumed that the information is from a line in the object intersecting the center of each detector, rather than the edge. If this was the extent to which the data was processed, a star artifact would be superposed upon the image. Each arm of the star would correspond to the 'preferred' line from the source to the center of each detector.

In mathematical parlance this can be expressed by the fact that the image distribution (i[x,y]) has been convolved with a star distribution (s[x,y]). The convolution of two functions can be reduced to the product of their Fourier transforms. In theory, then, the transformed star distribution can be divided out, and the inverse Fourier transform applied to obtain the corrected image. This is equivalent to convolving with the Fourier transform of 1/s[x,y]. This function, $s^{-1} = 1/s[x,y]$, is called the digital filter, or kernel, of the deconvolution. The processes used for deconvolution, including the application of the filter, is called the algorithm. Generally speaking, digital filter, kernel, and algorithm are used synonymously.

There is no single method for obtaining s^{-1} nor is there a single function that will give the best results under all circumstances. A variety of functions have been found that give good results in a given situation, and developing new kernels is almost as much an art form as a scientific endeavor.

Some algorithms are 'noisier' than others; that is, they may suppress information and therefore reduce the effective sampling density of the image. Others are more 'smooth'; they tend to produce images in which fine detail is hard to discern. In all cases, there is a trade-off between spatial resolution and contrast resolution.

Although the algorithm will affect the standard deviation (noise), it is applied equally to all regions of the image, and thus does not affect the percent difference of the signals from different density regions in the object.

Because algorithm information is proprietary to the manufacturer, it was difficult to estimate their affects on Ca detectability. Also, each manufacturer lists different names for their algorithms, so it is a difficult parameter to compare between manufacturers. For this reason, default values were chosen virtually randomly.

An experiment was performed to determine the best algorithm for Ca quantitation for each system. On each scanner a set of six images were taken; one for each of the cylinder inserts in the phantom. These were reconstructed with various algorithms for each scanner, as listed in Table 17.

Table 17 Algorithm Used for Experiments on Three CT Systems

System	Algorithm
1	Standard, Soft Tissue Bone
2	Hanning (#3) Special (#4) Adult Head (#6) Adult Head (#10) Shepp-Logan (#12)
3	Standard Body (#1) Smoother Body (#3) Standard Head (#5) High Edge Enhanced Head (#7) Shepp-Logan (#8)

Numbers in parentheses following algorithm names indicate the selection number used by the operator for scanning.

For each algorithm the average standard deviation over the six images was calculated. The results are displayed in the bar graphs of Figs 73-75. Algorithm numbers for systems 2 and 3 are as listed in Table 17.

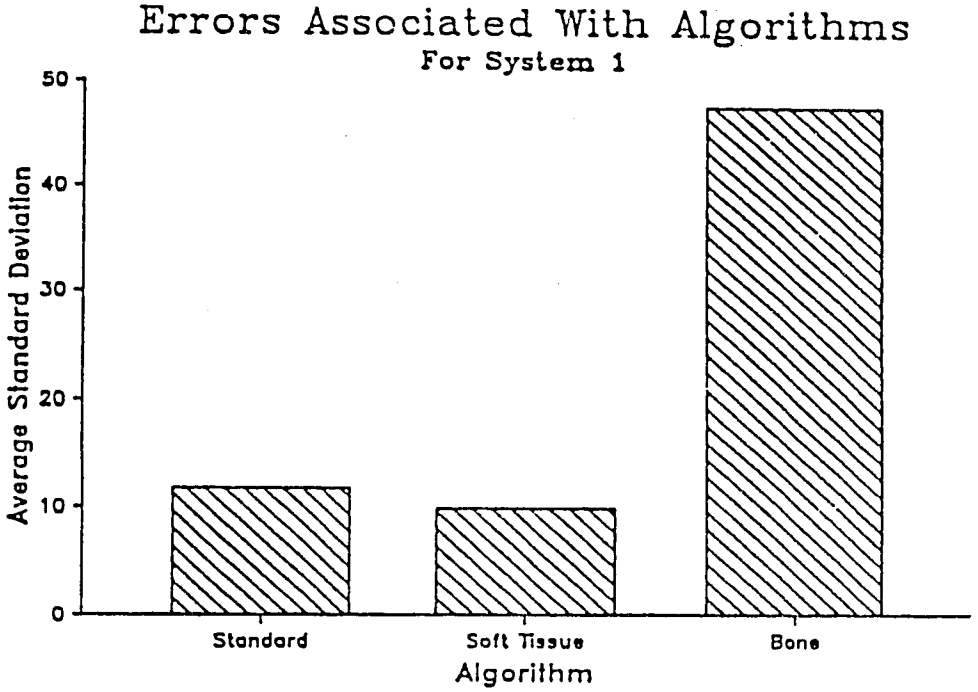

Fig. 73 Three reconstruction algorithms were studied for system 1. The choice of algorithm has a large effect on the results.

Figs 73-75 show a significant variation in the standard deviations between algorithms for each system.In Fig 74, 'sampling' refers to sampling rate, which is the number of projections that the system generates over the course of a scan. An increased sampling rate (1024) lead to an increase in standard deviation. This is because for constant mAs, doubling the sampling halved the mAs per intensity profile, and thus decreased the volume sampling.

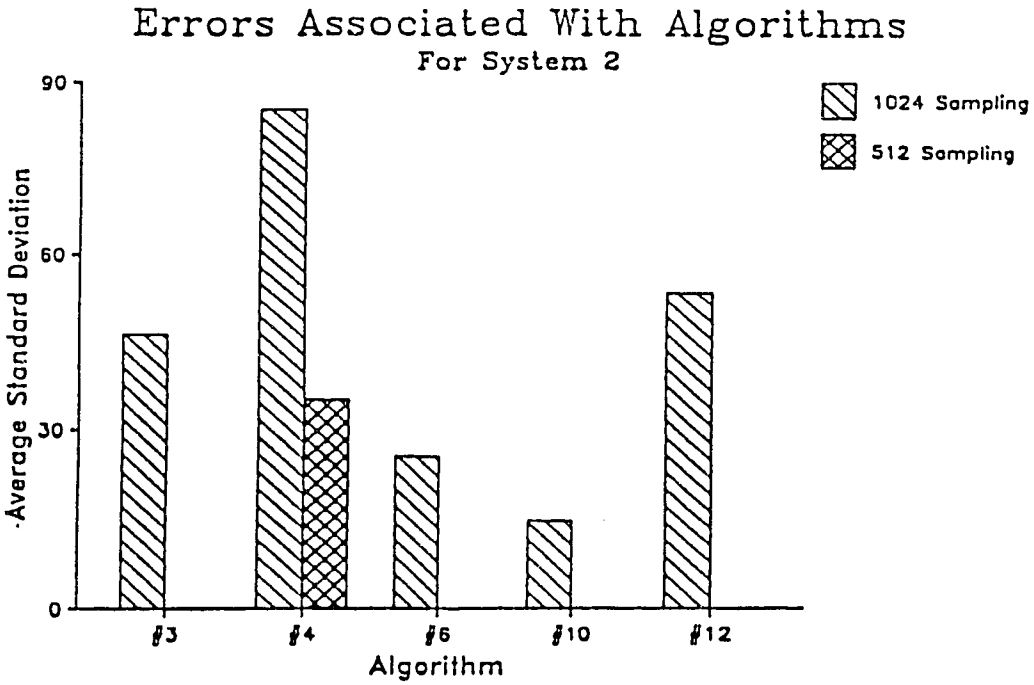

Fig. 74 Six algorithms were used with system 2. The names corresponding to the number are listed in Table 17.

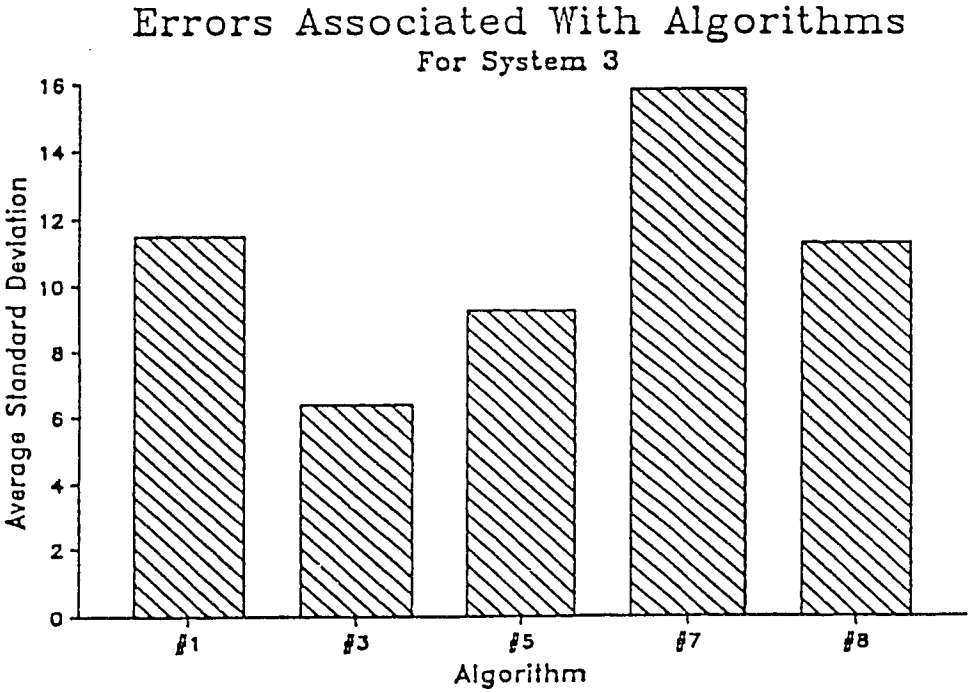

Fig. 75 Five algorithms from system 3 were tested for CT. Names corresponding to the numbers above are listed in Table 7.

4.2.6 Best case

Finally, all six of the cylindrical inserts were imaged using the optimal parameters, as determined by the above experiments, on each system. These parameters are listed in Table 18.

Table 18 Optimal Imaging Parameters for Each System

System	kVp	mAs	Slice Thickness	Algorithm
1	140	500	10 mm	Soft Tissue
2	140	480	10 mm	Adult Head (#10)
3	125	480	8 mm	Smoother Body (#3)

The results are shown in the graph in Fig 76. Note that although the slopes for the two systems are approximately the same, the standard deviations are significantly larger for system 2. As was mentioned previously, standard deviation seems to be the dominant measurement for detectability. Based on this graph then, we would expect the detectability to be worse for system 2. By taking the slopes of the two calibration lines and dividing them into the standard deviations of their respective measurements for each system, we can obtain the detectability of that system for each salt (Again, the *smaller* the detectability, the *better* the performance of the system). These values are shown in Table 19.

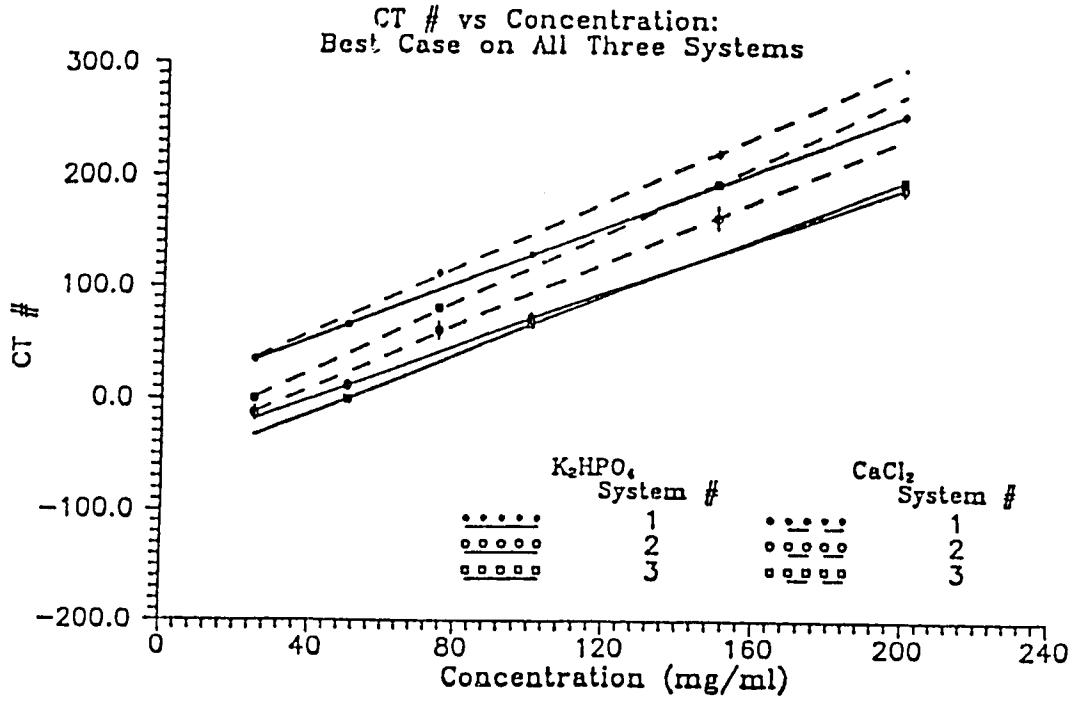

Fig. 76 The optimal calibration lines for all three CT systems.

Table 19 Detectability for Both Salts on Three Systems

System	Salt	Slope (CT#·ml/mg)	Standard Deviation (CT#)	Calcium Detectability (mg/ml)
1	K_2HPO_4	1.275	3.17	2.5
	$CaCl_2$	1.494	3.40	2.3
2	K_2HPO_4	1.200	5.43	4.5
	$CaCl_2$	1.421	8.13	5.7
3	K_2HPO_4	1.325	2.94	2.2
	$CaCl_2$	1.561	3.14	2.0

As one can see from Table 19, the calcium detectability for systems 1 and 3 is very good, $\leq$ 2.5 mg/ml. System 2 has a calcium detectability of $\approx$ 5.0 mg/ml, approximately twice that of the other two systems. It is interesting that K_2HPO_4 appears more detectable than

$CaCl_2$ with systems 1 and 3 but less detectable with system 2. The differences for systems 1 and 3 are small enough to essentially be ignored. That for system 2 can be explained by the fact that $CaCl_2$ is the more dense salt and will therefore cause increased beam hardening within the cylinder, increasing the standard deviation.

Even the 5.7 mg/ml detectability of $CaCl_2$ on system 2 is well below the critical level of 40 mg/ml, however. By comparison, analog radiology had a detectability of nearly 100 mg/ml. Thus the current use of CT is well justified for the quantification of calcium in SPNs.

4.2.7 CT System

One parameter that has not been explicitly treated as such up to this point is the CT system itself. Although the systems used here are generally comparable (none of them has cornered the market due to obviously superior performance) the above analysis shows that they clearly are not completely equivalent for all applications. Figure 77 shows the differences in the minimum detectable levels of calcium between the three systems.

Although all of these units would be adequate for Ca quantification in SPNs since they all have detectabilities well below the 40 mg/ml threshold, the factor of 2-3 separating systems 1 and 3 from system 2 make them preferable if a choice is available, since the better detectability corresponds to a smaller quantification error and better confidence. Where this difference might be even more significant is in current research in bone mineral content, where it is necessary to confidently measure very small changes in Ca density.

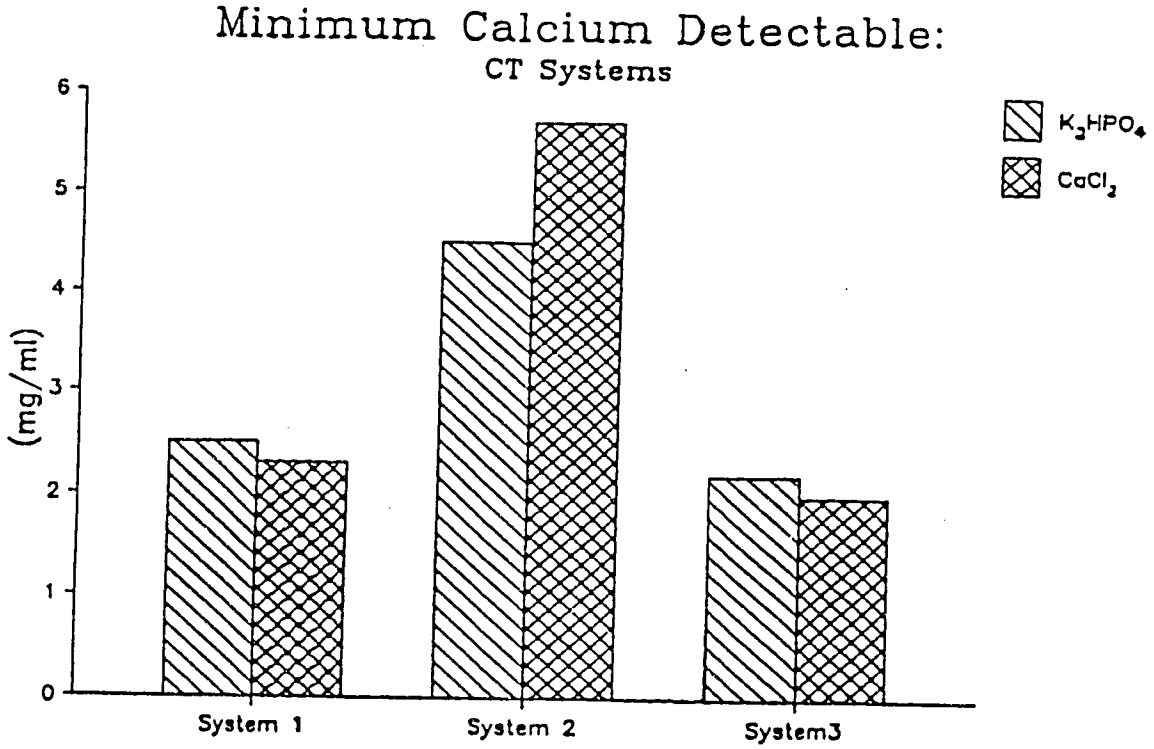

Fig. 77 The minimum acheivable error in Ca quantification for all three CT systems.

4.3 Theoretical Considerations

4.3.1 CT Error vs. Film-Screen Error

It was stated earlier that photon volume sampling is much greater for CT than for analog film radiology. One might ask why the volume sampling is not increased for analog radiology to bring it up to a CT equivalent level.

The reason can be explained in terms of three interconnected concepts. The first, detector efficiency, is given by the ratio of detected photons (Nd) to incident photons (Ni) for a detector. The second, the exposure range (R_E) of a detector, is the range of exposures (E & Ni) for which the detector responds linearly linear. The third, the intensity range (R_I) of a detector, is the range of

intensities (I & dNi/dt) over which its response is linear. When the measurement time must be t, the intensity range corresponds to an exposure range of:

(4.3.1) $$R_E' \propto R_I \cdot t$$

The lesser of R_E and R_E' will be the effective exposure range.

The detector efficiency relates the volume sampling (N_0) to the number of photons detected, using Equation (1.2.3) for N_i. From the proportionality of R_E and N_i there is therefore a relationship between the exposure range and the volume sampling. Likewise, (4.3.1) gives a relationship between the intensity range and volume sampling.

The detection efficiency of film-screen detectors is around 0.5 or 50%[22]. Thus, 1/2 of the volume sampling information is lost. The R_E of a typical film is 0.3 milliroentgens (mR) at 70 kVp[23]. At an imaging distance of 70 cm this corresponds roughly to a range of 1×10^{-2} mAs[24] for N_i.

R_E', the exposure range imposed by R_I, does not play a significant role for film-screen systems. The time taken for a phosphor molecule in the screen to emit its visible light is $\sim 10^{-8}$ s. Thus, more than 10^8 x-ray photons must strike each molecule in a screen each second in order to exceed R_I. This is a huge number. For a molecule with a 5 angstrom radius at a distance of 50 cm, the solid angle subtended is:

(4.3.2) $$(10^{-10})^2/4(10^{-1})^2 \simeq 10^{-19} \text{ steradians}$$

If every electron in the x-ray tube produced one x-ray photon, and these were dispersed isotropically and reached the detector, it would require approximately:

(4.3.3) $10^{19} \times 10^{8} = 10^{27}$ electrons/s $\simeq 10^{8}$ mA

Over an imaging time of 1 second this is a factor of 10^{10} times larger than the exposure range limitation calculated above. The limits on the volume sampling for a film-screen detector are therefore due to its exposure range rather than its intensity range.

There are two types of electronic CT detectors widely in use, scintillation crystals and high pressure xenon gas ionization chambers. Scintillation crystals are crystal lattices which emit visible light when interacting with ionizing radiation in a similar manner to an intensifying screen phosphor. The visible photons produced by a scintillator are converted into an electronic signal by a photocathode or a light sensitive diode. A photomultiplier tube (PMT) or electronic amplifier amplifies this electronic signal by approximately one million times which is then digitized and stored in a computer.

Gas chamber, or ionization chamber, detectors are containers filled with gas. Ionizing radiation interacting with the gas produces an ion/electron pair. An electric potential is applied between two electrodes within the chamber which pulls the ion pair apart. When each particle reaches its respective electrode a voltage signal is produced. This signal is subsequently amplified, digitized, and stored.

The detection efficiency of scintillators depends on the crystal used. The most popular scintillator at present is bismuth germanate ($Bi_4Ge_3O_{12}$). In the diagnostic energy range its detection efficiency is nearly 100%, primarily due to the large absorption cross section of bismuth (Z = 83).

The detection efficiency for gas detectors also varies. Xenon is the primary component of most gas combinations, and often pure xenon is used, because it has a relatively high absorption cross section compared to other gases. Even so, it is necessary to raise the pressure within the chamber considerably, to values of 5 to 25 atmospheres. With all this, the detection efficiency still is limited to 50 - 80%.

Neither of these types of detectors can store information, so instead pass photon counts on to a computer. The exposure range, therefore, is limited to the largest number that the computer is capable of handling. For practical purposes, however, $R_E = \infty$.

For gas chambers, R_I is limited by the time required for the conversion of an electronic pulse from analog to digital form, and by the rate at which these digitized pulses can be transferred to the computer. These are very quick processes, and in practice tube loading, patient dose and detection efficiency are the limiting factors for gas chambers.

For scintillation detectors, the intensity range is limited primarily by the decay time, the time which it takes for the crystal to return to its equilibrium state, which is typically in the range of 10^{-6} s. Also, an x-ray interaction may produce secondary modes of excitation which have forbidden transitions to equilibrium. These excited states release thermal energy to allow them into a state from which they can decay. Thus, the scintillation may persist for some time after excitation. This is known as afterglow. Sodium Iodide (NaI(Tl)), the most widely used scintillator in nuclear medicine, has such a secondary mode with a decay time of 0.15 s. This is the primary reason it isn't used in current CT scanners.

Bismuth germanate has virtually no afterglow and a decay time of 300 ns. Thus, nonlinearity of response occurs when photons arrive at intervals of << 0.3 μs, or rates >> 3.3 million photons/sec. For example, suppose a detector just starts to saturate at a photon fluence of 10^9 photons/sec, which is a typical value. A short scan would take about 1 second, so the total flux would be 1 billion photons. This may be converted to exposure by:

(4.3.4) $$\frac{E}{N_i} = (\mu_{en})_{air} \cdot \frac{\text{photon energy}}{54.8\text{x}10^6 \cdot A_d} \quad \frac{\text{roentgen}}{\text{photon}}$$ [25]

where: μ_{en} = the mass energy absorption coefficient in area/gm

A_d = the area of the detector

and photon energy is expressed in MeV.

Assuming an effective energy of 60 keV for a 100 kVp beam then the mass energy absorption cross section is $3.004\text{x}10^{-6}$ m^2/gm. The detector area will be taken as 4 mm x 25 mm. Thus (4.3.4) becomes:

(4.3.5) $$R_E = \Delta E = \frac{3.004\text{x}10^{-6} \cdot 0.06 \cdot 1\text{x}10^9}{54.8\text{x}10^6 \cdot 1\text{x}10^{-4}} \text{ roentgen}$$

$$= 0.34 \text{ R}$$

This is a factor of a thousand greater than the exposure range stated above for a film-screen combination. Thus the photon volume sampling can be much higher for the scintillation detector. If we detect the same contrast range using CT and film-screen detectors, the detectability of CT will be better because there will be a lower statistical error associated with the sampling process.

The results in chapter 2 show that the error due to the statistics of volume sampling for film-screen combinations is negligible compared to other statistical and systematic errors. The

discussion above demonstrates that even if other sources of quantification error could be eliminated, the photon counting ability of film-screen detectors is inherently lower than for electronic detectors.

4.3.2 Relationship Between Volume Sampling and Standard Deviation

As was discussed above, the detectability of Ca for CT scanners is primarily limited by the error, or standard deviation (s), of the measurement. This is a region of interest (ROI) standard deviation (s_{ROI}). Up until now, the sampling density and s_{ROI} have been assumed to be related. Proof of the validity of this assumption will now be given.

The ROI standard deviation for p pixels with standard deviations $\{s_p\}$ is given by:

$$(4.3.6) \qquad s_{ROI}^2 = \sum_p (s_p^2)$$

if the ROI has uniform density. The number of photons in each ray (N_r) which contribute to a given pixel varies randomly (as well as systematically). This random variation has a Poisson distribution, and thus, the standard deviation per ray (s_r) is:

$$(4.3.7) \qquad s_r = \sqrt{N_r}$$

Since the error in each ray is independent the total error for a given pixel is:

$$(4.3.8) \qquad s_p^2 = \sum_r (s_r^2)$$

Combining (4.3.6), (4.3.7), and (4.3.8) gives:

(4.3.9) $s_{ROI}^2 = \Sigma(N_r)$ for all rays contributing to the ROI.

Of course, N_r is proportional to N_d, which completes the proof. N_d is related to N_r by the detection efficiency so the greater the detection efficiency the smaller the standard deviation.

There is another component that adds to the standard deviation - electronic noise. The contribution of electronic noise to the standard deviation is determined by the conversion efficiency of a detector. This is the percentage of the energy of a detected photon that is converted into an electronic signal. If the conversion efficiency is low, the signal to noise ratio will be reduced, and the random component of the detector signal will increase, leading to an increase in the standard deviation within the pixels.

Thus, although the detection efficiency of xenon detectors is considerably lower than that of scintillation detectors, this is balanced by the fact that BGO has a conversion efficiency of only about 1 - 2%. The result is that both types of detectors generally perform similarly under conditions used in CT scanning.

4.3.3 Slice Thickness and Nodule Size

Earlier it was stated that the operator is not necessarily free to choose the thickness of the slice for a scan of an SPN. A CT image reduces a three dimensional volume element (voxel) to a two dimensional area element (pixel). When objects of different densities are included in the same voxel, their densities are averaged.

This rarely happens in the image or radial plane because the dimensions of the voxel in this plane are so small (1 mm or less per side). However, for a 10 mm thick slice, there is sufficient distance in the axial direction to have significant changes in density in the same voxel. This averaging of densities for a thick slice is called the partial volume effect. If enough non-SPN tissue volume is included in the pixels representing the nodule, the values that we obtain for calcification will not, therefore, be accurate.

This contribution of non-SPN tissues to the mean pixel value in a region of interest is called the partial volume fraction (PVF). It is possible to reasonably accurately calculate the partial volume fraction for SPNs. Let us assume that the nodule is a sphere of radius r_s. We wish to know the portion of the volume of a right circular cylinder of radius r_c (the radius of the circular ROI) and depth t (the slice thickness) which corresponds to sphere volume if they are arrange concentrically (see Fig 78). The volume of the sphere is given by:

$$V_s = (4/3)\pi r_s^3 \qquad (4.3.10)$$

while for the cylinder:

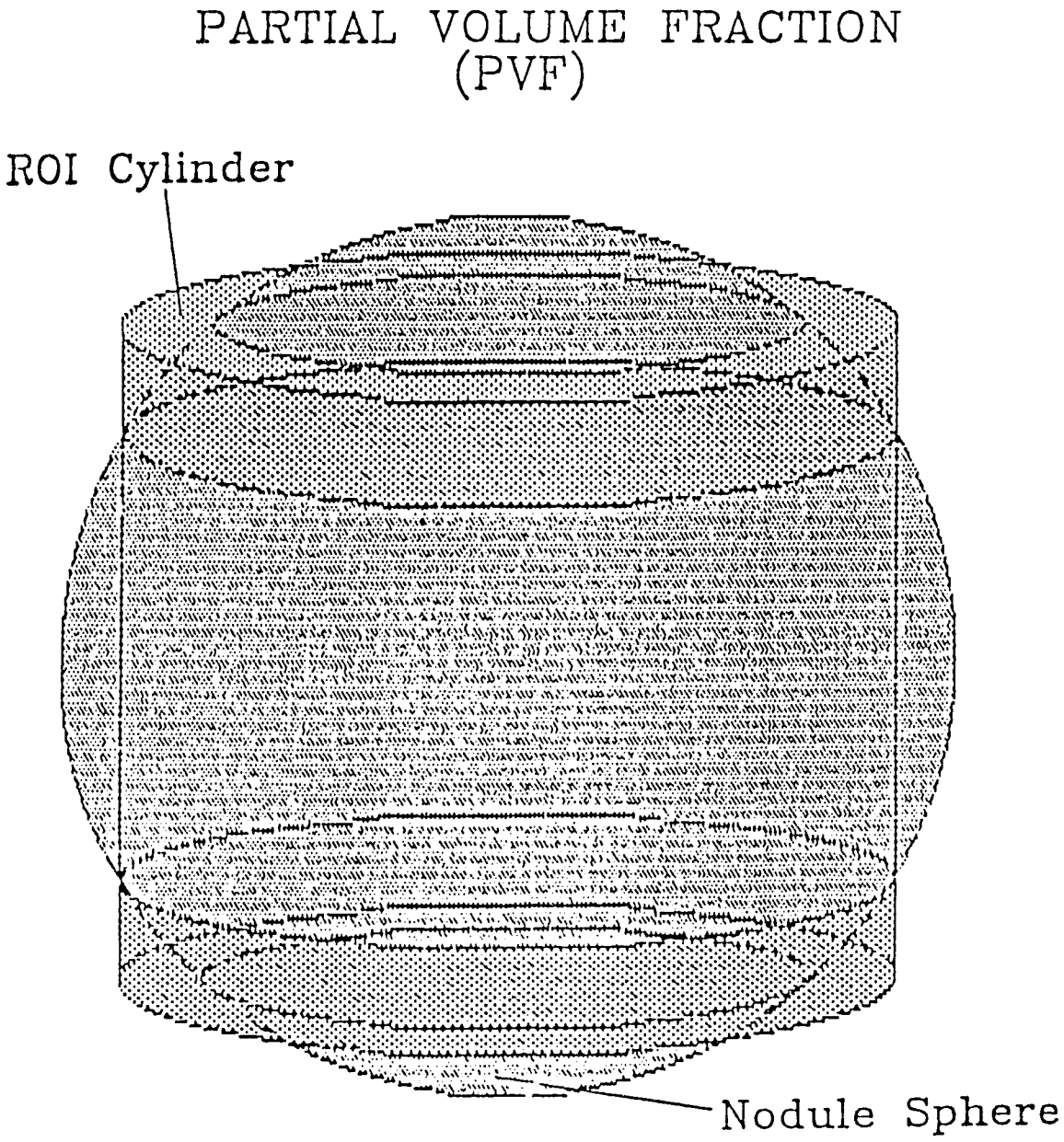

Fig. 78 The portion of the cylinder not filled with sphere is the partial volume fraction (PVF).

(4.3.11) $$V_c = \pi r_c^2 t$$

The partial volume fraction is defined as the percentage of the circular region of interest, represented by the cylinder, which is occupied by objects other than the SPN, which is represented by the sphere. By specifying an upper limit on the PVF, one can obtain a functional relationship between r_c, t, and r_s by:

(4.3.12) $$(1\text{-PVF}) \cdot 3r_c^2 t = 4r_s^3$$

The solution to this equation is a set of surfaces for given values of r_s.

At this point the question of an allowable PVF must be answered. One would like to choose a PVF that contributes no more error to the measurement than already exists from the standard deviation, say 3.4 CT# ($CaCl_2$ on system 1, see Table 19). If the CT# for the substance occupying the non-SPN volume of the cylinder (PVFCT#) and that of the nodule (SPNCT#) are known, the required PVF is simply:

(4.3.13) $$\text{PVF} \leq 3.4/(\text{SPNCT\#}-\text{PVFCT\#})$$

The most likely candidates to fill the PVF are lung and soft tissue. Lung has an average ideal CT# of approximately -800[26], while soft tissue can be considered 0 for most purposes. For a nodule at the critical level, 40 mg/ml, the SPNCT# would be approximately 60 ($CaCl_2$ on system2, see Table 19). Thus the PVFs for lung and tissue would be:

(4.3.14.a) $$\text{PVF}_L(40\text{ mg/ml}) = 3.4/(60 + 800) = 5\text{x}10^{-3}$$

(4.3.14.b) $$\text{PVF}_T(40\text{ mg/ml}) = 3.4/(60 - 0) = 5.7\text{x}10^{-2}$$

Using this system a PVF can be calculated to produce a desired accuracy for any concentration of calcification in an SPN.

Once a PVF has been determined, the slice thickness and ROI radius for a given nodule of known size can be calculated as per (4.3.13). Values of r_c (ROI radius) as a function of r_s (nodule radius) for various slice thickness based on a $5x10^{-3}$ PVF (40 mg/ml Ca, 3.4 CT# error) are shown in Fig 79. Where values of r_c exceeded r_s they were made equal.

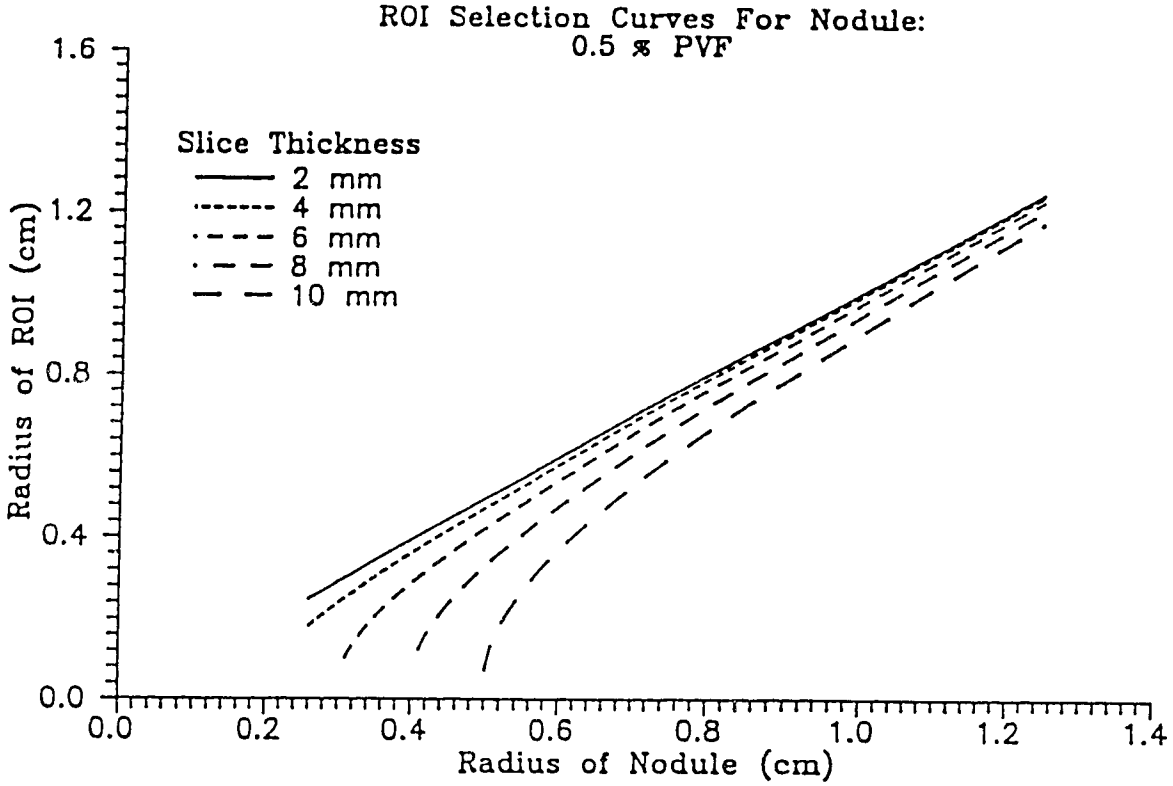

Fig. 79 Theoretical 0.5% PVF curves based on circular region of interest and spherical nodule.

Since one does not know the calcification of the nodule before scanning, a rule of thumb is to choose t to be r_s[10]. This, then, is the restriction placed on the slice thickness by geometry. One must balance

the effect of volume sampling on standard deviation with partial volume fractions to find the optimal slice thickness.

4.4 Summary

In this chapter, the use of CT scanners for Ca quantification has been explored. Three systems were used for experiments. Imaging parameters for these systems were systematically varied in order to find the optimal parameters for quantification. These parameters were: kVp, mAs, slice thickness, thickness of the surrounding absorber (chest wall thickness), and reconstruction algorithm.

KVp experiments were surprising in that the best detectability was given at higher kVps due to decreased noise. Since increasing kVp decreases dose to the patient, this is a very favorable situation.

mAs, slice thickness, and wall thickness all affected quantification according to a simple rule: increasing the object volume sampling (# of photons traversing a given volume) decreased the standard deviation, and thus the error in quantification. Anomalous slice thickness results for system 3 suggest that the collimation may not be behaving as expected on this system.

Algorithm selection proved to be crucial to reducing the error in quantification, and widely varying results could be obtained on the same system using different algorithms. New algorithms might possibly provide further decreases in quantitative error.

When all parameters had been studied, a combination of the best parameters was used to obtain the minimum detectable calcification for

each system. The results showed that system 1 and 3 performed similarly while system 2 had approximately twice the error of its two counterparts. However, the significance of this fact based on trials over only three systems is questionable.

Regardless of the differences between systems, the 2.0 to 5.7 mg/ml Ca detectability range is well within the 40 mg/ml threshold set for benignancy, and in this regard the use of CT for quantification is far better than analog radiography. Theoretical reasons for this discrepancy were explored in section 4.3 of this chapter.

A theoretical discussion of the dependency of quantitation error due to partial volume fractions was also given in section 4.3. This explored the relationship between the nodule geometry, the ROI radius, and the slice thickness as they pertain to partial volume errors. A theoretical justification for Zerhouni's rule of thumb that the slice thickness should be less than the SPN radius was given.

In conclusion, CT provides excellent quantification abilities for calcium in SPNs, and this work can be extended beyond that to bone mineral analysis and other calcium and light element quantification procedures. The current method of scanning one or more reference or calibration phantoms immediately following patient scans is time consuming and rather complicated by comparison to the methods proposed for analog and digital radiography, but there seems little choice if one wishes to have sufficient quantification accuracy. Unfortunately, beam hardening does not allow calibration phantoms to be scanned simultaneously with the patient without introducing errors. Longitudinal drift in the equipment does not allow calibration lines to be used over more than a few scans.

System differences make meaningful intersystem comparisons very difficult. Nonetheless, there are few radiological systems that can compare to CT for quantitative capabilities.

Chapter 5 : Applications

5.1 Techniques

In this thesis, the ability of three different imaging modalities to quantify calcium in SPNs has been investigated. The application of these to actual clinical use has yet to be discussed. In this chapter, an attempt to relate this research to practical situations will be made.

As was discussed in the CT section, there is little improvement to quantitative CT to be made to the current method of scanning a patient and then scanning a phantom with a simulated nodule. A comparison of the patient nodule to the calibrated nodule can be made and benignancy determined. This method is time consuming and complicated, and the tissue equivalent phantoms used are fairly costly, but beam hardening and scanner performance drift make other methods unfeasible.

The most significant factor here is one of the most imposing aspects of light element quantification: small changes in light element content produce very small changes in attenuation. This means that the contrast detection capabilities of a system must be optimized in every conceivable way. There is little room for loss of sensitivity.

For CT this involves maximizing kVp, mAs, and slice thickness (to the extent outlined in chapter 3). Reconstruction algorithms for a given system should be evaluated to determine which produces the least noise (standard deviation). This can be done simply by reconstructing the same image with different algorithms and measuring the standard

deviation from the same region of interest in a homogeneous phantom.Two radiographic methods, analog and digital, were studied in order to provide less expensive, quicker, and easier methods of quantification. The ring phantom could be used to provide reference values for calcification in the same image as the nodule. Since it is just plastic and calcium, it would likely be less expensive than phantoms currently used in CT. These modalities would also lower patient dose as compared with CT.

Neither radiographic modality has been thoroughly studied. IIDR can be investigated properly once a unit with direct access to the numeric data is available. For AR and SPDR, experiments for this project have been done with uniform tissue contribution (the water blocks). This would not be the case for a patient, and dual energy subtraction would probably be necessary to eliminate tissue nonuniformity.

This would require two separate images, doubling the error, and would introduce another process, dual energy subtraction, which would add further errors. If radiographs at both energies could be taken simultaneously then there would be no misalignment of images. Otherwise, alignment artifacts are likely and would also contribute to the error. Finally, the ring phantom would be placed outside the patient while the nodule was within. This would lead to a beam hardening error. The magnitude of these errors is uncertain as yet, and they may make radiographic quantification impossible.

For example, a dual energy imaging cassette was mentioned in chapter 1 as being a possible method of obtaining analog radiographs simultaneously and thus eliminating patient movement artifacts.

Unfortunately, our work on analog radiography has already ruled out its usefulness at the low concentrations of Ca we are interested in.

SPDR does show promise, and it is possible that the method used by the Birmingham group (parallelogram region of interest, discussed briefly in chapter 1) may be feasible for use with SPDR on a CT unit. Furthermore, for the Birmingham method, dual energy subtraction might not be necessary, as tissue contributions over the small areas involved might not vary significantly. One must decide with this method, however, how to obtain a calibration line of known reference values.

In short, there is still much work to be done in the possible use of SPDR with CT scanners to quantify calcification in SPNs. Of the three CT systems available for this research, only one provided features that might allow quantification with the present software. Thus, to continue investigation, it is likely that manufacturers would have to take an interest in the non-tomographic uses of their scanners. The fact that much of the work here might also be used as a basis for bone mineral analysis might help in this regard.

A ring phantom could also be used with SPDR. This would provide a reference in the nodule image. However, this would certainly require dual energy subtraction. A hybrid technique using both the Birmingham method and ring phantom might also be useful. Rib overlaying the nodule would be eliminated by defining a parallelogram and subtracting the base level density (corresponding to the overlaid rib) as the Birmingham group had done. The resultant density could then be compared to the unobscured portions of the rings to determine the Ca level.

5.2 Phantom Design

Throughout this thesis, phantoms from previous research have been discussed and new phantoms designed and built. In this section we will discuss the effect of phantom design on quantification.

Various calcium salts suspended in different media have been used by other researchers to simulate calcified pulmonary nodules. Zerhouni et al used hydrous calcium chloride ($CaCl_2 \cdot H_2O$) dissolved in distilled water[4]. The same group designed a prototype phantom package for use in determining benignancy in SPNs[10]. For this phantom they used calcium carbonate ($CaCO_3$) suspended in tissue equivalent epoxy resin. Hickey et al in their SPDR study used calcium hydroxide ($Ca(OH)_2$) suspended in some sort of wax[2]. Kruger et al. used calcium hydrogen phosphate ($CaHPO_4$) powder for their analog radiography studies and potassium hydrogen phosphate (K_2HPO_4) for a CT comparison[3].

This is the same potassium salt used in the commercial phantom used in our CT studies, although no mention is made of the solvent or suspending agent for this phantom in the accompanying literature. Tribasic calcium phosphate $Ca_3(HPO_4)_2$ (apatite) was suspended in petroleum jelly for the ring phantom. Later dibasic calcium phosphate $Ca_2(HPO_4)_2$ was suspended in paraffin in the ring phantom, but this was never used. The cell phantom and the cylinders supplied for the CT phantom both used hydrous calcium chloride ($CaCl_2 \cdot H_2O$) dissolved in water.

Although there appears to be no literature to support this, it is likely that hydroxyapatite $Ca_3(PO_4)_2 \cdot Ca(OH)_2$ is the calcium salt with which nodules become calcified. A comparison of the theoretical values

of the linear attenuation cross sections of some of these salts is shown in Fig 80.

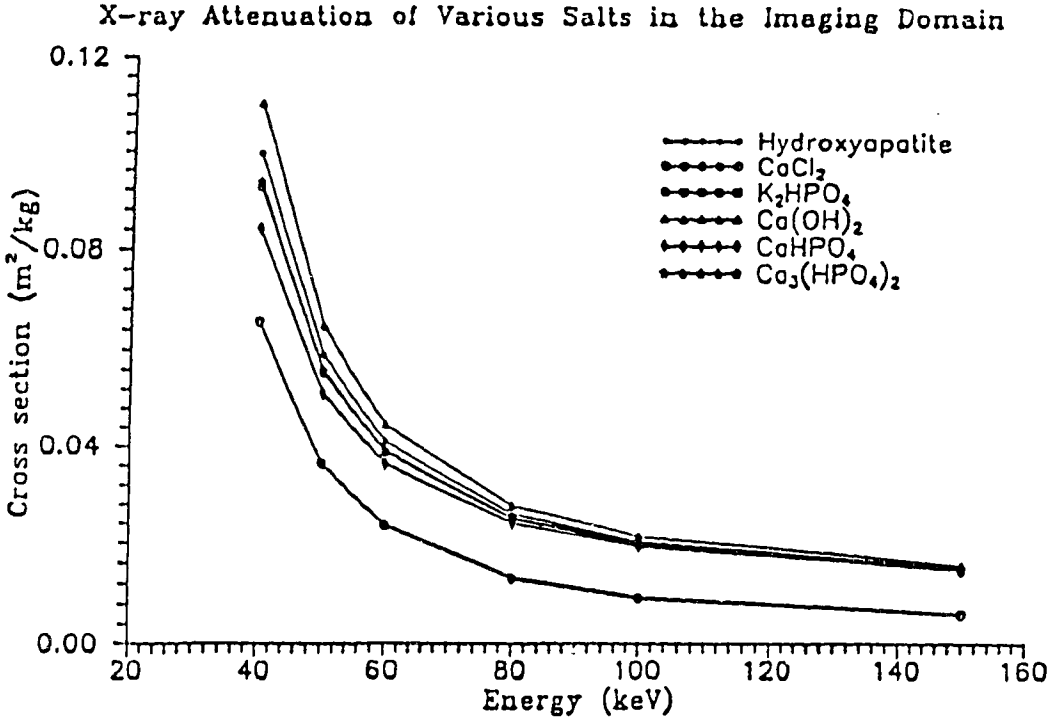

Fig. 80 Attenuation cross sections calculated theoretically from Hubbel's data.

It is interesting in light of this graph that although the attenuation cross section of K_2HPO_4 is greater than that of $CaCl_2$, the latter showed greater attenuation in CT experiments (see Fig 80). This is likely due to the fact that the $CaCl_2 \cdot H_2O$ used was claimed on the label to be about 27% water, and thus the concentrations were adjusted accordingly. This compound came from a reclamation project, and thus the label may have been in error.

It also bears mentioning at this point that there were substantial problems with suspending calcium salts in both petroleum jelly and paraffin. The predominant problem was air bubbles in the suspension which considerably altered the attenuation properties. With

paraffin, settling also occurred so that the Ca distribution was not uniform.

Even the trivial task of weighing the calcium salt was difficult when such small quantities were necessary for the low concentrations used. This applied to all the phantoms made. On a scale that measured to the nearest 0.1 mg, it became clear that a single crystal or grain of salt often weighed of the order of a mg. Thus, there are errors involved in transference of the salt from scale to solution.

To summarize, one must deal with extremely low concentrations of calcium or potassium salts in simulating calcification in SPNs. The same would be true for bone mineral analysis. This means that normally negligible effects such as settling, micro-bubbles, and even the salt used, may contribute significantly to experimental results.
It is therefore suggested that the utmost care be taken in the preparation of phantoms for quantification of low levels of light elements. Solutions are the easiest method of producing fairly reliable concentrations. It would be of great value if the composition of commercial phantoms would be provided as part of the package. Knowledge of the accuracy of the phantom would allow a better estimate of the accuracy of the quantification procedure.

Chapter 6 : Conclusion and Summary

This work has investigated the capabilities of three imaging modalities to quantify calcium in solitary pulmonary nodules. The three modalities are: analog radiography, digital radiography, and computed tomography. It would be useful to obtain quantitative estimates of calcification in SPNs because sufficient calcification is one of two radiological indicators of benignancy. If radiological criteria are unavailable, thoracotomy is often used.

Largely because of the work of a group at Johns Hopkins University in the early 1980s, a method for quantitating Ca in SPNs was developed. This method used a threshold calcification of 40 mg/ml for benignancy. Commercial CT packages based on this work are now available. However, CT quantitation is time consuming, expensive, and relatively complicated. Also, the dose from CT scans can be large. A radiographic method of quantifying Ca in SPNs would be useful if it was simpler, less costly, and quick. The dose for chest radiographs is typically lower than that for CT scans.

The investigations into analog radiography showed that exposure nonuniformity over the film field due to the inherent distribution of radiation from an x-ray tube was troublesome. Although various methods were devised to eliminate this field non-uniformity, the most effective still produced an error of 0.064 optical density units if the statistical error is taken to be two standard deviations. This compares to an optical density of 0.023 OD units for 40 mg/cm^2 Ca. Kruger et al found that dual energy subtraction could be expected to add another

0.07 OD error. The use of analog radiography for quantitation thus appears unfeasible.

Computed tomography is currently the most popular modality for quantification of Ca in SPNs. Three systems were tested. All three proved capable of detecting Ca concentrations of less than 6 mg/ml, well below the threshold value of 40 mg/ml. It should be noted that different salts to simulate Ca content gave different results. Finally, while two systems performed similarly, one was significantly worse.This implies that all CT scanners do not perform equally in terms of quantitative capabilities.

Two methods of digital radiography were explored. Investigations into DR with a DSA unit did not provide direct numeric data. Since film data was already shown to have limited value, investigation was terminated into this method of DR.

Scan projected digital radiography had already proved useful for past research on a prototype unit[2]. The possibility of using CT scanners for SPDR was investigated and found feasible. Only two of the three CT units had software to give numeric data from digital radiographs. One of these two reconstructed the data using unknown algorithms which compromised its linearity. The remaining unit had the capability to distinguish as little as 7.8 mg/cm^2 of calcium. However, other processes like dual energy subtraction would be necessary before this method could be used clinically. The error due to these processes remains to be investigated.

The final results of all the above procedures are shown in Fig 84. The horizontal line represents the 40 mg/ml Ca threshold for benignancy. The details of clinical use such as exact method, dose, and

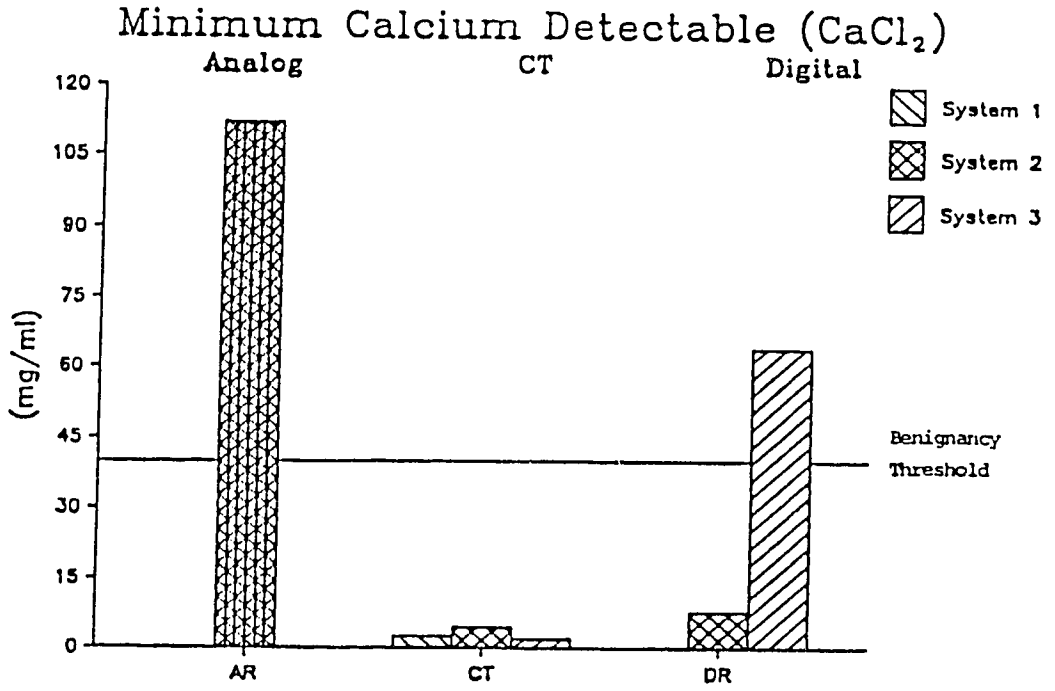

Fig. 81 Digital radiography shows potential as an alternative to CT. Analog radiography is no feasible for Ca quantification for SPNs.

design of phantom have yet to be worked out, although some of the work presented herein suggests possible avenues of development. Although there is practically no hope of using analog radiography as a substitute for CT quantitation, digital radiography promises an adequate replacement. With some software modification, an SPDR method might be developed for CT scanners, providing a quicker, easier, and less expensive method of calcium quantification with less patient dose and the same availability as CT methods currently in use.

FOOTNOTES

1 Siegalman et al., 'CT of the Solitary Pulmonary Nodule', AJR 135: 1-13, July 1980.

2 Hickey et al., 'Dual-Energy Digital Radiographic Quantification of Calcium in Simulated Pulmonary Nodules',AJR 148: 19-24, January 1987.

3 Kruger et al., 'Dual Energy Film Subtraction Technique for Detecting Calcification in Solitary Pulmonary Nodules', Radiology 140: 213-219, July 1981.

4 Zerhouni et al., 'Factors Influencing Quantitative CT Measurements of Solitary Pulmonary Nodules', Journal of Computer Assisted Tomography 6(6): 1075-1087, Dec. 1982.

5 Godwin et al., 'Distinguishing Benign from Malignant Pulmonary Nodules by Computed Tomography', Radiology 144: 349-351, July 1982.

6 Levi et al., 'The Unreliability of CT Numbers as Absolute Values', AJR 139: 443-447, Sept. 1982.

7 Zerhouni et al., 'A Standard Phantom for Quantitative Analysis of Pulmonary Nodules', Radiology 149: 767-773, Dec. 1983.

8 Tesic et al., 'Digital Radiography of the Chest: Design Feature and Considerations for a Prototype Unit', Radiology 148: 259-264, July 1983.

9 Tesic et al., 'Single-Slit Digital Radiography, Some Practical Considerations', AJR 142: 697-702, April 1984.

10 Fraser et al., 'Digital Radiography of the Chest: Clinical Experience with a Prototype Unit', Radiology 148: 1-5, July 1983.

11 Fraser et al., 'Calcification in Pulmonary Nodules: Detection with Dual-Energy Radiography', Radiology 160: 595-601, 1986.

12 Niklason et al., 'Simulated Pulmonary Nodules: Detection with Dual-Energy Digital versus Conventional Radiography', Radiology 160: 589-593, 1986.

13 Speller et al., 'A System for Dual-Energy Radiography', The British Journal of Radiology 56: 461-465, 1983.

14 Shaw and Plewes, 'Effects of Scattered Radiation and Veiling Glare in Dual-Energy Tissue-Bone Imaging: A Theoretical Analysis', Medical Physics, 14(6): 956-967, 1987.

15 Kruger, 'Dual-Energy Scanning-Slit Fluorography for the Determination of Vertebral Bone Mineral Content', Medical Physics 14(4): 562-566, 1987.

16 Katragaada et al., 'Digital Radiography Using a Computed Tomographic Instrument', Radiology 133: 83-87, Oct. 1979.

17 c.f. Evans The Atomic Nucleus, Chapter 20, McGraw-Hill inc., 1955.

18 Jackson, Classical Electrodynamics, Chapter 15, John Wiley & Sons inc., 1962.

19 Ibid. pp.364-365.

20 c.f. Evans, The Atomic Nucleus, Table 2.1.,p.608, McGraw-Hill inc., 1955.

21 Seltzer and Berger, Int. J. Appl. Radiat. Isot. Vol. 33, pp. 1189 - 1218, 1982.

22 Curry, Dowdey, & Murry, Christensen's Introduction to the Physics of Diagnostic Radiology, 3rd Ed., p. 115. Lea & Febiger publ., 1984.

23 Dupont handout PB2-D-7.0 5/81.

FOOTNOTES (cont.)

24 Curry, Dowdey, & Murry, Christensen's Introduction to the Physics of Diagnostic Radiology, 3rd Ed., p 408. Lea & Febiger publ., 1984.
25 Johns, The Physics of Radiology, 2nd Ed., p. 444. Charles C Thomas publ., 1961.
26 Fullerton, 'Fundamentals of CT Tissue Characterization', from Medical Physics of CT and Ultrasound: Tissue Imaging and Characterization, Fullerton & Zagzebski ed.s, AAPM, 1980.

BIBLIOGRAPHY

Bloch,R.G, 'Tuberculous Calcification. A Clinical and Experimental Study', AJR 59, 853-864, 1948.

O'Keefe,M.E., Good,C.A., McDonald,J.R., 'Calcification in Solitary Nodules of the Lung', AJR 77, 1023-1033, 1957.

Good,C.A, McDonald,J.R., 'Roentgenologic Evidence of Calcification in a Peripheral Bronchogenic Carcinoma', Mayo Clin. Proc. 31, 317-321, 1956.

Siegalman,S.S., Zerhouni,E.A., Leo,F.P., Khouri,N.F., Stitik,F.P., 'CT of the Solitary Pulmonary Nodule', AJR 135, 1-13, July 1980.

Godwin,J.D., Speckman,J.M., Fram,E.K., Johnson,G.A, Putman,C.E., Korobkin,M, Brieman,R.S, 'Distinguishing Benign from Malignant Pulmonary Nodules by Computed Tomography', Radiology 144, 349-351, July 1982.

Levi,C, Gray,J.E., McCullough,E.C., Hattery,R.R., 'The Unreliability of CT Numbers as Absolute Values', AJR 139, 443-447, Sept. 1982.

Zerhouni,E.A., Spivey,J.F., Morgan,R.H., Leo,F.P., Stitik,F.P., Siegelman,S.S., 'Factors Influencing Quantitative CT Measurements of Solitary Pulmonary Nodules', Journal of Computer Assisted Tomography 6(6), 1075-1087, Dec. 1982.

McCullough,E.C., Morin,R.L., 'CT-Number Variability in Thoracic Geometry',AJR 141, 135-140, 1983.

Zerhouni,E.A., Boukadoum,M, Siddiky,M.A., Newbold,J.M., Stone,D.C., Shirey,M.P., Spivey,J.F., Hesselman,C.W., Leo,F.P., Stitik,F.P., Siegelman,S.S., 'A Standard Phantom for Quantitative Analysis of Pulmonary Nodules', Radiology 149, 767-773, Dec. 1983.

Siegelman,S.S., Khouri,N.F., Scott,W.W.,Jr., Leo,F.P., Zerhouni,E.A., 'Computed Tomography of the Solitary Pulmonary Nodule', Seminars in Roentgenology XIX(3), 1984.

Siegelman,S.S., Khouri,N.F., Leo,F.P., Fishman,E.K., Braverman,R.M., Zerhouni,E.A., 'Solitary Pulmonary Nodules: CT Assesment', Radiology 160, 307-312,1986.

Zerhouni,E.A., Stitik,F.P., Siegelman,S.S., Naidich,D.P., Sagel,S.S., Proto,A.V., Muhm,J.R., Walsh,J.W., Martinez,C.R., Heelan,R.T., Brantley,P, Boxeman,R.E., Disantis,D.J., Ettenger,N, McCauley,D, Aughenbaugh,G.L., Brown,L.R., Miller,W.E., Litt,A.W., Leo,F.P., Fishman,E.K., Khouri,N.F., 'CT of the Pulmonary Nodule: A Cooperative Study', Radiology 160, 319-327, 1986.

BIBLIOGRAPHY (cont.)

Kruger,R.A., Armstrong,J.D., Sorenson,J.A., Niklason,L.T, 'Dual Energy Film Subtraction Technique for Detecting Calcification in Solitary Pulmonary Nodules', Radiology 140, 213-219, July 1981.

Speller,R.D., Ensell,G.J., 'A System for Dual-Energy Radiography', The British Journal of Radiology 56, 461-465, 1983.

Shaw,C, Plewes,D.B., 'Effects of Scattered Radiation and Veiling Glare in Dual-Energy Tissue-Bone Imaging: A Theoretical Analysis', Medical Physics, 14(6), 956-967, 1987.

Kruger,R.A., 'Dual-Energy Scanning-Slit Fluorography for the Determination of Vertebral Bone Mineral Content', Medical Physics 14(4), 562-566, 1987.

Tesic,M.M., Mattson,R.A., Barnes,G.T., Sones, R.A., Stickney,J.B., 'Digital Radiography of the Chest: Design Feature and Considerations for a Prototype Unit', Radiology 148, 259-264, July 1983.

Fraser,R.G., Breatnach,E., Barnes,G.T., 'Digital Radiography of the Chest: Clinical Experience with a Prototype Unit', Radiology 148, 1-5, July 1983.

Tesic,M.M., Sones,R.A., Morgan, D.R., 'Single-Slit Digital Radiography, Some Practical Considerations', AJR 142, 697-702, April 1984.

Fraser,R.G., Hickey,N.M., Niklason,L.T., Sabbagh,E.A., Luna,R.F., Alexander,C.B., Robinson,C.A., Katzenstein,A.A. Barnes,G.T., 'Calcification in Pulmonary Nodules: Detection with Dual-Energy Radiography', Radiology 160, 595-601, 1986.

Niklason,L.T., Hickey,N.M., Chakraborty,D.D., Sabbagh,E.A., Yester,M.V., Fraser,R.G., Barnes,G.T., 'Simulated Pulmonary Nodules: Detection with Dual-Energy Digital versus Conventional Radiography', Radiology 160, 589-593, 1986.

Morgan,D.R., Sones,R.A., Barnes,G.T., 'Performance Characteristics of a Dual Energy Detector for Digital Scan Projected Radiography' Medical Physics 14(5), 728-735, 1987.

Hickey,N.M., Niklason,L.T., Sabbagh,E., Fraser,R.G., Barnes,G.T., 'Dual-Energy Digital Radiographic Quantification of Calcium in Simulated Pulmonary Nodules',AJR 148, 19-24, January 1987.

Katragaada,C.S., Fogel,S.R., Cohen,G., Wagner,L.K., Morgan,C.,III, Handel,S.F., Amtey,S.R., Lester.R.G., 'Digital Radiography Using a Computed Tomographic Instrument', Radiology 133, 83-87, Oct. 1979.

BIBLIOGRAPHY (cont.)

Johns,H.E., Battista,J., Bronskill,M.J., Brooks,R., Fenster,A., Yaffe,M., 'Physics of Ct Scanners: Principles and Problems' Int J Radiation Oncology Biol Phys 3, 45-51, 1977.

Haus,A.G., (Ed.), The Physics of Medical Imaging: Recording System Measurements and Techniques, AAPM, New York, 1979.

Marshall,C., (Ed.), The Physical Basis of Computed Tomography, Warren H. Green, inc., St Louis, 1982.

Fullerton,G.D., Zagzebski,J.A., (Ed.s), 'Fundamentals of CT Tissue Characterization', from Medical Physics of CT and Ultrasound: Tissue Imaging and Characterization, Fullerton & Zagzebski ed.s, AAPM, New York, 1980.

Hendee,E., William,R., The Physical Principles of Computed Tomography, Brown and Company, Toronto, 1983.

Seltzer,S.M., Berger,M.J., Int. J. Appl. Radiat. Isot. Vol. 33, pp. 1189 - 1218, 1982.

Pratt,R.H., Tseng,H.K., Lee,C.M., Kissel,L.,MacCallum,C., Riley,M., 'Bremsstrahlung Energy Spectra from Electrons of Kinetic Energy 1keV $\leq T_1 \leq$ 200 keV Incident on Neutral Atoms $2 \leq Z \leq 92$', ADNDT 20, 175, 1977. Erratum: 26, 477.

Kissel,L., Quarles,C.A., Pratt,R.H., 'Shape Functions for Atomic-Field Bremsstrahlung from Electrons of kinetic energy 1-500 keV on Selected Neutral Atoms $1 \leq Z \leq 92$', ADNDT 28, 381, 1983.

Nordell,B., Brhme,A., 'Angular Distribution of Yield from Bremsstrahlung Targets', Phys Med Biol 29(7), 797-810, 1984.

Hubbel,J.H., 'Photon Mass Attenuation and Energy Absorption Coefficients from 1 keV to 20 MeV', Int J Appl Radiat Isot 33, 1269-1290, 1982.

Hubbel,J.H., 'Photon Crossections, Attenuation Coefficients, and Energy Absorption Coefficients from 10 keV to 100 GeV', NSRDS-NBS29, 1969.

Editorial in Phys Med Biol 24(4), 685-688, 1979

Dupont handout PB2-D-7.0 5/81.

Fuji Film Handbook: Processing and Handiling of Medical X-ray Films.

Fuji Film Medical X-ray Products Technical Handbook: Control of the Photographic Properties of Medical X-Ray Films Processed in Automatic Processors.

BIBLIOGRAPHY (cont.)

Fuji Film Medical X-Ray Products Technical Handbook: The Fundamentals of Photography.

Johns,H.E., The Physics of Radiology, 2nd Ed., p. 444. Charles C Thomas publ., Springfield Ill. 1961.

Knoll,G.F., Radiation Detection and Measurement, John Wiley and Sons, Toronto, 1979.

Coulam,C.M., Erickson,J.J., Rollo,F.D., Everette,A., (Ed.s) The Physical Basis of Medical Imaging, Appleton-Century-Crofts, New York, 1981.

Curry,T.S.,III, Dowdey,J.F., Murry,R.C.,Jr., Christensen's Introduction to the Physics of Diagnostic Radiology, 3rd Ed., p. 115. Lea & Febiger publ.,Philadelphia, 1984.

Bering,P.R., Data Reduction and Error Analysis for the Physical Sciences, McGraw-Hill Book Co., Toronto, 1969.

Taylor,J.R., An Introduction to Error Analysis: The Study of Uncertainties in Physical Measurements, University Science Books, Mill Valley, California, 1982.

Evans,R.D., The Atomic Nucleus, McGraw-Hill Book Co., Toronto, 1955.

Jackson,J.D., Classical Electrodynamics, 2nd Ed, John Wiley & Sons inc., New York, 1962.

Gradshteyn,I.S., Ryzhik,I.M., Tables of Integrals, Series, and Products, Academic Press Inc., Toronto, 1980.

Whitman,R.L., Zinck,E.E., Nalepa,R.A., Chemistry Today, 2nd Ed, Prentice-Hall Canada inc., Scarborough Ont., 1982.